Measurement of the Total ^{8}B Solar Neutrino Flux at the Sudbury Neutrino Observatory

Vadim Liviu Rusu

A DISSERTATION

in

Physics and Astronomy

Presented to the Faculties of the University of Pennsylvania in Partial Fulfillment of the Requirements for the Degree of Doctor of Philosophy

2003

Eugene W. Beier

Supervisor of Dissertation

Randall D. Kamien

Graduate Group Chairperson

To Iris

Acknowledgments

Bă calule, dacă nu-ţi place la plug
ar hi trăbuit să te faci popă

Onu lu Maieraş

This thesis and the work within could not have happened without the efforts and contributions of a large number of people.

First, I want to thank Gene Beier, my thesis advisor, for guidance throughout the years and help to get to the end. His vision and understanding of the modern problems in physics made me want to carry this on and continue after. Josh Klein is the person I most closely worked with. From explaining what "Q" or "cluster" means to the right way to say "beach" he was a great teacher and a very good friend. Everything I ever done on SNO sparked from a discussion with him and everything I will ever do in physics will bear his intellectual imprint.

My fellow "first phase" grad student and friend, Mark Neubauer, was always willing to answer my naive questions, before and after he graduated, and he never said no to an MP of lager at Buzzy's or New Deck. Bill Heintzelmann was the one that helped me with my statistical quandaries and signal extraction problems. Chris Kyba and Monica Dunford, good friends and SNO-mates, were my fellow grad students during the "salt phase". They were always willing to help when I was asking for a "money plot" and made life in 2E5 and Sudbury an enjoyable experience. During the first two years, when I was struggling to understand the "paddle-cards" Richard Van de Water was the one to explain to me all the details about the electronics during long days U/G and long nights at Eddie's. I am grateful to Bill Frati who helped me with my first analysis projects. Rick Van Berg helped me a lot during the GPS boards

design and construction and I definitely owe him all I know about electronics design and testing. I also thank the post-docs at Penn: Scott Oser, for useful discussions about systematics and Neil McCauley for handling the data processing and other tedious analysis problems. Chuck Alexander and Godwin Mayers were the two persons that made the GPS boards a reality and helped me with the testing and installation. Paul Keener was always there to help me with my "queue" problems and general computational issues.

Outside Penn, I want to thank in particular to Aksel Hallin and Alan Poon for their help on the external low energy background analysis. Noel Gagnon was the person with whom I spent a lot of time U/G doing long ECALs and electronic repairs. Rich Helmer pointed out the "bifurcated analysis" to me. There are a lot of people on SNO that deserve my gratitude but whose name are not mentioned here. A big "thank you" to you all. In the non-SNO world I want to thank Cristian Staii (Varu) for being a good friend and tennis partner throughout the years.

My family back home gave me support and understanding for the 22 years in schools.

Finally, I want to thank Iris for all her patience and love during all the years in grad school. She is the one I dedicate this work to.

ABSTRACT

MEASUREMENT OF THE TOTAL ^{8}B SOLAR NEUTRINO FLUX AT THE SUDBURY NEUTRINO OBSERVATORY

Vadim L. Rusu

Eugene W. Beier

This work presents experimental measurements obtained by analyzing the first 254 live days of data from the SNO NaCl run. The electron neutrino flux was measured to be $1.66 \pm 0.10(\text{stat.})^{+0.07}_{-0.07}$ (syst.) $\times$ 106cm^{-2}s^{-1}and the non-electron neutrino flux was measured to be $3.32 \pm 0.38(\text{stat.})^{+0.26}_{-0.25}$ (syst.) $\times$ 106cm^{-2}s^{-1}. Using the above results we determined the integrated electron neutrino survival probability to be $0.33 \pm 0.04(\text{stat.})^{+0.02}_{-0.02}$ (syst.). This rejects maximum mixing in the solar neutrino sector at more than 3σ using SNO data only under the assumption that the flavor changing mechanism is due to the MSW effect in the solar interior.

The capability of the Sudbury Neutrino Observatory (SNO) to distinguish between the Charged-Current(CC) and Neutral-Current(NC) neutrino interactions made possible the first simultaneous measurements of the electron and non-electron solar neutrino flux, providing a direct test of the hypothesis that neutrinos change flavor as they propagate from the Sun to the Earth. Two tonnes of purified NaCl were added to the one kilotonne of heavy water target of SNO to enhance the neutron capture efficiency and detection of capture gamma-rays. Neutron capture on ^{35}Cl often produces multiple gamma-rays, which permits a statistical separation of neutron capture and electron events based on the event isotropy. the increased statistical separation between event categories, using the degree of event isotropy, made possible a significant improvement on the measured fluxes. Moreover, the flux analysis does not require

any assumption regarding the energy dependence of the flavor changing mechanism.

Contents

List of Figures

List of Tables

Ch. 1

Physics of Neutrinos

1.1 Introduction

Neutrinos, postulated by Pauli more than 70 years and first observed by Reines and Cowan [1] 45 years ago, are probably the least understood fundamental particles. The physics of massive neutrinos developed throughout the last 30 years of the last century and opened interesting new concepts, such as neutrino oscillations.

Using the Sun as the source of neutrinos is not a new idea. It was first attempted in the late 60's by Ray Davis in the Homestake experiment [2]. The large flux of solar neutrinos compensates for the low neutrino interaction cross-sections. The Sudbury Neutrino Observatory (SNO) experiment uses deuterium as an active target for solar neutrinos in order to measure the electron and the non-electron neutrino fluxes separately. This information can be used to probe the neutrino flavor change in a model independent way. Fundamental physics implications can be derived about the total solar neutrino flux and the mixing parameters (Δm^2 and $\tan^2\theta$).

This thesis describes the analysis of the first 254 days of data from the second phase

of the SNO experiment. We start by familiarizing the reader with the fundamental concepts of the physics of massive neutrinos and the experimental progress made so far. A detailed description of the detector follows. The next chapter provides the tools necessary for understanding the detector in terms of calibration, reconstruction and data selection. We continue with how the fundamental parameters for the analysis are measured and estimation of backgrounds. We show then how the neutrino fluxes can be determined through a maximum likelihood method. Last, the final results are extracted and conclusion are presented.

1.2 Massive neutrinos and the Standard Model of Particle Physics

I briefly describe in what follows some of the theoretical aspects related to the physics of massive neutrinos. We start by placing the neutrinos, as elementary particles, in the context of the Standard Model (SM) of elementary particle physics and show the implications related to the existence of massive neutrinos. Since the scope of this thesis is to measure a component of the neutrino flux from the Sun, we will also present some of the main ingredients of the Standard Solar Model (SSM), especially parts pertinent to the production and propagation of neutrinos through solar medium. There has been great development in neutrino physics over the past 5 years, and the field is rapidly evolving with new and interesting theoretical ideas as well as new experimental facts.

1.2.1 Symmetries and Standard Model

Symmetries have played a fundamental role in our understanding of particle physics. Starting with the Poincare group of space-time transformations to the isospin invariance group of SU(2) in nuclear physics and the flavor SU(3) symmetry group of Gell-Mann and Ne'eman ([3]) for hadron physics, our understanding of physics has always deepened with the identification of an invariance group in the system. There are two distinct kind of symmetries for physical systems: *global symmetries* where the symmetry transformation is applied to a field at all space-time points, and *local symmetries* where the symmetry transformation at different space-time points are unrelated.

Our present description of nature relies upon the concept of invariance under local symmetry transformations, or gauge invariance. The Standard Model as it was developed initially by Glashow ([4]), Weinberg ([5]) and Salam ([6]) and expanded later to include the strong interactions by Glashow, Iliopoulos and Maiani ([7]) is based upon the gauge group $SU(3)_c \times SU(2)_L \times U(1)_Y$. Since the main topic here is the neutrino, we are going to restrict ourselves to the lower group $SU(2)_L \times U(1)_Y$. This symmetry is broken down via the Higgs mechanism to an unbroken $U(1)_Q$ symmetry with the associated generator, the electric charge given by: $Q = I_{3L} + Y/2$. Here, I_{3L} is the third component of the weak isospin and Y is the hypercharge. To discuss the weak interactions of fermions one should assign quarks and leptons to the following representations of $SU(2)_L \times U(1)_Y$:

$$q_L = \begin{pmatrix} u_L \\ d_L \end{pmatrix} : (2, \frac{1}{3})$$

$$u_R : (1, \frac{4}{3})$$
$$d_R : (1, -\frac{2}{3})$$
$$\psi_L = \begin{pmatrix} \nu_{eL} \\ e_L \end{pmatrix} : (2, -1)$$
$$e_R : (1, -2)$$

where in (x, y), x defines the $SU(2)$ representation (isospin) and y the $U(1)$ representation (weak hypercharge) we are referring to. Similar assignments are repeated for all three families (flavors) of quarks and leptons with (u, d, e, ν_e) replaced by (c, s, μ, ν_μ) and (t, b, τ, ν_τ).

One thing clearly missing from this picture in order to have a complete (even merely aesthetic) symmetry between the quark sector and the lepton sector is ν_R (sometimes denoted as N_R). Although we have no experimental confirmation of ν_R's, there is no fundamental reason why one does not add this in. The ν_R is not introduced simply because we do not want neutrino masses to be present in the model. The introduction of ν_R will not change anything in the gauge sector of the theory. Using the zero charge of the neutrino one can show that an eventual ν_R, singlet under $SU(2)_L$ is also singlet under $U(1)_Y$ in a (1,0) representation of the gauge group.

In the context of the Lagrangian formalism we can write for the mass of neutrinos:

$$-L_{Dirac} = m_D(\overline{\nu_L}\nu_R + \overline{\nu_R}\nu_L) = m_D\overline{\nu}\nu \tag{1.1}$$

This is a typical Dirac mass term which connects states of right(R) and left(L)[1]

[1]The left/right combination is needed in order to obtain a singlet for the mass term in the

chiralities through a Yukawa coupling with the iso-doublet Higgs [8]. We can define the Dirac field, a four-component spinor, as a combination of left and right chiral fields using the ν_L and ν_R states and the corresponding CPT partners ($(\nu_L)^C = (\nu^C)_R$ and $(\nu_R)^C = (\nu^C)_L$). In the Dirac context, the right handed state can be viewed as a sterile, stand alone entity. However, it has exactly the same mass as ν_L, therefore, its introduction does not change the mass spectrum of the theory.

Eq. (1.1) is written for a single generation, but it could be easily updated to include all 3 neutrino generations known so far (see the Z-pole study at LEP[2]), in which case the Yukawa coupling (m_D) becomes a 3×3 matrix, allowing mixing and flavor changes between separate families as long as there are non-diagonal terms in the mass matrix, that is, the mass eigenstates are not identical to the interaction eigenstates. The Dirac mass term conserves the lepton number, as an accidental symmetry of the model. If mixing would not be present, the lepton number would be conserved for each generation, but this symmetry is explicitly broken by allowing flavor transition to a lower $L = L_e + L_\mu + L_\tau$ accidental $U(1)$ symmetry.

The Z-pole study at LEP can only account for neutrinos interacting via the electro-weak interaction. In principle, more generations are allowed (there are many models that predict more than 3 neutrino types), which increases the dimension of the Yukawa coupling matrix. The extra neutrinos are genuinely sterile, they have different masses and their introduction in the SM has more far reaching implications than the ν_R addition. As it will be discussed below, there are some hints that such particles exists and current experiments are probing this question in detail.

Lagrangian under the group transformations, particularly, $SU(2)$

[2]Colliding e^+ and e^- one can measure the total width of the Z-boson as well as the partial width of all the "visible" decay modes. Subtracting the two, one can obtain the "invisible" partial decay width of the Z-boson. The width for a single $\nu\overline{\nu}$ mode can be calculated and from this and the above measurement one can determine the $N_\nu = 2.994 \pm 0.012$

Aside from the Dirac mass term, since neutrinos are chargeless, it is possible to construct the mass singlet by using the CPT counterpart of ν_L, the right-handed field ν_R^C. This is the Majorana mass term (Eq. (1.2)), which violates the lepton number by 2 and connects a neutrino with an anti-neutrino. This leads to interesting phenomena like neutrinoless double beta decay.

$$-L_{Majorana-active} = \frac{1}{2} m_A (\overline{\nu_L} \nu_R^C + \overline{\nu_R^C} \nu_L) = \frac{1}{2} m_A \overline{\nu} \nu \tag{1.2}$$

As it can be seen, $\nu = \nu_L + \nu_R^C$, satisfies $\nu = \nu^C$, so the particle is the same as the antiparticle. This mass term needs a Higgs triplet, or some particular combination of doublets, in order to ensure the singlet nature for the mass term.

Last, following the principle that everything that is not forbidden is allowed, we can form the Dirac-Majorana mass term by also allowing terms like:

$$-L_{Majorana-sterile} = \frac{1}{2} m_S (\overline{\nu_L^C} \nu_R + \overline{\nu_R} \nu_L^C) \tag{1.3}$$

which can be generated either by a Higgs scalar or can simply be a mass term allowed by the gauge symmetries.

This gives the complete picture for 1 neutrino generation as:

$$-L_{D-M} = \begin{pmatrix} \overline{\nu_L} & \overline{\nu_L^C} \end{pmatrix} \begin{pmatrix} m_A & m_D \\ m_D & m_S \end{pmatrix} \begin{pmatrix} \nu_R^C \\ \nu_R \end{pmatrix} \tag{1.4}$$

1.2.2 The See-Saw mechanism

Eq. (1.4) leads to the so called "see-saw" mechanism, which is one of the many models invented to explain the smallness of the neutrino masses. Since there is no reason to

believe that the flavor eigenstates are identical to the propagation (mass) eigenstates we can introduce the fields:

$$n_L = \begin{pmatrix} \nu_L \\ \nu_L^C \end{pmatrix} = \begin{pmatrix} \cos\theta & \sin\theta \\ -\sin\theta & \cos\theta \end{pmatrix} \begin{pmatrix} \chi_{1L} \\ \chi_{2L} \end{pmatrix} \tag{1.5}$$

Here χ_{1L} and χ_{2L} are the left handed components of the neutrino mass eigenstates. This mixing angle is given by:

$$\tan 2\theta = \frac{2m_D}{m_S - m_A} \tag{1.6}$$

and the neutrino mass eigenvalues are:

$$m_{1,2} = \frac{m_A + m_S}{2} \pm \sqrt{\left(\frac{m_S - m_A}{2}\right)^2 + m_D^2} \tag{1.7}$$

The χ's must necessarily be Majorana neutrinos: we start with four degrees of freedom (ν_L, ν_R and their CPT conjugates) and there are two mass eigenstates, so there have to be two massive neutrino fields. Each of them corresponds to two degrees of freedom, therefore, Majorana particles.

The "See-Saw" arises naturally in this framework. Consider $m_A << m_D << m_S$. In this limit:

$$\theta \approx \frac{m_D}{m_S} << 1, \quad m_1 \simeq m_L - \frac{m_D^2}{m_R}, \quad m_2 \simeq m_R \tag{1.8}$$

It follows that we have a very light Majorana eigenstate, χ_1 (composed mostly of ν_L) and a very heavy Majorana eigenstate, χ_2 (composed mostly of ν_R), and it is χ_2 being heavy that makes χ_1 light, therefore, the see-saw. Interesting to note that with

the largest Dirac mass eigenvalue of the order of the electroweak scale, $m_D \sim 200\text{GeV}$ and $m_S \sim 10^{15}\text{GeV}$, which is close to the typical GUT scales, one would obtain the heaviest of the lightest neutrino to be $\sim (10^{-2} - 10^{-1})\text{eV}$, which is close to the right order of magnitude.

1.2.3 Neutrino oscillation

As for any fermion, the neutrino masses, if present, could be given by the Yukawa coupling to Higgs, as seen in Sec. 1.2.1, which opens the possibility that the propagation states (mass eigenstates) are not the same as the interaction eigenstates, which in turn, produces the oscillation phenomenon. By definition, the neutrino created at the interaction point, called ν_l, is a superposition of the physical states, with different masses m_α:

$$|\nu_l >= \sum_\alpha U_{l\alpha} |\nu_\alpha > \tag{1.9}$$

where U is the unitary matrix used in diagonalizing the matrix that describes the Yukawa coupling.

Considering linear wave propagation and using the relativistic approximation ($E_\alpha \approx |p| + \frac{m_\alpha^2}{2|p|}$) we can obtain the oscillation pattern as :

$$P_{\nu_l \nu_l'} = \sum_{\alpha,\beta} \left| U_{l\alpha} U_{l'\alpha}^* U_{l\beta}^* U_{l'\beta} \right| \cos\left(\frac{2\pi x}{L_{\alpha\beta}} - \phi_{ll'\alpha\beta} \right) \tag{1.10}$$

where $L_{\alpha\beta} = \frac{4\pi|p|}{m_\alpha^2 - m_\beta^2}$ and $\phi_{ll'\alpha\beta}$ is a mass independent phase factor.

The mixing matrix can be parameterized as:

$$U = \begin{pmatrix} 1 & 0 & 0 \\ 0 & c_{23} & s_{23} \\ 0 & -s_{23} & c_{23} \end{pmatrix} \times \begin{pmatrix} c_{13} & 0 & s_{13}e^{i\delta} \\ 0 & 1 & 0 \\ -s_{13}e^{-i\delta} & 0 & c_1 3 \end{pmatrix} \times \begin{pmatrix} c_{12} & s_{12} & 0 \\ -s_{12} & c_{12} & 0 \\ 0 & 0 & 1 \end{pmatrix} \tag{1.11}$$

where $s_{ij} = \sin\theta_{ij}$, θ_{ij} represents 3 mixing angles, and δ is the CP violating phase allowed [3] .

Experimental data ([9]) suggests that $|U_{13}| << 1$ which allows a simplified 2-family treatment of oscillations. In particular, for oscillations length pertinent to solar neutrinos we have:

$$P_{ee}^{3\nu} = \sin^4\theta_{13} + \cos^4\theta_{13} P_{ee}^{2\nu} \tag{1.12}$$

In the 2-generation case, the mixing matrix takes a simple form:

$$U = \begin{pmatrix} \cos\theta & \sin\theta \\ -\sin\theta & \cos\theta \end{pmatrix} \tag{1.13}$$

and the survival probability in vacuum becomes:

$$P(\nu_\alpha \to \nu_\alpha) = 1 - \sin^2 2\theta \sin^2\left(\frac{1.27\Delta m^2 L}{E}\right) \tag{1.14}$$

with $\Delta m^2 \equiv {m_2}^2 - {m_1}^2$ in eV^2, L being the source-detector distance in km, and E, the neutrino energy in GeV.

In the presence of matter the oscillation pattern can be altered due to the sup-

[3] There are actually 2 more CP violating phases arising from the relative electroweak eigenstates admixture in the Majorana fields, but they have no influence on the kinematics/oscillations

plementary charged-current interactions with electrons. This can lead to typical resonance phenomena depending upon the density profile of the material under consideration. This is the so-called MSW effect, first pointed out by Wolfenstein [10] and later applied to solar neutrino oscillations by Mikheyev and Smirnov [11]. The additional interaction leads to different forward-scattering amplitude for ν_e relative to other flavors. The net effect is an enhancement or reduction of oscillations near the resonance condition. If we consider, for instance, $\nu_e \longrightarrow \nu_\mu$ oscillations in the Sun (or the Earth), the instantaneous mixing angle in matter takes the form:

$$\sin 2\theta_m = \frac{\Delta m^2 \sin 2\theta}{\sqrt{(\Delta m^2 \cos 2\theta - A)^2 + (\Delta m^2 \sin 2\theta)^2}} \tag{1.15}$$

where $A = 2\sqrt{2}EG_F N_e$ (G_F is the Fermi constant and N_e is the electron number density in the medium). Eq. (1.15) shows an enhancement (reduction) of the mixing angle in matter for $\theta < \frac{\pi}{4}$ ($\theta > \frac{\pi}{4}$). Thus, matter effects allow us to determine whether the largest component of ν_e is lighter (or heavier) than the largest component of ν_μ. If ($\Delta m^2 \cos 2\theta = A$ (the resonance condition), the mixing angle becomes maximal. As the neutrino propagates through matter the mixing angle changes according to changes in the matter density.

The transition probability for a neutrino propagating through matter can be approximated as ([12]):

$$P(\nu_e \longrightarrow \nu_\mu) \simeq \frac{1}{2} - \frac{1}{2} \cos 2\theta_i \cos 2\theta_f (1 - 2\mathcal{P}) \tag{1.16}$$

where θ_i is the mixing angle at the production point, θ_f is the mixing angle at the detection point and $\mathcal{P}$ is a measure of adiabaticity in the neutrino propagation through

Source	L (m)	E(MeV)	$\bar{m}(\mathrm{ev}^2)$
Reactor	10^2	1	10^{-2}
Meson factory	10^2	10	10^{-1}
Accelerators	10^3	10^3	1
Atmosphere	10^7	10^4	10^{-3}
Solar core	10^{11}	1	10^{-11}

Table 1.1: Possible neutrino experiments and their typical sensitivity range

matter[4].

An interesting limit arises from (Eq. (1.16)) as we consider the maximum mixing. In this case, the vacuum mixing angle is $\theta_0 = \pi/4$. Usually, we will consider $\theta_f = \theta_0$, so the transition (survival) probability becomes equal to 0.5 according to (Eq. (1.16)).

The sensitivity of a certain experiment to an oscillation hypothesis (mass squared difference and mixing angle) depends on $\bar{m} = \frac{E}{L}$. If this quantity is much bigger than $|m_\alpha^2 - m_\beta^2|$ any oscillation effect would be hard to observe and if it is much lower, than the oscillation pattern would need more space to develop. Table 1.2.3 shows the expected sensitivities for the most common sources of neutrinos and the related neutrino experiments. The solar neutrino experiments, are sensitive to wide range of mass scales ($\Delta m^2 \sim 10^{-4} - 10^{-10}\mathrm{eV}^2$).

As a last comment it should be noted that the addition of masses for neutrinos in the SM is not the only way to obtain flavor transformation. Other exotic models, like equivalence principle violation or neutrino magnetic moment[5], could be a potential candidate and are explored in the literature [12].

[4]In the adiabatic approximation, the matter density varies slowly

[5]Assuming that the magnetic field is large enough

1.2.4 Final remarks

Although the addition of neutrino masses does not constitute a fundamental problem for the Standard Model of particle interactions, there are lots of question marks to be raised: why the masses are so small ($m_{\nu_e} < 1$eV while m_e=551keV), what are the terms in the coupling matrix (and similarly, does the electron neutrino couple mostly to the light state – normal hierarchy, or the heavy state – inverted hierarchy), are there any other neutrinos besides the three known (and what are their interactions), is there any CP violating phase to be sought within the Yukawa coupling matrix (for two generations there is no CP violating phase, since any complex phase can be re-absorbed in the field definitions, but for three generations one phase remains), are there any CPT violation processes to be explored in the neutrino sector?

Our current understanding on neutrino physics is rather limited. As the situation stands now, neutrinos might offer interesting hints for physics beyond the Standard Model (the "see-saw" model, for instance, predicts the existence of large mass scale particles). The measurement of CP violation is also crucial, for the same reasons for which it is currently done in the quark sector, to help understand the matter-antimatter asymmetry in the Universe. Any deviation from unitarity is a clear indication of physics beyond the Standard Model. From an experimental standpoint, although the cross-sections are small, the cleanliness of such a measurement with leptons is very appealing.

1.3 The Sun, the Standard Solar Model and Neutrinos

Neutrinos, at the present level of understanding, interact only through weak interaction. Because of that, the interaction rates are extremely small, and in order to perform a neutrino experiment, one needs a very large flux of incoming neutrinos and as large a target as possible. As mentioned in Sec. 1.2.3, one of the many sources of neutrinos is the Sun, which produces exclusively *electron neutrinos*. The ^{8}B flux, to which SNO is sensitive, due to its high energy threshold, has been calculated to be $\sim 5 \times 10^6 \mathrm{cm}^{-2}\mathrm{s}^{-1}$ [13] at the surface of the Earth. This immense flux of neutrinos is a by-product of the thermonuclear reactions which power the Sun and occur deep inside the solar core. The overall reaction $4p + 2e^- \longrightarrow {}^4\mathrm{He} + 2\nu_e + 26.7\mathrm{MeV}$ goes through several steps as shown in Fig. 1.1. Most of the energy released ($\sim 97\%$) is taken by the photons which travel to the surface of the Sun and gets emitted as light. The rest of the energy goes as kinetic energy to neutrinos and heavy nuclei.

Each reaction presented in Fig. 1.1 is determined by nuclear physics without any reference to a particular solar model. The total number of neutrinos, the normalization, comes out of detailed simulations of the solar physics.

The neutrino fluxes as predicted by the Bahcall-Pinsonneault-Basu (BP2000) standard solar model [13] are shown in Fig. 1.2. Another prediction of the solar model is the density profile of the Sun which allows the calculation of the resonance parameters for the MSW effect as described in Sec. 1.2.3.

Understanding solar physics in detail might look at a first glance to be quite a daunting task. There are, however, a certain number of parameters such as, as mass, radius, surface composition and photon luminosity which are well known and

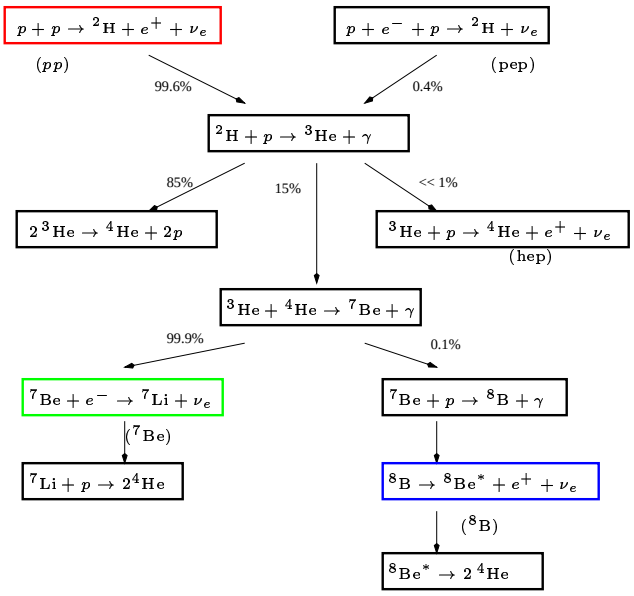

Fig. 1.1: Nuclear reactions involved in the *pp* chain. From [14].

can be calculated based upon models which rely on hydrostatic equilibrium, isotopic abundance and other assumptions specific to a star on the main sequence . A complete presentation of the stellar evolution and solar measurement together with neutrino flux calculations is given in [14]. The great success of the Standard Solar Model has proved to be the agreement with the helioseismological data on the observed surface vibration modes (better than 0.1%). This gives a lot of confidence in the neutrino flux as predicted by SSM.

1.3.1 The Solar Neutrino Problem (SNP)

More than 30 years ago, in the Homestake experiment, Ray Davis ([2]) and collaborators made the first attempt to measure the flux of neutrinos coming from the Sun, using the interaction of neutrinos with ^{37}Cl above an energy threshold of 0.8 MeV. The result was unexpected; it showed a deficit of solar neutrinos relative to the Stan-

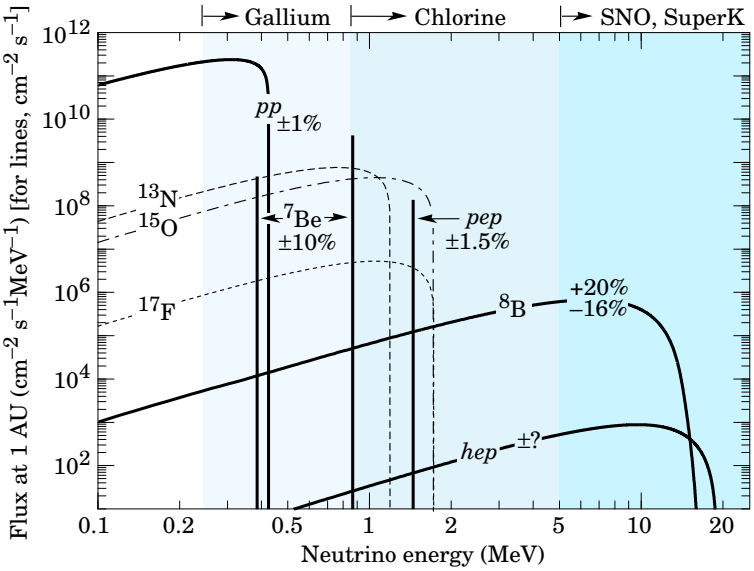

Fig. 1.2: BP2000 SSM neutrino energy spectra from [15]. Also shown (top of figure) are the energy thresholds for the various types of solar neutrino experiments.

dard Solar Model prediction. A completely different experiment based on a different method (Kamiokande II and later SuperKamiokande) found similar deficits proving that the observations were correct. This deficit in the solar neutrino flux was also observed later through another experiment (GALLEX) using the interaction of neutrinos with ^{71}Ga. This time, the low energy threshold (0.233 MeV), improved the sensitivity to the *pp* reaction which represents by far the largest contribution to the solar neutrino flux as seen in Fig. 1.1. The constraint on the *pp* flux by the observed solar luminosity made it even harder to believe that the neutrino deficit was due to a failure to model appropriately the neutrino production in the Sun in the standard solar theory. Different results, for different experiments and energy sensitivity range are shown in Fig. 1.3.

This discrepancy came to be known as the Solar Neutrino Problem (SNP). B.

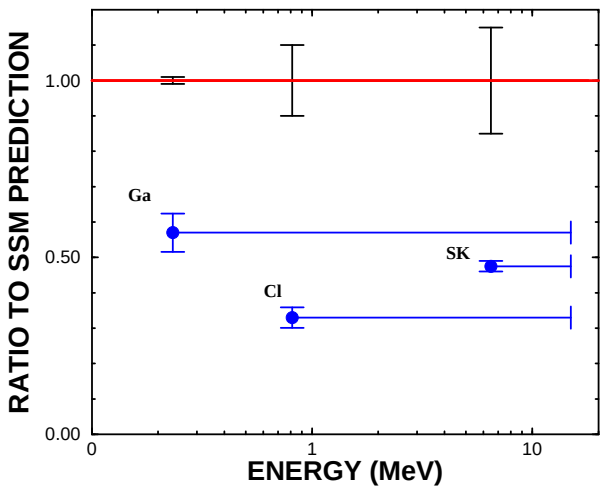

Fig. 1.3: The Solar Neutrino Problem, as reflected by the most constraining solar neutrino measurements before SNO. The uncertainties for the SSM predictions for each experiment are also shown

Pontecorvo was the first one to postulate that neutrinos have mass. Following the model of the $K_0 - \bar{K}_0$ meson system, he suggested the neutrino oscillations mechanism. Later, L. Wolfenstein expended the formalism to incorporate the effect of matter on the oscillation pattern. Mikeyev and Smirnov applied this new formalism to the solar core and developed a whole theory for the propagation of solar neutrinos from the production point, in the core of the sun, to the Earth. One point should be stressed here, this was the first indication of flavor mixing in the lepton sector, which was already a known phenomenon in the quark sector.

There were at least two other possible, though perhaps not as appealing explanations. One is the possibility that the SSM is incorrect. The SSM proved to be a great success for a lot of other predictions. More than that, the hypothesis used in the model are mostly related to nuclear physics and not so much to solar properties.

A second option in solving this dilemma is the possibility that one or more experiments is wrong. In comparison between Cl vs Ga, the systematics involved are quite different. Also, the advent of Water Cerenkov detectors, rendered the result almost impossible to be explained as a common, unknown, instrument related problem. Not only are the measuring techniques very different but also, the energy thresholds and the sensitivity range are specific to each experiment. Fig. 1.2 shows the neutrino energy spectra for each solar reaction and the range to which each experiment is sensitive.

1.3.2 The SNO approach

The Sudbury Neutrino Observatory (SNO) is a water Cherenkov detector, but unlike its predecessors, it can distinguish, on a statistical basis, electron neutrinos from the other two types.[6] This novel capability was made possible by using heavy water (D_2O) as the active target [16]. There are three interactions a neutrino can undergo when traversing the D_2O medium:

Elastic scattering (ES)

This is the process though which a neutrino scatters off an atomic electron in either the D_2O or the H_2O region[7]

$$\nu_{e,(\mu,\tau)} + e^- \rightarrow \nu_{e,(\mu,\tau)} + e^-$$

The relativistic scattered electrons may have an energy above the Cherenkov threshold and produce Cherenkov photons that then get imaged by photo-multiplier tubes. The

[6] The previous water Cherenkov experiments, like Kamiokande and Super-Kamiokande, were sensitive to all flavors, but the dominant contribution came from the electron flavor ($\sim \frac{5}{6}$) and had no capability to distinguish between flavors

[7] Ch. 2 gives more details about the structure and functionality of the SNO detector

Cherenkov radiation is produced in a cone with the angular opening of $\cos\theta = \frac{1}{\beta n}$, where β is the particle velocity relative to the speed of light and n is the refractive index of the medium. For water, $n = 1.33$ and the angle turns out to be $\sim 42°$. Under ideal condition, the signature of an ES event will be the image which is the intersection of a perfect cone on a sphere. Multiple Coulomb scattering makes the image less than perfect, but in principle, the ES events will have a certain degree of anisotropy. This is the reaction for which the previous water Cherenkov experiments were sensitive. Its major characteristic is the angular distribution of the scattered electrons which is strongly forward-peaked in the direction of the incident neutrino. This is important for separating the events, but also for establishing the Sun as the source of neutrinos seen in SNO.

Charged current (CC)

The first way in which a neutrino can break up the deuteron is via the CC interaction:

$$\nu_e + d \rightarrow p + p + e^-$$

The detection is similar to the ES detection, with the relativistic electron producing Cherenkov radiation in a forward cone. Also, there is a slight anti-correlation between the electron direction and the initial neutrino direction $(1 - 0.340\cos\theta)$. Most important, the electron energy follows the incident neutrino energy more closely than the electrons for the ES reaction , offering the possibility of accurately measuring the spectrum of the incoming neutrinos. The threshold for this reaction is 1.44 MeV.

Neutral current (NC)

The last, but certainly the most important process in SNO is the disintegration of a deuteron via a neutral current reaction.

$$\nu_x + d \rightarrow n + p + \nu_x$$

This interaction is equally sensitive to all active neutrino flavors, which gives SNO the capability to normalize the CC (or ES) flux measurement. The interaction threshold is 2.2 MeV and results in a free neutron which thermalizes and is then captured on a nucleus. During the D_2O phase the neutron captures on a deuteron, producing one γ-ray which Compton scatters. The Compton electron then generates Cherenkov light. In general, the γ may Compton scatter multiple times and there may be more than one recoil electron above the Cherenkov threshold. The net effect of multiple Compton scatters will be a slight increase in the isotropy of the event.

By adding a Cl salt, to the D_2O multiple γ's are produced by neutron capture on ^{35}Cl. The Cherenkov light from NC events in salt will have a characteristic high degree of isotropy. This helps reduce the statistical covariance between electron and neutron events. Also, the visible Cherenkov energy of the NC events is increased and the neutron capture cross-section is higher, which allows a larger collection of neutrons for a more precise measurement of the NC flux .

1.4 The current status of neutrino flavor change in the solar neutrino mass regime

In the last few years we have accumulated an immense[8] amount of information about flavor changing processes in the solar neutrino mass regime. In addition to previous experiments[9], the SNO D_2O measurement, which included a total neutral-current flux and therefore a proper normalization, offered clear evidence for neutrino flavor change. This section briefly describes the results from the two.

1.4.1 SNO D_2O measurement

In August 2001 SNO collaboration published the first measurements of the CC and ES interaction rates from the pure D_2O phase [17]. Above a relatively high threshold of $T_{eff} > 6.75$ MeV kinetic electron energy, the measured ^8B flux assuming the standard spectrum shape was determined to be:

$$\begin{aligned} \phi^{CC}_{SNO}(\nu_e) &= 1.75 \pm 0.07\ (\text{stat.})^{+0.12}_{-0.11}\ (\text{sys.}) \pm 0.05\ (\text{theor.}) \times 10^6\ \text{cm}^{-2}\text{s}^{-1} \\ \phi^{ES}_{SNO}(\nu_x) &= 2.39 \pm 0.34(\text{stat.})^{+0.16}_{-0.14}\ (\text{sys.}) \times 10^6\ \text{cm}^{-2}\text{s}^{-1} \end{aligned}$$

The CC flux was from SNO then compared to the more precise ES flux reported by the SuperKamiokande collaboration [18]:

$$\phi^{ES}_{SK}(\nu_x) = 2.32 \pm 0.03\ (\text{stat.})^{+0.08}_{-0.07}\ (\text{sys.}) \times 10^6\ \text{cm}^{-2}\text{s}^{-1}.$$

[8] Relatively speaking, since the neutrinos are probably the least known particles in the Standard Model

[9] Both radio-chemical and water Cherenkov detectors in the pre-SNO era provided numerous indications of flavor change, but the lack of a proper normalization in the flux measurement precluded a definitive result

The difference of $0.57 \pm 0.17 \times 10^6$ cm^{-2}s^{-1},was interpreted as evidence of an active non-ν_e component in the solar flux at 3.3σ confidence level.

The reason for applying a 6.75 MeV energy threshold was two-fold. First, at the time it was felt that the level of backgrounds was not completely understood in the low energy regime and second, to limit the presence of neutrons in the signal region, so that a clear extraction of the number of CC events could be made.

Over the next year (2001-2002), a lot of progress was made in understanding the low energy backgrounds and the neutron response, so that in July 2002, SNO published a second article [19] that offered direct evidence for neutrino flavor transformation at 5.3σ. This was done by measuring the total active neutrino flux through the neutral current interaction. At a lower threshold (5 MeV electron kinetic energy),

$$\begin{aligned}
\phi_{\rm SNO}^{\rm CC}(\nu_e) &= 1.76^{+0.06}_{-0.05}({\rm stat.})^{+0.09}_{-0.09}\ ({\rm syst.}) \times 10^6\ {\rm cm}^{-2}{\rm s}^{-1} \\
\phi_{\rm SNO}^{\rm ES}(\nu_x) &= 2.39^{+0.24}_{-0.23}({\rm stat.})^{+0.12}_{-0.12}\ ({\rm syst.}) \times 10^6\ {\rm cm}^{-2}{\rm s}^{-1} \\
\phi_{\rm SNO}^{\rm NC}(\nu_x) &= 5.09^{+0.44}_{-0.43}({\rm stat.})^{+0.46}_{-0.43}\ ({\rm syst.}) \times 10^6\ {\rm cm}^{-2}{\rm s}^{-1}
\end{aligned}$$

which can be converted into electron and non-electron neutrino fluxes by a simple change in variables (Ch. 6) to obtain the flux of electron and non-electron active neutrinos:

$$\begin{aligned}
\phi_e &= 1.76^{+0.05}_{-0.05}({\rm stat.})^{+0.09}_{-0.09}\ ({\rm syst.}) \times 10^6\ {\rm cm}^{-2}{\rm s}^{-1} \\
\phi_{\mu\tau} &= 3.41^{+0.45}_{-0.45}({\rm stat.})^{+0.48}_{-0.45}\ ({\rm syst.}) \times 10^6\ {\rm cm}^{-2}{\rm s}^{-1}
\end{aligned}$$

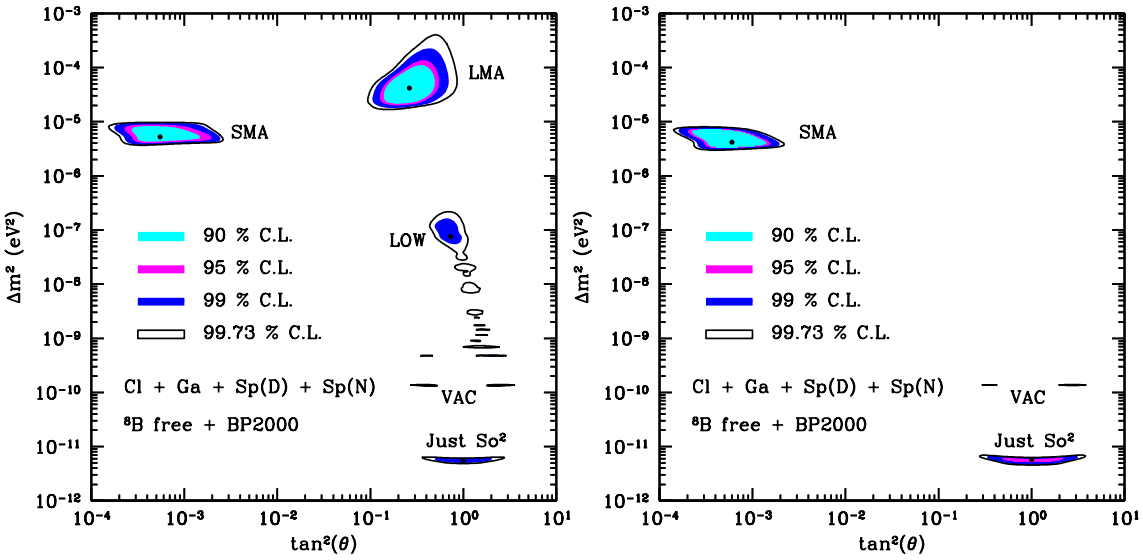

Fig. 1.4: Allowed regions in the Δm^2-$\tan^2\theta$ plane at various confidence levels for oscillation to (left) active (ν_μ , ν_τ) and (right) sterile neutrinos in the pre-SNO era. From [20].

The Bahcall-Pinnsoneault-Basu (BP2000) Solar Model [13] predicts a total flux of $\phi_{SSM} = 5.05^{+1.01}_{-0.81} \times 10^6$ cm^{-2} sec^{-1} in agreement with the SNO measurement.

The results had a large impact on the understanding of neutrino flavor physics. The allowed regions of MSW parameters (Δm^2 and $\tan^2\theta$) from a global fit to all neutrino experiments before SNO are shown in Fig. 1.4. Substantially different classes of solutions were allowed with relatively similar probability.

After SNO published the neutral current result together with the separate day and night energy spectra [21], the picture changed to what is shown in Fig. 1.5. Most of the previous regions were excluded and the only solution left at 95%CL was the so-called "Large Mixing Angle" (LMA). The best fit value for δm^2 was 5×10^{-5}eV^2 and $\tan^2\theta = 0.34$. The oscillations to *only* sterile states were completely excluded. Admixtures of active-sterile neutrinos in the solar sector still remain as a viable solution.

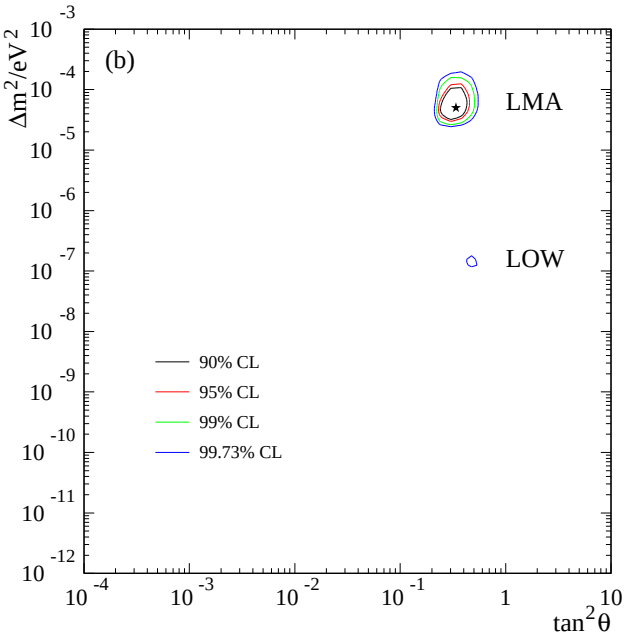

Fig. 1.5: Allowed regions in the Δm^2-$\tan^2\theta$ plane at various confidence levels for oscillation to (left) active (ν_μ , ν_τ) and (right) sterile neutrinos after SNO. From [21]

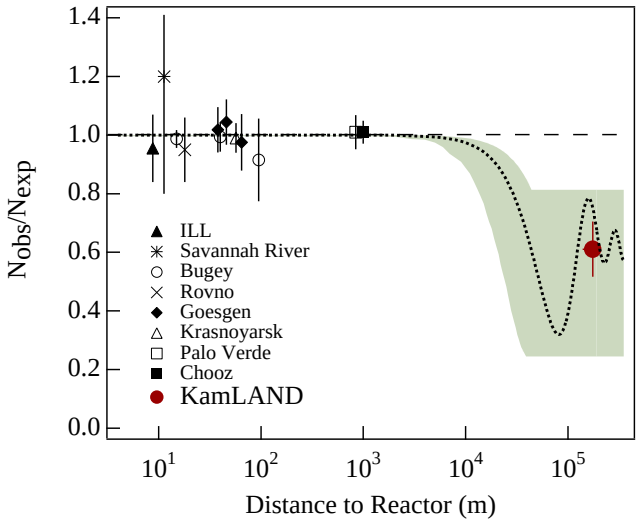

Fig. 1.6: Flux reduction result measured by different experiments at different energies and base-lines. The superimposed line is the survival probability for the best fit to the solar neutrino data. Taken from [22]

1.4.2 A new generation of reactor experiments: KamLAND

Before the SNO data established LMA to be the strongly favored solution for the massive solar neutrino oscillations, a number of experiments (Palo-Verde, CHOOZ, Goesgen, etc.) attempted a measurement of the oscillations parameters using reactor anti-neutrinos[10] . The combination of energy and reactor-detector distance was not appropriate for the actual value of Δm^2 and $\tan^2\theta$ that those experiments tried to determined (see Fig. 1.6). KamLAND [22] was the first reactor neutrino experiment with the right energy-baseline combination that was able to measure a signal in the anti-neutrino flux suppression from reactors.

Located in Japan, KamLAND measures the anti-neutrino flux from multiple nuclear power plants, at an average distance of $\sim$ 180km. The detection mechanism is

[10]Assuming CPT invariance the expected flux suppression for anti-neutrinos should be the same as for neutrinos, so the parameter realm that an anti-neutrino experiment is sensitive to, should be the same as a neutrino experiment

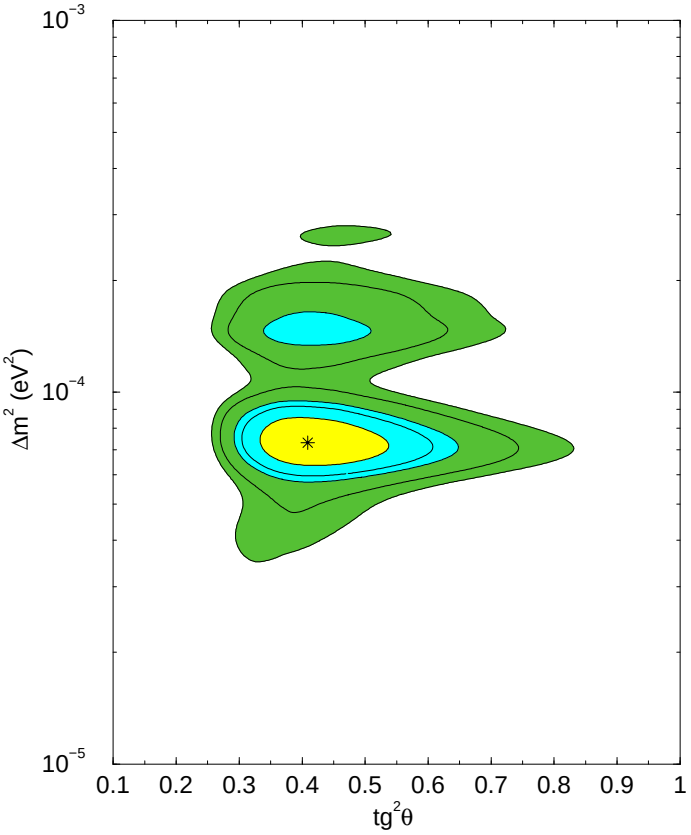

Fig. 1.7: Allowed regions from a combined analysis of the solar neutrino data and the KamLAND spectrum at 1σ, 90%, 95%, 99% and 3σ C.L. The best fit point is marked by a star. Taken from [23]

the inverse β-decay reaction, $\overline{\nu_e} + p \longrightarrow e^+ + n$ in liquid scintillator. For 162 ton·yr of reactor data KamLAND measures a suppression of $0.611 \pm 0.085(\text{stat}) \pm 0.041(\text{syst})$ above an energy of 2.6MeV for the prompt events (e^+). Performing a global analysis that includes both the solar data and the KamLAND rates and spectrum, one can drastically limit the allowed regions for the oscillation parameters[11] (Fig. 1.7). The best fit point turned out to be ([23]) $\Delta m^2 = 7.3 \times 10^{-5}$ eV^2 and $\tan^2\theta = 0.41$[12].

[11] One can also include the effects due to 3 generations, by assuming a non-zero value of U_{e3}. This results in shifting the allowed regions to larger Δm^2 and smaller $\tan^2\theta$.

[12] The χ^2 minimization was performed with a free ^{8}B flux.

Ch. 2

The SNO Detector

This chapter provides an introduction to the site, functionality and operations of the Sudbury Neutrino Observatory (SNO) detector. We describe here as exhaustively as possible the crucial sub-systems with emphasis on the design and building of the GPS interface, which is the major contribution of the author to SNO electronics.

2.1 Sudbury, Neutrinos and Life Underground

SNO [24] is located near Sudbury, Ontario, near the #9 Shaft of INCO Ltd. Creighton mine. Creighton is one of the most productive nickel mines currently in operation. At a depth of 6800 feet (2039 m) the norite rock provides a shielding equivalent to ~6000 m of water, reducing the cosmic muon flux to 3 muons an hour on an effective area of $\sim 200\,\mathrm{m}^2$.

The transport of the materials used in the constructions as well as daily access to the lab is provided by an elevator car (called the "cage") which runs periodically between the surface and all the mine levels. From the cage shaft to the SNO laboratory

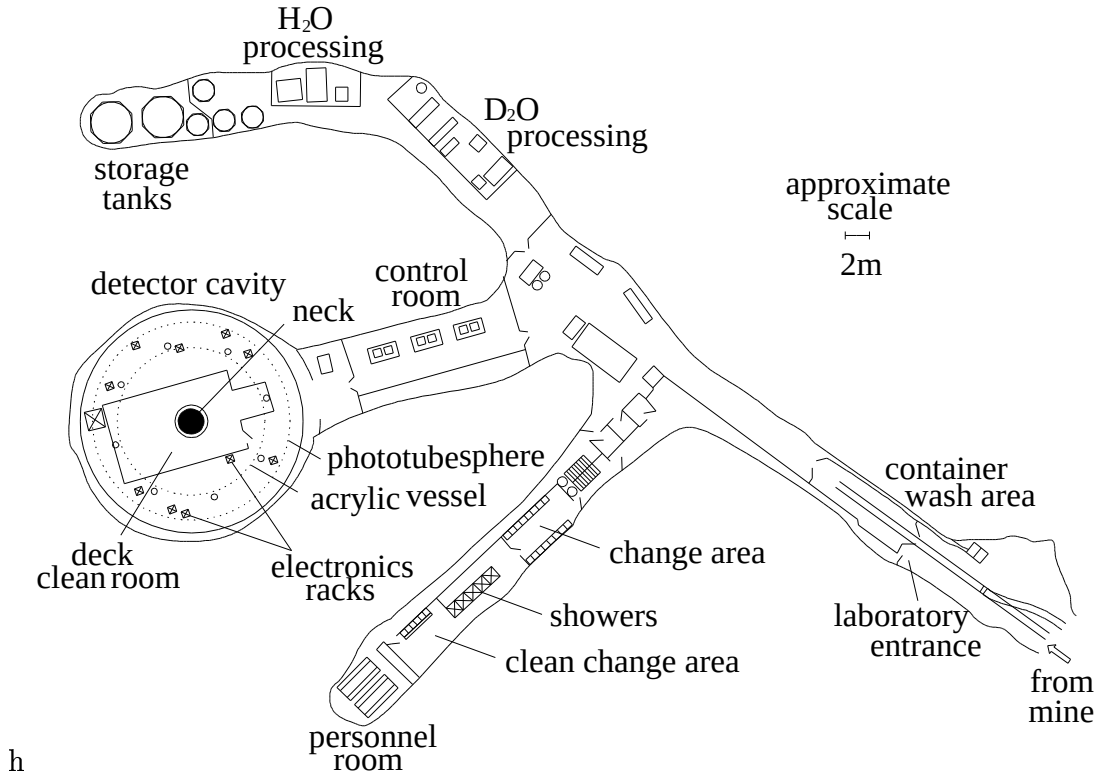

Fig. 2.1: Layout of the SNO site. The detector itself is sealed under the deck in 22×30 m cavity. The only access, for calibrations, is allowed through the neck (shown in the figure and the guide tubes (tubular structure that run vertically through the detector). Taken from [25]

one has to walk approximately 2 km to gain entrance to the lab (Fig. 2.1) itself and must observe the clean room procedures needed to keep the radioactivity levels in SNO as low as possible.

The detector sits in a 22 m diameter, 30 m high barrel shaped cavity, filled with pure water for shielding. A spherical structure made of steel, 18 m in diameter (**P**hotomultiplier **SUP**port Structure-"PSUP") holds the photo-multiplier tubes. Inside the PSUP, there is a spherical acrylic vessel containing 1000 tones of purified heavy water (D_2O). The readout and control electronics are located on a deck at the top of the cavity. Access to the water inside the detector is performed from a

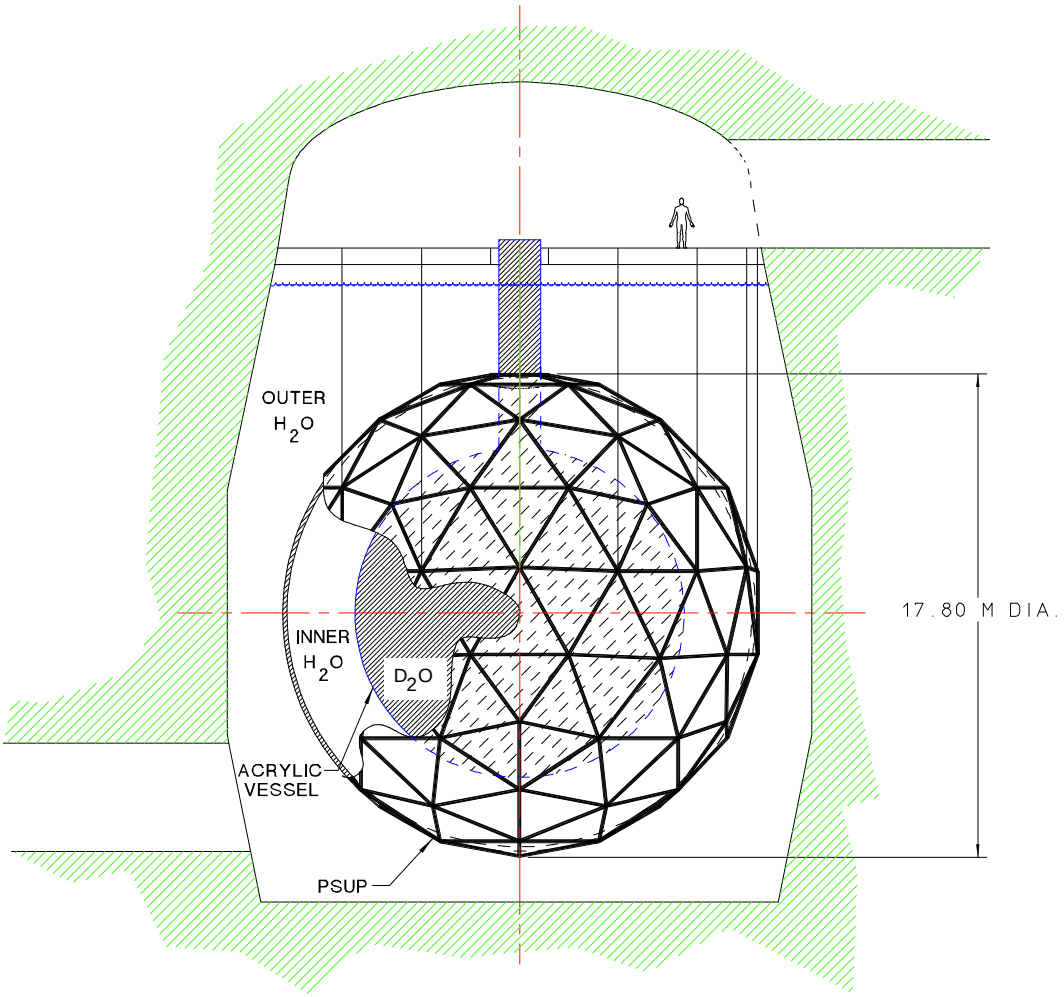

Fig. 2.2: Schematic view of the SNO detector. Taken from [25]

dark room on the deck (Deck Clean Room, DCR). Strict procedures for cleanliness are enforced everywhere in the lab, especially in the DCR. A schematic view of the detector is shown in 2.2.

2.2 The Water System

The constant challenge for the water system is maintaining the low level of radioactivity required to perform the SNO measurements while continuously circulating and keeping the water at a nominal temperature of 10°C.

The radioactive backgrounds can mimic the neutrino signal (described in 1.3.2) in two ways. First, a γ ray from certain nuclei can disintegrate a deuteron and produce a neutron. Since the thermalization process loses all the energy and direction information of the initial neutron, no cut can be devised to reduce the neutron background through off-line analysis. The only way to perform the measurement is to precisely determine how many neutrons come from photo-disintegration and keep them at a very low level. The second cause for a false signal can be a low energy radioactivity event shifted to the signal region by the finite energy resolution of the detector and the properties of the off-line reconstruction. For example, a low energy γ (or $\beta - \gamma$) could appear to have an energy above the analysis threshold and reconstruct inside the fiducial volume. In the Uranium and Thorium chain, two decays are the most dangerous: ^{208}Tl (2.615 MeV γ) and ^{214}Bi (2.445 MeV γ). The target level for the amount of U and Th present in the detector has been set so that the background would not exceed 5% of the SSM expectations for the signal [24]. To meet this requirement SNO has to achieve levels which are smaller than 4.5 x 10^{-14} g/g ^{222}Rn, 3.7 $\times 10^{-15}$ g/g ^{224}Ra, and 4.5 $\times 10^{-14}$ g/g ^{226}Ra in the D_2O and 4.5 $\times 10^{-13}$ g/g ^{222}Rn, 3.7 $\times 10^{-14}$ g/g ^{224}Ra, and 4.5 x 10^{-13} g/g ^{226}Ra in the H_2O .

The way in which SNO reaches these levels is described in the next sections and the measurement techniques employed will be detailed in Sec. 5.2.1.

2.2.1 The Heavy Water

The key to the SNO experiment is the heavy water which constitutes the active target used for distinguishing between the two fundamental reactions in SNO (CC and NC, 1.3.2). The 1 kt of heavy water was obtained as a loan from Atomic Energy of Canada (AECL). The heavy water system is responsible for maintaining the required level of radioactivity at low levels while maintaining the high isotopic purity ($> 99.9\%$) of the D_2O. The removal of the impurities is done by circulating the water (max. rate of $\sim$150 l/min) through ultra-filtration membranes and a reverse osmosis system (RO). The D_2O is de-gassed before going into the detector to decrease radon and oxygen levels. During the second phase of the experiment, purified NaCl was added to the heavy water. The total amount of salt added was $\sim$2 tones, corresponding to a concentration by weight of 0.196%.

2.2.2 The Light Water

The main purpose of the light water is to provide shielding against external radioactivity, mainly coming from the surrounding rock and the PSUP. To attain the desired levels of radioactivity, the water is highly purified through continuous circulation. Before entering the detector, the water is de-gassed, passed through a series of membranes, and through an RO unit. In order eliminate biological contamination, the water is irradiated with UVs from mercury lamps and then cooled to 10°C.

2.3 The Acrylic Vessel (AV)

The 1 kt of heavy water is contained in a spherical structure made from 122 UVT (UV transmitting) 5.6 cm thick acrylic panels. The material used in construction of the AV also had to have low levels of radioactivity ($< 10^{-13}$ g/g U/Th) and be transparent to Cherenkov light. The AV extends in the upper hemisphere with a neck which allow access for the D_2O circulation and for the calibration sources to be deployed inside the heavy water. The neck is made from acrylic less transparent to UV in order to reduce the detection of light produced in that upper region of the detector[1]. The AV is suspended from the deck with 10 Vectran fiber ropes.

2.4 The Photo-multiplier Tubes (PMT)

The active region of the detector is 4π steradians relative to the center of the AV (except for the neck opening) viewed by 9438 inward-facing Hammamatsu R1408 photo-multiplier tubes which are fixed to a 18 m diameter stainless steel structure (PSUP). The diameter of a PMT is 20 cm and the surface glass is special low radioactivity (Schott 8426) made by Schott Glaswerke. The photo-cathode coverage is 31% which is increased to 59% by 27 cm in diameter light concentrating reflectors which surround the PMT surface glass. The vertical component of the geomagnetic field is canceled with 14 horizontal field compensation coils embedded in the cavity walls to increase the photo-cathode efficiency.

Under normal operation the HV on typical PMTs is set to ~ 2 kV which provides a gain of 10^7 and a dark rate of ~ 500 Hz. The transit time through a typical PMT

[1]The static discharge in the neck turned out to be an important source of instrumental backgrounds as it will be describe below in text

is $\sim$ 30 ns while the spread in the transit times is less than 1.5 ns. In addition to the 9438 inward-looking PMTs there are also 91 outward looking PMTs which detect cosmic muons as well as instrumental sources of light.

During the first months of commissioning massive high voltage breakdowns were observed. The reason was that O-ring seals in the high voltage connectors were assembled at atmospheric pressure. When immersed in de-gassed water, the gas diffused out of the connectors and that caused low pressure inside the connector. The flawed connector design permitted electrons to initiate avalanche discharges at low pressure. To make the connectors function properly, the water is re-gassed with N_2 so the detector could be run at the nominal HV.

2.5 Front end electronics, trigger and Data Acquisition System

The electronics for SNO generates the trigger and records PMT information [25], [26]. Designed to record data continuously from 9728 channels with less than 10 ns trigger dead-time, the system has performed extremely stably throughout the data taking.

Although the design and commissioning phase took place before 2000, the author has taken on active role in maintaining all parts of the system, and also upgrading and building new components. This section will describe in detail the front end electronics and the trigger system together with the data acquisition (DAQ). At the end of this chapter, I give a detailed description of the GPS communication system used in SNO. A graphical description of all systems related to the event readout and control is shown in Fig. 2.3.

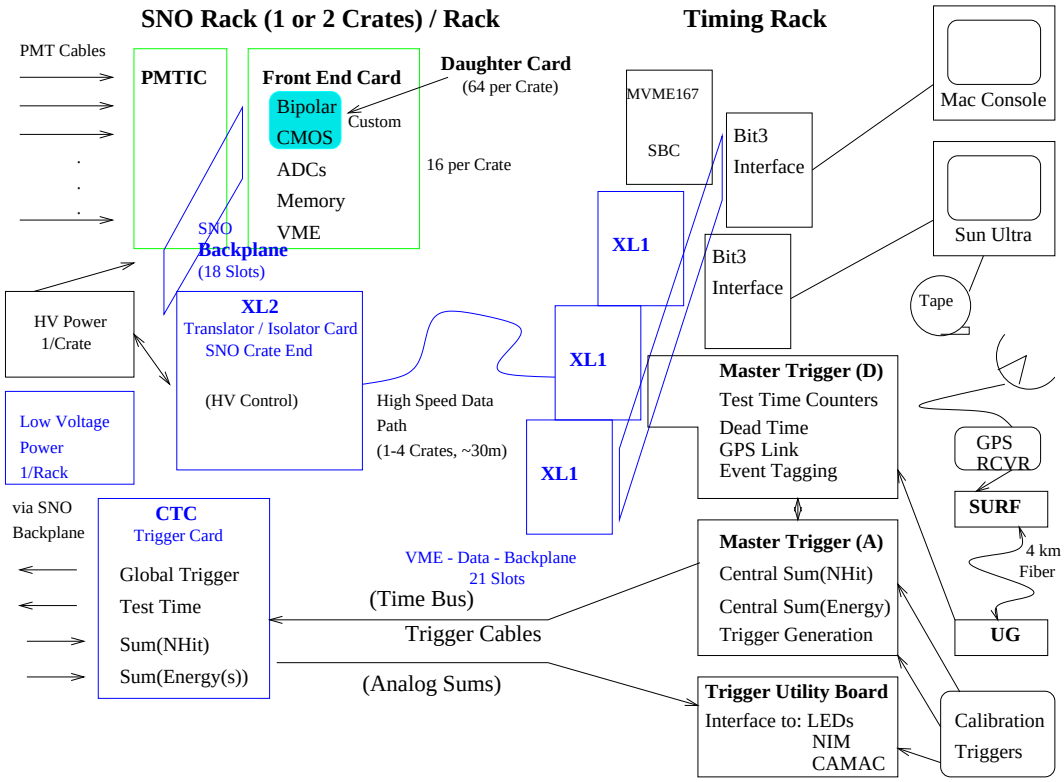

Fig. 2.3: The general overview on the SNO electronics and Data Acquisition System. The different parts of the readout chain are: the front end, the bus communications and translations, the triggers system, the main DAQ computers and the surface-underground communications for GPS. Taken from [25]

2.5.1 Front end electronics

Although the signal rate (solar neutrinos) is very small, the electronics chain is required to handle large rates ($\sim$ 1 kHz) due to backgrounds and possible supernovae events, without significant dead-time. This is implemented through 3 custom ASICs (Application Specific Integrated Circuits) and 16 custom designed electronic boards. The ASIC chip set consists of a wide-dynamic-range integrator, a fast and sensitive discriminator/gating circuit, and an analog/digital pipelined memory with a timing circuit.

The front-end of the SNO electronics sits in 19 crates, each processing signals from up to 512 PMTs. The signal cycle begins with a photon generating an analog pulse from a PMT. The analog pulse travels through $\sim$ 32 m of 75Ω RG59-like waterproof coaxial cable to the PMT interface card (PMTIC). There are 16 PMTICs in a crate, and each PMTIC serves 32 PMTs. The cables are grouped in 4 bundles of 8 cables on a paddle card. The PMTIC also provides HV to the PMT as well as disconnects for individual cables, HV blocking capacitors for the PMT signal, over-voltage and breakdown protection for the integrated circuits, limited read-back of the PMT current, and a programmable calibration pulse source for each channel. The PMTIC connects directly to its companion Front End Card (FEC32). The FEC32 is responsible for processing, digitization and storing of the 32 signals coming from the PMTIC.

The main part of the processing is done by the ASICs. They reside on four daughter-boards (DBs), each DB handling 8 channels. There are two discriminator chips (SNOD) on each DB. SNOD is a fast discriminator which observes any leading edge of the pulse and splits it in two branches (approximately in the ratio 1:16) and feeds it into two separate channels, one low-gain and one high-gain, of a four channel charge integrator (SNOINT). Each channel of the SNOD chip has independent discriminator and gate generators to provide the timing functions necessary for the SNOINT chip. The SNOINT and SNOD chip outputs [27] are then delivered to the CMOS ASIC (QUSN7) analog memory. The QUSN7 chip [28] stores the integrated signals, provides a time-to-amplitude conversion (TAC) and issues the trigger logic for the SNO detector. The 16-deep analog memory samples the low- and high-gain channels of the SNOINT at early and late times for a total of four possible charge

samples for each memory cell[2].

The TAC and the timing sequence are initiated on the leading edge of SNOD signal. The TAC starts whenever a given PMT fires and is stopped on the arrival of a centrally generated Global Trigger (GT) or resets itself if no trigger has been generated. If the trigger has been generated, the four analog voltages corresponding to three charges and one time measurement are stored in one of the 16 analog memory banks (cells) for later digitization and an associated digital memory records the GT number (GTID), and any associated condition flag. When a QUSN7 has data, it asserts a "Data Available" flag which initiates the on-board readout cycle. The readout is controlled by a clocked, synchronous state machine (the "sequencer"), implemented in a standard field-programmable gate array (FPGA). On the assertion of the data-available flag, the sequencer will present the four voltages stored in the analog memory of the QUSN7 chip to the inputs of four commercial MAX120 12-bit 2-μs ADCs. The digitized information is then read by the sequencer and written to the 4MB SIMM DRAM on-board memory. The information from a complete digitization process is contained in a 3-word, 12-byte, fixed format data structure. The 3 words contain the four digitized voltages (charges+time), a 16-bit GT sequence number (GTID), four bits of cell address and four flag bits. This is a complete description of a PMT hit in the sense that the time, charge, GTID and the geographical location are fully specified and can be used by down-stream analysis. Even if the memory is loaded out of temporal sequence, the hit descriptors can be properly sorted out by the DAQ event builder based on their unique GTID.

All communications (data, address, control) between different parts of the system

[2]At any time we can set the system to acquire 3 types of charge measurements. A long integration and a short integration version of the high gain and one low gain charge which can have either (but not both) short or long integration times

are done through a custom backplane that implements the "SNOBus" protocol. A relatively high-speed (>8MB/s) RS485 link between the SNOBus crate and the central DAQ VME crate is implemented through a pair of translator cards (XL1, XL2). The translator card located on the SNOBus (XL2) crate performs TTL-GTL conversion. All data and addresses on the SNOBus are transmitted as GTL logic (0.8 V swing) in order to reduce pickup with the highly sensitive PMT signals.

2.5.2 The Trigger system

The SNO trigger system provides the decision level necessary for saving the events which resemble a typical neutrino events. The idea behind the trigger logic is simple. The event is considered "interesting" if a preset number of PMTs fire in coincidence [29]. There are several variants of this logic which SNO uses, but the main physics analysis hardware trigger is set at a threshold of 16 PMT firing within a 100 ns window.

Besides the decision logic, the trigger system also provides several system wide functions: calibration of the electronics (pedestals and slopes) through a controllable source of pulses (see Sec. 3.1.1) , synchronization and time stamps of the events, FEC's local counter tests through individual pulsing and GPS synchronization for absolute timing measurements.

A pictorial description of the trigger system in shown in Fig. 2.4. The front end of the trigger cycle is completely analog. This choice was made for reasons of speed. The time between N tubes firing and the return of the corresponding global trigger system is around 240 ns, mostly dominated by cables between the central trigger station and the individual crates. Each time a PMT pulse crosses the SNOD threshold, the

channel's QUSN7 chip will produce a small current pulse with uniform height for each channel and a width of 100 ns.[3] The choice of this particular time was made in order to accommodate the Cherenkov light reflections off the PSUP ($\sim$ 80 ns) within a trigger window. A hierarchical sum is performed at a crate level. Eight channels are summed on the DB, then the signals from each pair of DBs are summed on the MB and then driven through the SNOBus backplane. The two top DBs summed signals are routed far away from the bottom DBs summed signal to reduce the pickup on the trigger lines. All 512 channels in a crate are then summed on a Crate Trigger Card (CTC) and then the signal is passed to the MTC/A (the analog summing system wide trigger card) where all the 19 crates are summed together.

Although the 100 ns pulse (NHIT100) is the main physics analysis hardware trigger, there are other ways of triggering the detector. Similar to NHIT100 there is a 20 ns pulse (NHIT20), which could be very useful for an in-time coincidence from different locations in the detector. There is also analog summing of copies of the PMT pulses themselves. This triggers (e.g. ESUMHI) turned out to be an extremely useful tool for studying instrumentation generated backgrounds because of their characteristic pulse shape. The veto tubes (**O**ut**w**ard **L**ooking-OWLs) can essentially create separate triggers from normal tubes. OWLN is an OWL version of the NHIT100 signal and OWLEHI is the OWL version of ESUMHI signal. Each of those pulses is summed independently of others and each goes to its own MTC/A.

An MTC/A can provide up to three separate trigger thresholds simultaneously. Once a signal has crossed a threshold on the MTC/A, the comparator fires a 20 ns logical trigger pulse which is sent to the digital part of the trigger system (MTC/D). A DAQ programmable bit mask on the MTC/D enables any particular selection of

[3] This width is programmable over a narrow range whose maximum is 100 ns.

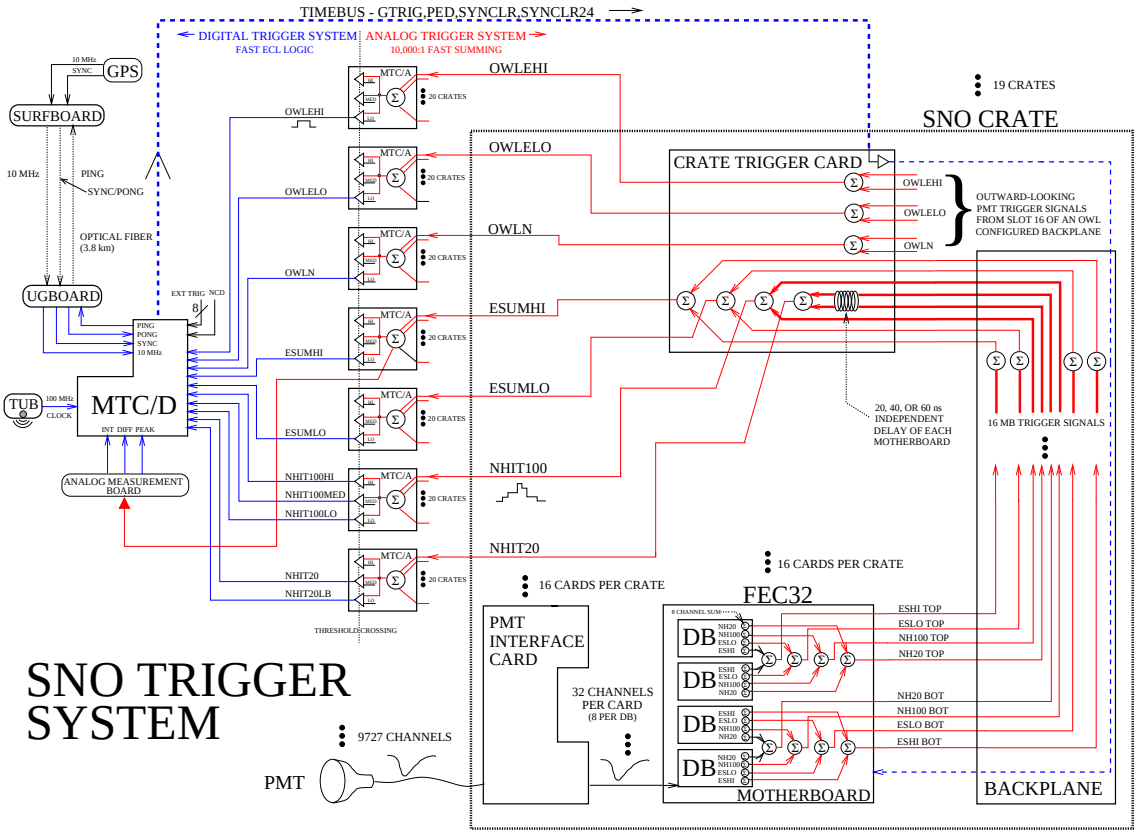

Fig. 2.4: Generation, summing and decision stages of the SNO trigger system. Figure courtesy of M. Neubauer

trigger combination. If a trigger signal whose mask bit is enabled fires, a 20 ns long "raw trigger" is created which then waits at a latch for the next tick of an on-board 50 MHz clock. The raw trigger is then latched and a global trigger is created, driven back to the CTCs and through the backplane to the QUSN7 chip, which upon receiving it, saves any information it might have in the analog storage array. The global trigger (GT) will have an unique ID within a given run based on a 24 bit counter on the MTC/D. Since the lower 16 bits are separate from the upper 8 bits on the FEC, they have to be loaded and cleared independently. Under normal running a SYNCLR (which clears the lower 16 bit counter on the QUSN7 chip) and a SYNCLR24 (which

clears the upper 8 bits) are sent out when the lower 16 or the upper 8 bits of the GT counter on the MTC/D roll over.

When the global trigger is created on the MTC/D, an additional signal called LOCKOUT prevents any other signal from creating a global trigger while the current trigger cycle is active. LOCKOUT is set to 420 ns, during which time the MTC/D latches all of its trigger related information and writes it to its on-board memory. In addition to the trigger word selected, the MTC/D will also store the 50 MHz count to be used as a precise inter-event timing, a 10 MHz count for absolute time (GPS), the current count in the GT counter for subsequent building of the events by DAQ, and several errors and status flags. The MTC/D can store up to 1 million events on its on-board memory and is capable of handling burst rates in excess of 2 MHz. Under normal running the trigger rate is $\sim$ 20 Hz.

As mentioned above, the inter-event time is kept by the 50 MHz counter. The length of this counter is 43 bits, which means it will roll over once every 2 days. The uncertainty in event-by-event times is roughly equal to the rms jitter in the edges of the 50 MHz clock, that is less than a ns or so. The absolute time for an event is provided by the Global Positioning Satellite (GPS) system. The GPS receiver and the communication with the MTC/D are described in more detail in Sec. 2.5.4. A 10 MHz clock is sent down the optical fiber from the surface which increments a 53 bit counter. This will provide absolute time measurements for 28 years without rolling over (the t_0 is defined as Jan 1, 1996).

Trigger types in SNO

Besides physics triggers the MTC/D can generate a variety of other trigger types, used, for example, in calibration and monitoring. The total of 26 candidate trigger

types are described below [29]:

- The *NHIT100* trigger. As described above, this is the simple 100 ns coincidence trigger. For different levels, is set to trigger when a specified number of PMTs fire in coincidence window.
  - *NHIT_100_LO*: Low threshold 100 ns trigger, currently set to 11.
  - *NHIT_100_MED*: Medium threshold 100 ns trigger. Currently set at 16, this is the main physics trigger used in analysis.
  - *NHIT_100_HI*: High threshold 100 ns trigger, currently set at 21.
- The *NHIT20* trigger is the short window variant of the *NHIT100*. Channel by channel delays allows tuning this trigger to fire on specific parts of the detector.
  - *NHIT_20*: Normal 20 ns trigger.
  - *NHIT_20_LB*: Look-back 20 ns trigger
- The energy sum triggers (*ESUM*).
  - *ESUM_LO*: Low-gain energy sum trigger
  - *ESUM_HI*: High-gain energy sum trigger
- The OWL triggers are simply the one FEC version of the NHIT and ESUM triggers. They come from three FEC slots (3/15, 13/15 and 18/15) dedicated to the Outward-looking Tubes. Those types of triggers are mostly used for identifying muons from cosmic rays and act like veto trigger.
  - *OWLN*: Outward looking tube 100 ns trigger

  - *OWLE_LO*: Outward looking tube low-gain energy sum trigger
  - *OWLE_HI*: Outward looking tube high-gain energy sum trigger

- *PULSE_GT*: Pulser generated calibration trigger mostly used for calibrations of the electronics. It also acts as an unbiased detector trigger.

- *PRESCALE*: Prescaled trigger. Although it is mainly used for NHIT_100_LO prescaling with the intention of studying the low energy backgrounds in a region where the rates would be too high for normal triggering, in actuality it could use any signal plugged into the NHIT_100_LO input.

- *PEDESTAL*: The pedestal calibration trigger will generate pulsed triggers at a programmable frequency anywhere under 100MHz. It is mainly used for electronics calibrations, but it has also proven to be an invaluable tool in understanding the pathological behaviors of the electronics (TSLH, see [30]).

- The GPS triggers. They will be described in more detail in Sec. 2.5.4
  - *PONG*: GPS round-trip delay trigger (see Sec. 2.5.4)
  - *SYNC*: GPS synchronization trigger (see Sec. 2.5.4)

- *EXT_ASYNC* is the only asynchronous trigger channel in which the global trigger generated from an external input is not synchronized to the 50 MHz clock. This is usually used for laser calibrations where the 20 ns raw trigger jitter associated with the synchronization is undesirable.

- *EXT8/PULSE_ASYNC*: External trigger/Asynchronous calibration trigger mask

- *EXT6* The MISSCLK trigger is used as a tag in order to identify events where the 10 MHz clock from surface has been lost and the UG clock is being used (more details in Sec. 2.5.4).

- *EXT2, 3, 4, 5, 7*: External triggers mostly used as tags/triggers for different calibration sources.

- *SPECIAL_RAW*: Logical combination of nine pre-selected triggers

- *NCD*: Neutron Counter Detector trigger to be used in the future NCD phase of SNO.

- *SOFT_GT*: Software initiated trigger

- *MISS_TRIG*[4]: Flag denoting that a masked-in trigger arrived after the global trigger word had been latched.

2.5.3 Data acquisition software system (DAQ)

The DAQ system is mainly responsible for readout and control. It also performs the event building, runs low and high level monitoring software and provides the interface for the electronics calibrations.

The main hardware part of the DAQ system is a Motorola 68040 single-board computer without an operating system (the embedded CPU, or eCPU). The eCPU access to the VME is provided by a PCIbus-VME interface (the Macintosh Dual-Port Memory, MDPM) and an SBus-VME interface (the Sun Dual-Port Memory, SDPM) each with 8 MB of memory. The FEC data is read out passively by the eCPU which

[4]The name is somehow misleading since the trigger signal is not actually missed

also has access to the MTC/D data. Once all the hardware is read out, the eCPU transfers the data to the SDPM which is simultaneously and asynchronously read by a Sun Ultra-1 workstation (snopenn01) which runs a program to sort the FEC and MTC/D data and builds the events (Builder). The Builder output stream is written locally to a DLT tape, transferred to surface and then written to a backup tape, and broadcast (Dispatcher) to authorized clients for near-line monitoring.

The control and monitoring of the electronics and some environmental properties, is done via a user interface, SHaRC (SNO Hardware Acquisition and Readout Control) which runs on a G4 Macintosh PPC. SHaRC also maintains a database with the current hardware status (number of channels online, MB and DB status, etc.) which is generates, for each run, a DQXX bank that contains a detector snapshot of the hardware situation for subsequent Monte Carlo simulations.

On rare occasions, the PMT bundle is associated to the wrong event either through a corrupted GTID in a PMT bundle (hardware orphans) or through inefficiencies of the readout/building software (software orphans). These pathological events are saved into an "orphanage" and they are later removed through off-line analysis cuts.

2.5.4 The Global Positioning Satellite (GPS) interface

It is important that SNO can keep track of absolute, universal time. In particular, in the case of a supernova event, there has to be a precise stamp for synchronization with other experiments. This is achieved by using a commercial DATUM, GPS time and code frequency generator, which drives a 10MHz sine wave signal whose frequency is continuously modulated to remain in synchronization with clocks on-board the GPS satellites. The 10MHz signal from the GPS unit is sent to a custom designed

printed circuit board (SURFBOARD) located in the surface SNO building. The SURFBOARD converts the analog signal to optical signal and then transmits it through $\sim$ 5 km of optical fiber to the underground receiver board (UGBOARD). The UGBOARD converts the signal back to ECL (Emitter Coupled Logic) and drives it as single ended ECL to the MTC/D.

A schematic view of the GPS system is shown in Fig. 2.5. The basic idea behind the GPS interface was outlined in [31]. Mark Neubauer, a former graduate student at Penn designed the first version of it. The design was upgraded and a new version was built by the author. The old system was decommissioned and replaced by the new one in Oct. 2002.

The GPS synchronization

The GPS system also allows the synchronization of the detector to the absolute time [32], [31] . A preset time is loaded into the shift register of the MTC/D and into the GPS commercial unit by the DAQ main computer. A TTL pulse (SYNC) is driven by the GPS unit whenever this preset time is reached.

There are three operations the MTC/D does upon the SYNC's arrival. It loads the 10MHz counter with the preset time, generates a SYNC trigger and a drives a PING signal (ECL) back to the UGBOARD. The PING signal is converted to optical signal by the UGBOARD and sent to surface. The PING arrival at the SURFBOARD triggers the PONG pulse which is driven through the same path as SYNC all the way to the MTC/D where it generates a PONG trigger. The round trip synchronization delay is simply the time difference between SYNC and PONG triggers which can be calibrated out in the off-line analysis. In the current setting the DAQ instructs the GPS unit to send SYNC pulses once per hour and then checks for the SYNC/PONG

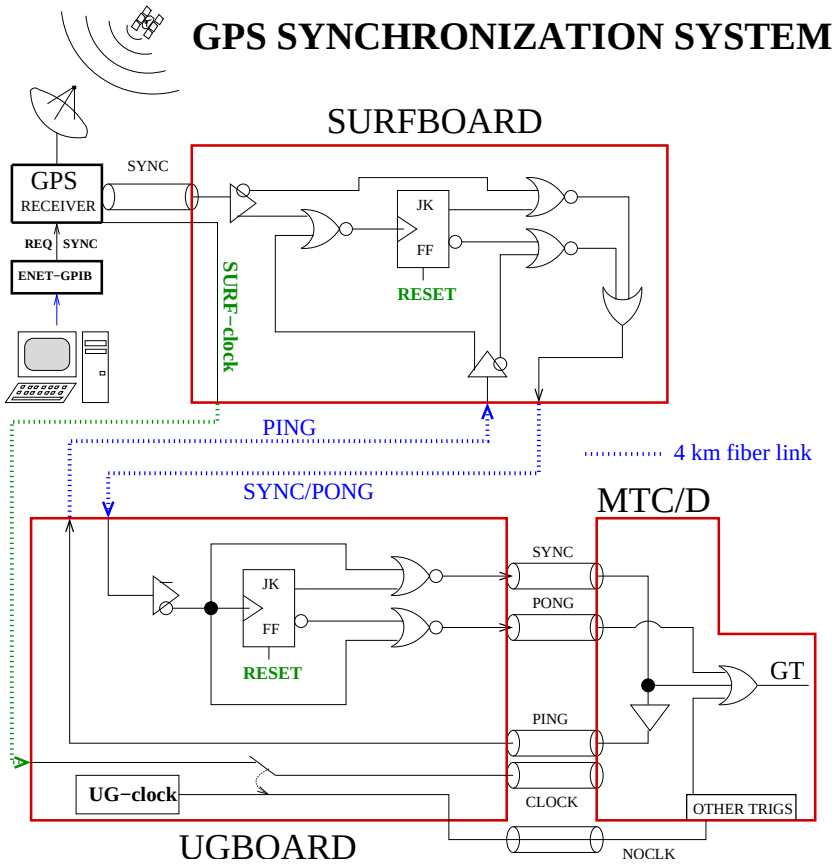

Fig. 2.5: GPS synchronization and monitoring.

triggers in the data stream.

The absolute time is kept this way to within 100 ns (i.e. one 10 MHz tick) although the relative time of the event can be determined more precisely through the 50 MHz clock.

SURFBOARD and UGBOARD

Besides the synchronization process, the two GPS boards have an important role in monitoring and controlling the 10 MHz clock relayed from the GPS unit to the MTC/D. The SNO detector is in an active mining environment, which can be some-

times disruptive to the continuous communications between surface and underground.

The 10 MHz clock, SYNC and PONG relay is implemented through commercial point-to-point optical ports made by Agilent Tech. The infrared ($\lambda \sim 1300\,\mathrm{nm}$) LED transmitter (HFBR-1312T) sends the optical signal via a 62.5/125 micron graded index multi-mode fiber to its pair PIN diode receiver (HFBR-2316T). The optical signal is converted to analog and driven through a comparator where an on-board potentiometer allows threshold fine tuning.

In case of a transmission failure (due either to the GPS unit or something else related to the fiber connection, for example) an LED indicates a failure mode on both SURFBOARD and UGBOARD. A 24 bit counter on the UGBOARD records the missing clock edges and when a preset number of counts is reached the UGBOARD raises the UGCLK status flag which is sent to the MTC/D. The maximum number of counts allowed can be set by proper setting of a jumper field on the board. On the assertion of the UGCLK, the UGBOARD automatically switches to an on-board 10MHz clock. This clock will be continuously relayed to the MTC/D until the next SYNC pulse is generated. When the SYNC comes, a decision is made. If the surface clock is back online then UGBOARD switches back to the normal 10MHz clock and de-asserts the UGCLK flag. Otherwise, it assumes that the surface clock is still unreliable and continues to use the on-board one. This "AND" clause ensures the proper synchronization and gives confidence in the stability of the surface clock for the off-line analysis.

There are multiple levels of monitoring on the SURF-UG combination. They proved to be useful tools in continuously keeping track of potential problems on the communication fibers. Since the commissioning (Oct 2002) of the new GPS system have been no failures.

2.6 SNOMAN: SNO Monte Carlo and ANalysis

The software package used for detector simulation and data analysis is a set of FORTRAN routines and uses CERN's ZEBRA memory management bank structure [33]. SNOMAN is used in conjunction with the SNODB (SNO DataBase) [34] which contains all the constants obtained from calibrations or physical calculations. SNODB is based on the CERNLIB HEPDB software package [35] and is updated periodically to incorporate new constants.

The main part of SNOMAN is the Monte Carlo simulation code, which is a mixture of elementary interaction and propagation of particles and detector simulation. The package can simulate a large range of processes, from neutrino interactions to radioactive background production and detection. A major part in SNO simulation is the propagation of electrons and neutrons and the Cherenkov light production and detection. As for any Cherenkov detector, a lot of work has been invested in understanding the electrons, γ and photon transport through the active materials of the detector. SNOMAN does this by internally accessing EGS4 (Electron Gamma Shower code) [36] with an appropriate set of parameters while neutron transport is modeled based on the MCNP code(**M**onte **C**arlo **N-P**article Transport Code System, [37]).

The events, are written to tape by the DAQ in a ZEBRA format, called ZDAB. The usual analysis process take the ZDAB banks as the input and unpacks the information contained there. Every event is subsequently calibrated using the SNODB constants, reconstructed and stacked in either PAW ntuple format [38] or ROOT tree format [39]. The detector configuration, including the important electronics effects and all the sources used for calibration are simulated in great detail within SNOMAN.

Ch. 3

Understanding the Data - Calibration, Data Selection and Reconstruction

After the tape writing process, the data is nothing more than a large collection of numbers for each PMT hit recorded in every event. The next stage is to pass it through the off-line processing to go from PMT time, location and charge information to event characteristics. In this stage, we estimate the position of the event (vertex), its direction and its effective energy. There is also the entire process of calibrating the detector in order to understand the fundamental physical responses. In the end, one has to devise tools that will reject almost all backgrounds for a clean selection of the neutrino candidates. In what follows, we will show how all these tasks are accomplished in SNO.

3.1 Tools to understand the detector

Aside from the calibration of the electronics, most of SNO's calibration is performed using source units deployed in small containers inside the detector. The access to the H_2O region is provided by the guide tubes and access to the D_2O is through the neck of the acrylic vessel. Since there are a relatively large number of detector components that can undergo changes in time, and given the SNO's desire for precision, there is a continuous need for monitoring and calibration of the detector.

3.1.1 Electronics and PMT calibration

SNO performs periodic calibrations of the electronics (ECA) and the PMTs (PCA). The ECA is done by selectively firing channels in order to determine the "pedestals" for the three charge (QHS, QHL, QLX) and one time (TAC) measurements. The hardware required for this calibration was described in Sec. 2.5.2 and Sec. 2.5.3. Using the trigger system we can simply instruct the DAQ to send programmed pulses (PEDESTAL) to fire each channel and then collect the data on another forced trigger pulse (GT). In addition to "pedestals", there is also a need to calibrate the time slopes by continuously varying the delay between the PEDESTAL and GT signals.

The usual ECA is done on a bi-weekly basis or after any major maintenance work performed on the detector components. Special analysis algorithms were designed to extract the proper calibration constants from the ECA data. Also, in order to ensure quality control the collaboration has developed algorithms to validate these constants [30]. The ECA data is flagged when, for example, the width of the determined pedestal distribution is too wide for a given channel or the constants changed significantly from a previous run. An ECA expert then decides based on this validation information

whether or not the derived constants should be stored in the database to be used in downstream analyses. The author took active role in the implementation of some algorithms used in the validation process and in the integration of the ECA validation in the overall analysis package (SNOMAN).

During the D_2O phase, it was discovered that the measured TAC value for a channel depended on the rate at which that channel was taking data (**T**ime **S**ince **L**ast **H**it, TSLH). The net effect of this behavior was to worsen the reconstruction for data taken at lower rates. During the D_2O phase a correction was developed and applied. In August 2000 a remedy was installed (fans to cool down the electronics racks) and since then, this effect has been almost non-existent and the correction has become obsolete.

The second basic calibration is the PMT calibration (PCA) which is done roughly on a monthly basis, unless otherwise required. Using a laser system (the "laserball") one can infer the PMT time and charge response to Cherenkov-like light. The "laserball" consists of a nitrogen laser, using dye cells to provide monochromatic light with seven wavelengths between 337 nm and 620 nm and a diffuser ball. The system can deliver pulses with widths <1 ns at a repetition rate of up to 40 Hz.

There are three main effects that one can study and devise corrections for based on the PCA data. First, the "walk", is due to the fact that the channel discriminator is designed to fire on the leading edge of the PMT pulse. For different pulses, this firing can occur sooner or later, depending on the pulse height. One can eliminate this through a study of correlations between the charge and the time measurements. The second correction derived from the PCA is the time offsets between PMTs. This occurs because of cable lengths, PMT transit times and differences in the length of the electronic traces and electronic components delays. Finally, although not playing

an important role in the solar neutrino analysis, due to low occupancies specifics for the energies involved, one can also design a correction for the multi-photoelectron effect. The number of photoelectrons that were detected can be determined from the charge measured by the PMT. A detailed description of the PCA and how all the necesarry corrections are applied is presented in [40].

The fundamental optical parameters like attenuation or scattering lengths, angular response of the PMTs, and of the reflectors, are deduced using a global fit to laserball data. This is done by scanning the D_2O region at different wavelengths between 337 nm and 620 nm. The fitted values for optical parameters are then used in MC to predict the detector response to various inputs.

3.1.2 Physics calibrations

In order to determine the detector response to γ 's, electrons and neutrons, the SNO collaboration has devised and deployed a large number of calibration sources with different energies and particles involved. The goals of these deployments were to understand the energy response of the detector, the reconstruction performance, neutron capture efficiency or creating models for understanding the backgrounds in the regions where the MC is difficult to calibrate directly.

The list, together with a short description of the calibration sources used in this thesis is shown below:

- ^{16}N - A triggered source that produces γ's with the largest contribution from the 6.13 MeV de-excitation of the ^{16}O resulting from the β decay of ^{16}N.
- ^{8}Li - Triggered source of β with an endpoint of 14 MeV from the β decay of ^{8}Li.

- ^{252}Cf - An untriggered source of neutrons from the fission of ^{252}Cf.

- **pT** - A linear accelerator in miniature which collides protons on a target of ^{3}H to produce ^{4}He which subsequently produces a 19.8 MeV γ through de-excitation. This source is not triggered.

- **Acrylic Encapsulated Sources** - Mostly used for background studies and low energy detector response, these sources are basically small amounts of radioactive materials (^{238}U or ^{232}Th) that are lowered into the detector in small capsules made from acrylic. Since the natural radioactivity in the detector is kept at very low levels, the amount of data obtained with these sources (although untriggered) completely overwhelms the normal baseline of radioactivity.

3.2 Off-line processing of the data

3.2.1 The reconstruction algorithm

In order to determine the relevant quantities for analysis one has to fit the PMT data for each event for time, position and direction. The reconstruction method used in this thesis has been described in [41] and is currently used for the SNO analysis in the salt phase[1].

We can define the time residual of a PMT as:

$$T_{res} = T_{PMT} - T_{ev} - \frac{|\overline{x}_{ev} - \overline{x}_{PMT}|}{c_{gr}} \tag{3.1}$$

[1]There are multiple reconstruction algorithms that SNO developed throughout the years, the one used here has been chosen for reasons of speed (CPU time)

and a likelihood function for having the event occurring at the position $\overline{x}_{ev}$ and at time T_{ev} as:

$$\mathcal{L} = \prod_{i=0}^{N_{hits}} P(T^i_{res}) \tag{3.2}$$

where T_{PMT} and $\overline{x}_{PMT}$ are the time and position of the i'th PMT of the N_{hits} PMTs that fired in the current event. The $P(T^i_{res})$ represents the probability density of having a T^i_{res} residual hit time for the i'th PMT. This distribution is taken from Monte Carlo simulation and laserball data (see 3.1) and consists of a main peak centered at zero with a σ of 1.5 ns (the typical transit time spread through the PMTs) and on each side, two smaller peaks due to pre-pulsing and after-pulsing of the PMTs. For hits later than 15 ns the time residual distribution is approximated with a constant. This is not necesarrily correct since there are non-flat structures in the real distribution associated with reflections and scattering. Nevertheless, since the amount of late light (scattered at large angles and reflected) accounts for $\sim 12\%$ of the total light the approximation holds relatively well throughout the spatial and energetic regime we are interested in.

The determination of direction is done as a second stage of the reconstruction process. To avoid late light complications, only hits within ± 10 ns window around the prompt peak are used. The likelihood function to be minimized uses the fact that electrons will generate a Cherenkov cone with an opening angle of 42°. The probability density function in $\cos(\theta)$ (the transverse angle around the reconstructed direction) is derived from Monte Carlo studies and has a sharp peak at 0.74 which gets smeared by electron Coulomb scattering. The azimuthal angle around the reconstructed direction is assumed to be flat.

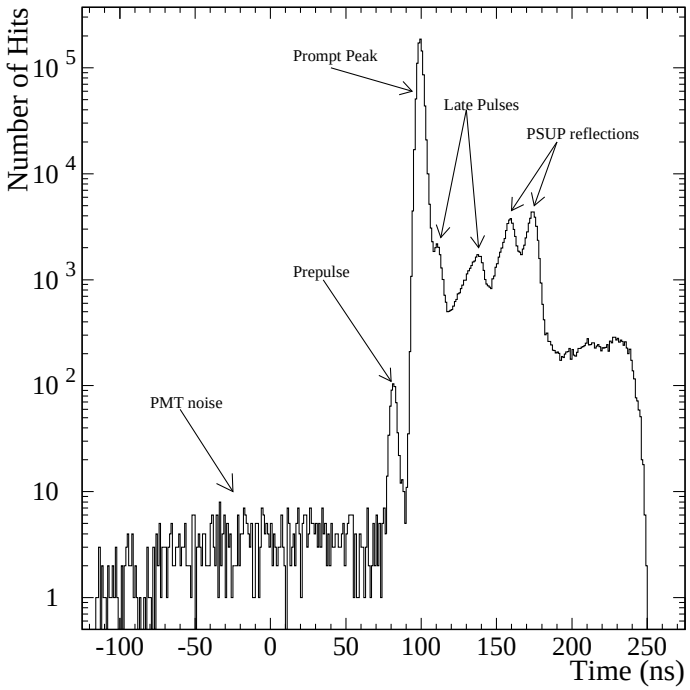

Fig. 3.1: The PMT times as measured with the laserball at the center of the detector. Figure courtesy of C. Kyba

3.2.2 The energy estimation algorithm

The way SNO estimates the effective kinetic energy of an event has been developed in [41] and we are only going to outline the algorithm here. The first step is to define the effective number of PMT hits as

$$N_{eff} = N_{in-time} - N_{noise} \tag{3.3}$$

where $N_{in-time}$ is the number of hits within a ± 10 ns window around the prompt time of the event. The latter is defined as the time it would take a photon to travel from the production point to the PMT in a straight line. N_{noise} is the number of noise hits in the same time window[2].

N_{eff} is corrected then to a N_{eff} at the center of the detector, by taking into account the attenuations of the photons in the different media and the PMT optical response. An additional correction is applied to keep track of the number of tubes online at that given time. Finally, the mapping of the corrected N_{eff} to energy is done through a MC simulation of electrons at the center of the detector.

3.3 Data reduction

As described in Sec. 2.5.3, the data collected is written to tape in a specific format (Sec. 2.6). A dedicated CPU farm processes the data using a suite of PERL modules and the main analysis package (SNOMAN). The desired electronics and PMT calibration constants are applied and the data is then reconstructed. For each run

[2]The number of noise hits in the trigger window is measured continuously using the *PULSE_GT* trigger (see Sec. 2.5.2). We can then extrapolate this number into the ± 10 ns interval assuming that the noise hits are flat throughout the trigger window

there is a subsequent MC simulation which is generated under the same conditions and with large statistics.

This section will describe how the events are selected from the data and the cuts we use for the selection. In order to reduce the sensitivity of the final result to biases, the analysis is done "blindly". This means that the final result will be completed on a "blind" data-set and only after all the tools are in place and methods for background measurement developed we will remove the blindness criteria and obtain the final result. There are multiple levels of blindness we use in this thesis:

- "Wilkerson-Elliott" scheme - An unknown fraction of events between 10 and 30% is removed from the data set
- Salt blindness - An unknown fraction of muon follower neutrons (see 3.3.1) is artificially added into the data set with no muon follower tag associated with them.
- NC cross-sections rescaling - The NC neutrino cross-sections on deuteron are rescaled by an unknown factor, so the total flux predicted by MC is off by an unknown factor.

3.3.1 Instrumental events removal: Data Cleaning

Background events arising from instrumentation are one of the most dangerous backgrounds in SNO. These types of events come from misbehavior of the detector components (PMT tubes, electronics), and specific phenomena that are inherent to certain parts and/or operations of the detector, e.g. the "bubblers" following the recirculation of the water and the static discharges in the neck of the acrylic vessel. The first

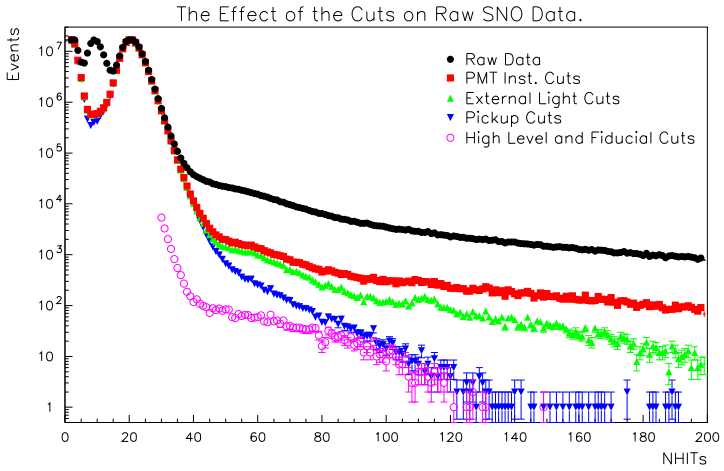

Fig. 3.2: Nhit distribution of the raw SNO data and the major selection steps towards a sample of neutrino candidates. Figure courtesy of N. McCauley

category above, in particular the so-called "flashers", which are most probably static discharges in the space between PMT dynodes, dominate the event trigger rate above the end of the low energy backgrounds [3] as can be seen in Fig. 3.2. Fortunately, they do have a very distinctive signature in charge and time, so can be efficiently removed from the data set.

The SNO DCWG ("Data Cleaning Working Group") put a large amount of effort in eliminating all the pathological events in our data. More than 20 cuts were designed based solely on "low level" quantities[4] for all types of pathological events observed. A list of the cuts used in this thesis, with a short description, is presented below:

- **Burst cuts**
  - **RETRIGGER** - A 5 μsec limit on consecutive events

[3] Roughly 30 hits

[4] Charge , time, and PMT hit pattern, with no resort to reconstruction or reconstruction specific quantities

- **NhitBurst** - Cuts any series of 6 events with more than 40 hits each in a time of 4 seconds or less.

- **Junk** Removes pathological DAQ events (orphans, see Sec. 2.5.3)

- **Timing cuts**
  - **FTS** - cuts events for which the median time difference between PMT pairs within 3 m of each other is greater than 6.8 ns
  - **ITC** - cuts events with less than 60% of the PMTs in a sliding window 93 ns wide

- **Hit pattern cuts**
  - **FGC** - cut events with a channel or PMT position cluster further away than 1200 cm in average from other PMTs
  - **CrateIsotropy** - cuts events with more than 70% of the hits in one crate and more than 80% of those hits are in two or fewer FECs

- **Muon follower cuts**
  - **MFS** - cuts all events for 20 s after an identified muon. It is effective in removing spallation events produced after a muon passes through the detector.
  - **MMFS** - cuts all events 250 msec after a 150 Nhit event. The reason for this cut is to remove spallation events produced after an atmospheric neutrino interacts in the detector. These events can not be cut by MFS since there is no muon tag associated with the first event.

- **Charge cuts**
  - **QCLUSTER** - A cut developed by the author, removes any event with a high charge[5] in a cluster of 4 hits. The "cluster" is defined as any 4 hits in a window 5 channels wide, sliding through every electronic FEC32 card.
  - **QvT** - Removes events with a maximum QH difference greater than 1000, or QL difference greater than 180 counts, from the average charge and hit at a time more than 60 ns earlier than the median time
  - **Q/Nhit** - Removes events with an average total charge per number of hit tubes less than 0.25 photoelectrons after the highest 10% of the charges were removed
  - **AMB** - The Analog Measurement Board (see 2.5.2) cuts events with the normalized AMB's integral or peak measurement of the ESUMHI signal more than 3.7σ away from the average for events with the same Nhit. This and the next two cuts rely on trigger signals rather than PMT or FEC information.
  - **ESUM** - cuts events which have the ESUMHI trigger fired
  - **OWLEHI** - cuts events which have the OWLEHI trigger fired

3.3.2 Instrumental events removal: High Level Cuts

For the post-reconstruction stage, another set of cuts (HLC-high level cuts) have been developed in order to further reject any possible leakage of non-physics events in our data set. There are two such cuts used in this thesis. **ITR**(In Time Ratio),

[5] QH>2000 and QL>300

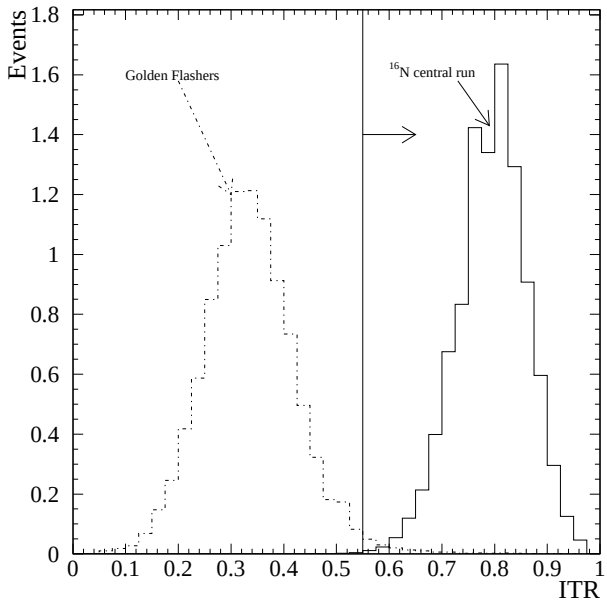

Fig. 3.3: ITR distribution for golden flasher and ^{16}N events.

a parameter developed by the author, is a very simple, yet a very powerful test on reconstruction and instrumental events. The ratio of number of hits in the $(-2.5, 5)$ ns around the fitted event time, to the total number of hits, is calculated and the event passes if this ratio is above 0.55. Since not all the timing effects (TSLH being one of them) are in the MC, the ITR distribution is poorly reproduced by the simulation so it became necessary to place a loose cut so the acceptance is very close to 100%. The typical ITR distribution is shown in Fig. 3.3 on an ^{16}N run together with the distribution for the "golden flashers" which is a hand-scan selected flasher data set.

The second HLC is $\langle\theta_{ij}\rangle$. This is the average tube-to-tube angle as viewed from the fitted position. In a "perfect world", without scattering, the electron will generate a perfect 42° cone, so the tube-to-tube distribution will have an excess at 42° which

Analysis step	Number of events
Total event triggers	435721068
Neutrino data triggers	196417438
$N_{hit} \geq 20$	55446430
Instrumental background cuts	50912120
Muon followers	50030032
High Level Cuts	37913558
Fiducial volume cut	549900
Energy threshold cut	2729
Total Events	2729

Table 3.1: Data reduction steps

will drive the average angle towards higher values[6].

3.3.3 Signal box definition

Having all the tools mentioned before in place one can define the so-called "signal region". This will represent a collection of events which are suitable neutrino candidates. The first step in the data reduction scheme is to select just events that pass the "neutrino trigger", which is the *NHIT_100_MED* (Sec. 2.5.2). Then we apply the Data Cleaning cuts and High Level Cuts. A graphical description of the signal box is shown later in Fig. 5.3 (Sec. 5.1). In the end, we restrict the fiducial volume to 500 cm in order to move away from backgrounds originating from outside of the D_2O , and an energy threshold of 5 MeV to keep the radioactive backgrounds at a low level (Ch. 5). The number of events kept in the data set after each step is presented in Table 3.1.

[6]Clearly, most of these angles will be close to zero, for simple geometric reasons only

Ch. 4

PDF Shapes and Acceptances

The ultimate goal of the SNO solar neutrino analysis is to extract the three signals of interest, Elastic Scattering (ES), Neutral Current (NC) and Charged Current (CC). These can be then compared with the model predictions and also against each other, in order to establish the quantities that will be used later in determination of neutrino properties. To extract signals, one needs to know their distinguishing characteristics. In order to separate them. In SNO, these characteristics are the shape of certain distributions (energy, hit patterns, angle between the reconstructed direction and the Sun and vertex radius). To obtain shapes, one can use models of the detector (Monte-Carlo, analytical parameterizations, calibration) and then estimate the uncertainties on these shapes. It goes without saying that, ideally, one would want to understand these shapes using a small number of variables, so that the number of correlations are reduced and the treatment of uncertainties can be done in a manageable way[1].

[1] A perfect example here is the energy distribution. If we make the assumption that the detector response is Gaussian, one would need only two parameters to describe the energy shape of a certain signal: the scale (the mean of the mono-energetic Gaussian response) and the resolution (the width of the Gaussian response). The final shape of that particular signal will be then the convolution between the energy distribution of the signal and the Gaussian response of the detector. This

Besides shapes, to obtain a meaningful physical result, one also needs to determine the correct acceptances for the signals. This is usually done using Monte Carlo; given the number of extracted events in the signal region, what is the neutrino flux that would produce this number of events? The crucial point here is that one needs to make sure that the relation between the acceptance of a particular signal, as predicted by MC, and reality is known, and the uncertainties are well understood.

There is always a direct comparison which can be done between MC and calibration to determine how well the simulations describes reality. The calibration source are designed specifically to test specific signal features so the data-MC comparison is meaningful, allowing one to validate the interpolations that the MC does to obtain the final shapes and acceptances. In this sense, the MC is "over-constrained" by calibration.

Comparing with the pure D_2O phase, there are several changes worth noticing. The energy released after a neutron capture increases, which increases the number of events above threshold. The neutron capture efficiency is larger which also improves the statistics on the NC determination. The increases in the capture efficiency "flattens out" the radial distribution, so there is a loss of information here, especially for a restricted fiducial volume. Last, we can use the geometrical pattern of the PMT hits to distinguish between CC and NC events (see 1.3.2).

4.1 Energy scale and resolution

We will make the assumption that away from the trigger threshold the energy response of the SNO detector is well represented by a Gaussian distribution. Although this

convolution, of course, could be done analytically, or using Monte Carlo

assumption is well supported by Monte Carlo, as shown in Fig. 4.1, there is no real way to verify this, since we do not have a mono-energetic electron source during salt phase[2]. Nevertheless, the agreement between all the sources deployed and the MC simulation of the sources is in very good agreement (as shown in Fig. 4.2), which indicates that the fundamental energy response in MC is correct. It should be noted here that in the energy regime for solar neutrino analysis, SNO signals span the whole energy response, so perfect understanding of the tails of the resolution is not crucial. The problem is more acute in the estimation of backgrounds. However, the background analyses are either done, or checked, by background calibrations, as will be described later. Also, the energy threshold for the analysis is chosen so that the backgrounds are kept at a very low level.

The width of the mono-energetic response is taken to be the fundamental energy resolution of the detector. This way, to completely describe the energy distribution of a signal, we need, aside from the fundamental physical description of processes, two parameters (the scale and the resolution) and the correlation between them. The latter is shown in Fig. 4.3 as the dependence of the resolution on energy and could be described by a formula:

$$\sigma_E(E) = -0.3836 + 0.4873\sqrt{E} + 0.02614E \tag{4.1}$$

where E is the total energy of the electron[3].

The primary energy calibration for SNO is the triggered ^{16}N source (Sec. 3.1.2).

[2]This is not strictly true since during the D_2O phase a 19.9 MeV γ source (pT) was deployed. Unfortunately, the statistics collected were rather low for a useful check of the long tails in the energy distribution

[3]$E = T + mc^2$, T being the kinetic energy of the electron, m its rest mass and c the speed of light in vacuum

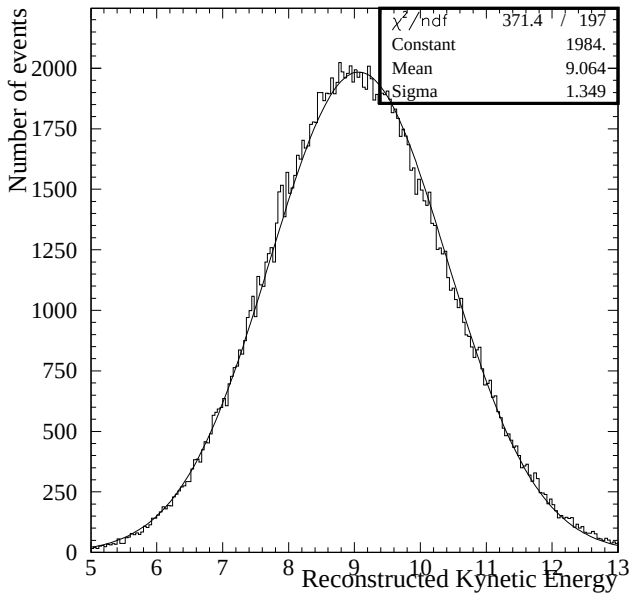

Fig. 4.1: Gaussian fit to the MC 9 MeV electrons generated uniform and isotropic in the D_2O volume.

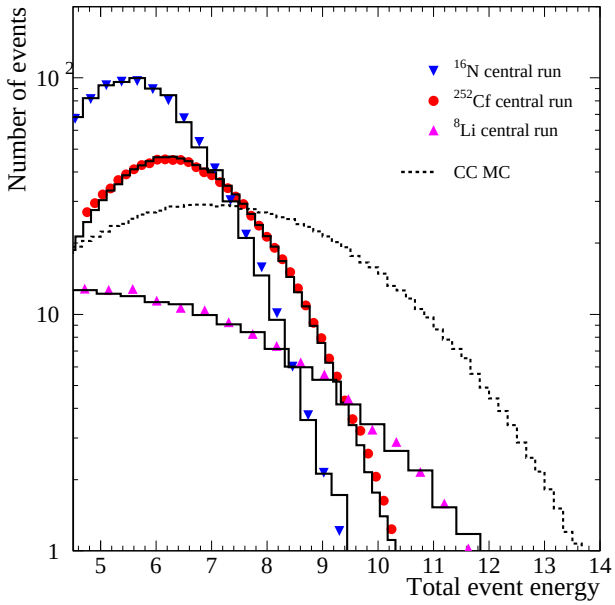

Fig. 4.2: MC simulation of energy distribution for several sources deployed by SNO. The CC MC is also showed for reference

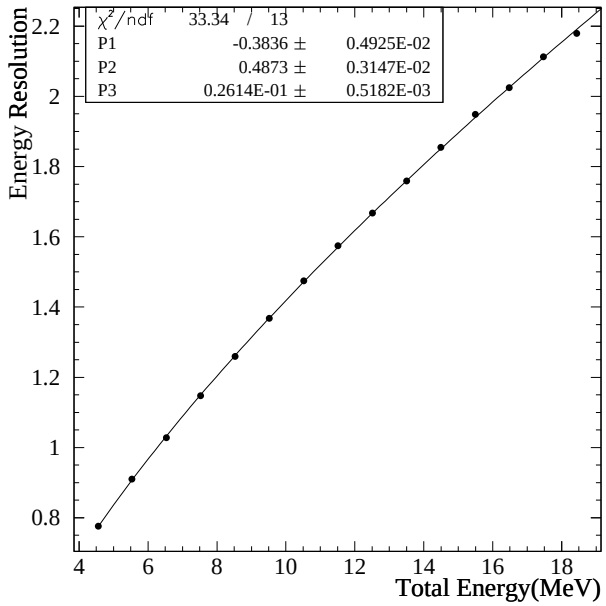

Fig. 4.3: Energy resolution as a function of energy for mono-energetic electrons generated uniform and isotropic in the D_2O. The MC was generated under the same conditions as the neutrino runs throughout the livetime.

The number and energy of produced γ 's in the ^{16}N decay is shown in Fig. 4.4. Since the 6.13 MeV γ ray dominates, one can approximate this with a mono-energetic γ source. However, the detection of γ's in SNO is done via Compton scattering on electrons. Although most of the time the only electron above the Cherenkov production threshold is the one from the first hard scattering, the energy distribution of the electrons "produced" by the ^{16}N source will have a Compton scattering profile, rather than being mono-energetic. Under the assumption that:

- The MC reproduces correctly the Compton scattering distribution.
- The fundamental energy response is Gaussian, therefore the only parameters needed are the scale and the resolution.

we can fit the ^{16}N energy distribution with a function of choice and compare the free parameters in the fit between data and MC. It turns out that over the "peak" of the ^{16}N energy distribution we can fit a simple Gaussian, so we will consider the mean of this Gaussian to be a measure of the scale and the width (a measure of the energy resolution).

4.1.1 Energy scale and resolution uncertainties as derived from ^{16}N source

During the salt phase, the calibration group performed several ^{16}N scans[4] throughout the detector volume, as well as periodic "stability runs"[5]. The scans can be used to assess the uncertainty on the overall energy scale inside the fiducial volume using a volume weighting algorithm as in Eq. (4.2).

[4] These are usually relatively short runs taken at different positions
[5] Long runs taken at the center of the detector

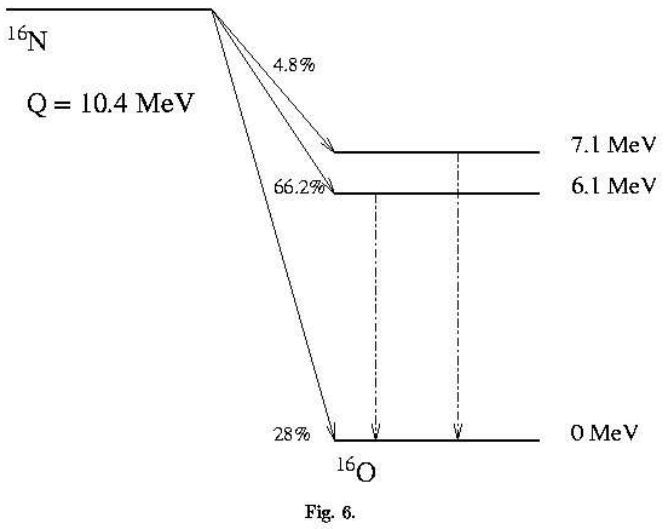

Fig. 4.4: The ^{16}N decay scheme.

$$\overline{E} = \frac{\Sigma_i w_i E_i}{\Sigma_i w_i} \tag{4.2}$$

where E_i denotes the measured energy at a certain position i and w_i, the volume represented by the position i. A large number of systematic effects related to the energy scale were investigated in [42] and the overall systematic uncertainty for the energy scale was determined to be 1.1%. The largest contributors to this are the source effects, like its geometry and optics, and the asymmetries in the detector. The same method can be used for resolution to obtain an uncertainty of 3.5%, where we have neglected any dependence of resolution uncertainty on energy[6].

[6]The SNO collaboration derived actually an energy dependent resolution uncertainty, but throughout the energy range we are interested in, the correction turns out to be relatively small

Stability of the energy scale

During the D_2O phase it was found that the energy response of the detector as derived from ^{16}N source was slowly dropping at a rate of about 0.5% a year. At the time, no explanation was found and the analysis carried on by using an empirical linear drift derived from ^{16}N to correct for this change. When salt was added, in June 2001, there was an abrupt change in the energy scale for the first 2-3 months of $\sim 2.5\%$. After that, the drift stabilized at $\sim 1.7\%$ a year. At the current level of understanding, it seems that the effect is due to degradation in the reflectors angular response and changes in D_2O attenuation lengths. This variation in energy scale is accounted for in MC by drifting the D_2O attenuation lengths according to the drift formula derived from ^{16}N . After this correction has been applied, the trends in energy scale as derived from the ^{16}N source, throughout the salt phase, are shown in Fig. 4.5. Also, for completeness, we show similar trends, as obtained from low rate ^{16}N runs which were taken to check any potential differences due to rate effects.

The data during the first three months, when the energy scale of the detector is still not yet completely understood, will be discarded in this thesis. The uncertainty assigned to the energy scale from time variations is derived as in Fig. 4.6. There we combine the fractional difference between ^{16}N data and MC in bins 50 days wide and fit a constant through lifetime. The uncertainty on that fit will be included in the overall energy scale uncertainty.

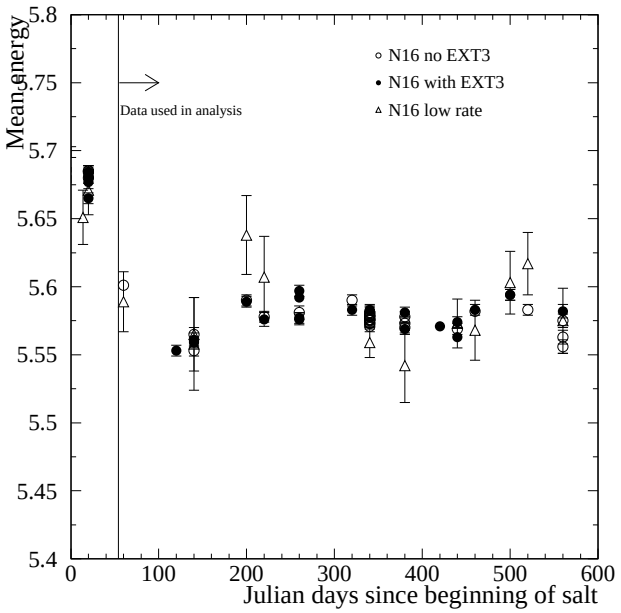

Fig. 4.5: Energy stability after all the corrections have been applied. Shown are different conditions under which ^{16}N is taken.

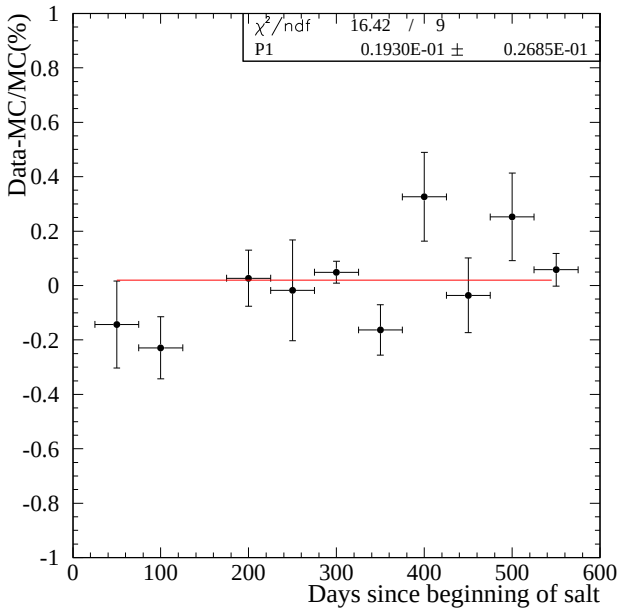

Fig. 4.6: Stability of the energy scale relative to the MC simulation. The data has been combined in bins 50 days wide.

4.2 Reconstruction uncertainties

The properties of the reconstruction algorithms in SNO have been intensively studied before ([41], [43], [44]) so we are just going to outline the main uncertainties related to the number of events reconstructed inside a fiducial volume of choice.

4.2.1 Vertex Shift and resolution

The vertex reconstruction response can be parameterized as a simple Gaussian:

$$R(x, \sigma, \mu; x_0) = \frac{1}{\sqrt{2\pi\sigma}} e^{-\frac{[(x-x_0)-\mu]^2}{2\sigma^2}} \tag{4.3}$$

where x represents the reconstructed position of the events, x_0 the real position of the events, μ the vertex shift and σ, the vertex resolution. The typical vertex displacement (defined as $R_{fit} - R_{true}$) for fitters in SNO is of the order of 1 cm per each 1 m from the center of the detector. The resolution of the reconstruction algorithm is of the order of 17 cm throughout the energies of interest.

The effect of any uncertainty in the vertex shift and the vertex resolution on the measured neutrino fluxes will be similar to the effect of the uncertainty energy scale and energy resolution. Any mismatch between MC and reality will result in an overestimate/underestimate of the acceptance to a particular signal. ^{16}N scans and ^{8}Li source data (3.1.2) were used to determine potential systematic effects in reconstruction by convolving the basic reconstruction response with the spatial distribution of the electron from the source. In [44] the systematic uncertainty in vertex shift has been found to be 1% and that in vertex resolution 15%. The effect of these systematics on the flux measurement will be estimated in Ch. 7.

Parameter	Uncertainty
α_M	11%
β_S	9.5%
β_M	4.2%

Table 4.1: Systematic uncertainties on the angular resolution parameters as derived from ^{16}N scans. Table taken from [43].

4.2.2 Angular resolution

For the angular resolution studies we can use the resolution function described in [45]:

$$P(\cos\theta) = \alpha_M \frac{\beta_M e^{\beta_M(1-\cos\theta)}}{1-e^{-2\beta_M}} + (1-\alpha_M)\frac{\beta_S e^{\beta_S(1-\cos\theta)}}{1-e^{-2\beta_S}} \tag{4.4}$$

where the first term describes the sharp peak in the angular distribution (the actual resolution of the detector) whereas the second term, models the long tails mostly due to multiple scatterings. α_M describes the relative fraction of the two. The volume weighted mean difference between data and MC for a ^{16}N scan for each of the three parameters in (Eq. (4.4)) is taken as the systematic uncertainty as shown in Table 4.1

4.3 Hit pattern to distinguish CC and NC events

The addition of salt made possible the neutron capture on ^{35}Cl rather than on deuterium. This had three consequences; first, the neutron capture cross-section increased, second, the total energy of the γ 's produced is higher and third, most of the time, for each neutron captured, there were 2 or more γ 's emitted during the de-excitation of ^{36}Cl. The statistical separation between CC and NC events could therefore be improved by considering a variable that takes into account the isotropy of the hits in the detector. We expect the neutron events to have a more isotropic

distribution of hits than the electron events, since there are multiple γ 's in different directions present.

The SNO collaboration has tried a large number of parameters that made use in different ways of the isotropy information in order to achieve the best possible separation between CC and NC events. In the end, it turned out that very little, if anything, can be gained in using more complicated schemes instead of the simplest of them all: the average angle between all the possible pairs of hit PMTs in the events with respect to the reconstructed event position. This parameter, called $\langle\theta_{ij}\rangle$, will be used as the isotropy statistic in this thesis. The only real advantage it has over the rest of the parameters developed is its simplicity.

It has been found, through Monte Carlo simulation, that the statistical resolution of the algorithm used to separate the signals in SNO does not get worse as we decrease the number of bins in the $\langle\theta_{ij}\rangle$ distribution. Consequently, in the interest of keeping the number of parameters that need to be investigated small and also the number of correlations between them at a minimum we will use just two bins for $\langle\theta_{ij}\rangle$. In that case, the only quantity that needs to be studied is the relative height of these two bins. The boundary between the two has been chosen at 1.22, based on Fig. 4.7

Quantitatively, the parameter we propose to investigate will be the ratio between the number of events in the first bin, and the total number of events in the $\langle\theta_{ij}\rangle$ distribution (from now on we will call this $\langle\theta_{ij}\rangle$ ratio).

4.3.1 $\langle\theta_{ij}\rangle$ ratio modeling in Monte Carlo

Since we will use MC to reproduce two of the three signals, one has to understand how well the MC should be expected to simulate reality. Again, there is no neutrino source

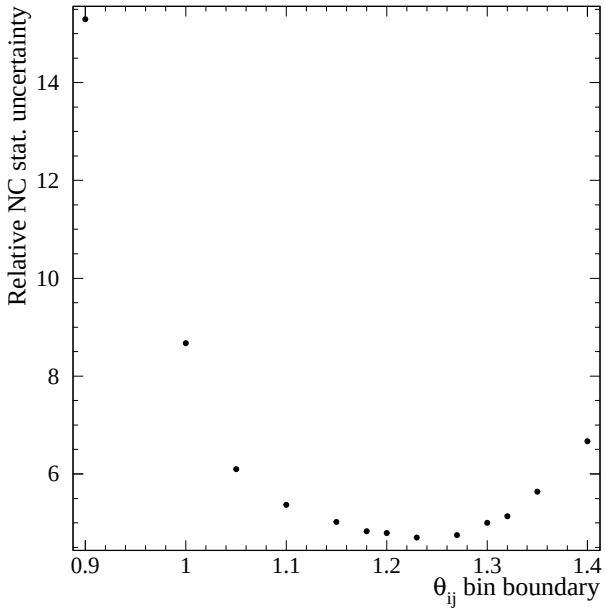

Fig. 4.7: Relative statistical uncertainty in the extracted NC flux as a function of the boundary between the two bins used in the extraction algorithm. This is based on 300 MC simulated data sets.

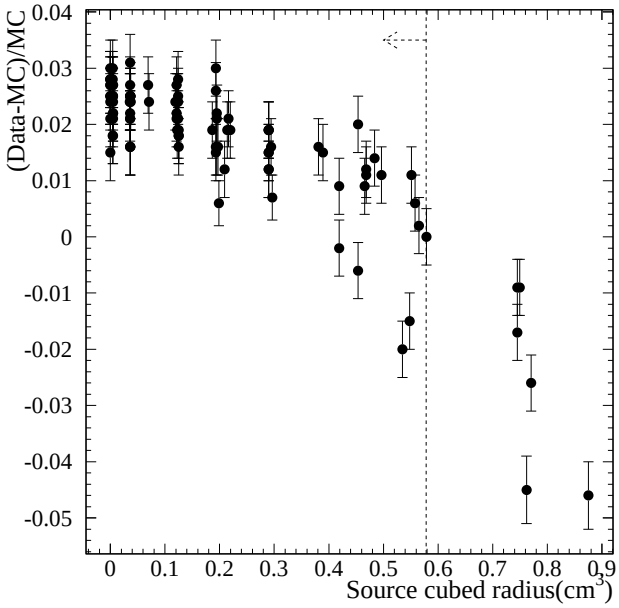

Fig. 4.8: Fractional difference in the $\langle\theta_{ij}\rangle$ ratio between data and MC at different points in the volume. The 550 cm fiducial volume is shown as the dashed line

for an ultimate calibration, therefore we will determine the uncertainties on $\langle\theta_{ij}\rangle$ from ^{16}N and assume they are valid throughout the energy regime. The procedure to determine the uncertainties will be relatively similar to the one used for energy. Fig. 4.8 shows the difference between data and MC for an ^{16}N scan. It is obvious that there is a differential error of the model in approximating the reality, between the center of the detector and regions closer to the AV.

To determine the volume weighted uncertainty, we will first consider the weighted average difference between data and MC as in (Eq. (4.5)).

$$\Delta\bar{\mu} = \frac{\Sigma_i \frac{V_i}{\sigma_i^2 N_i}\left(\frac{Data_i - MC_i}{Data_i}\right)}{\Sigma_i \frac{V_i}{\sigma_i^2 N_i}} \tag{4.5}$$

where i represents the i'th run used, V_i, the volume represented by that run, N_i,

the number of runs for that volume and σ_i, the statistical uncertainty on the i'th determination.

The uncertainty on this difference will be calculated in a volume weighted way as:

$$\sigma\mu = \frac{\Sigma_i \frac{V_i}{\sigma_i^2 N_i} (\frac{Data_i - MC_i}{Data_i})^2}{\Sigma_i \frac{V_i}{\sigma_i^2 N_i}} \tag{4.6}$$

When all the positions in Fig. 4.8 are combined, the difference between data and the MC model is $0.7\% \pm 1.9\%$. We will assign 1.9% systematic uncertainty to the $\langle\theta_{ij}\rangle$ ratio as a result of detector asymmetries.

4.3.2 Stability of the $\langle\theta_{ij}\rangle$ ratio

We can use the central ^{16}N runs to determine whether there are any variations in the $\langle\theta_{ij}\rangle$ ratio. Fig. 4.9 shows no time dependence within the statistical uncertainties. To obtain that plot we combine the ^{16}N central runs in bins 50 days wide. In the same figure, there are shown separately, the runs taken at high rate and the runs taken at low rate in order to measure any potential rate dependence problems (TSLH). The difference between high rate and low rate is within the expected statistical variations.

4.3.3 Energy non-linearities in $\langle\theta_{ij}\rangle$ ratio

We tested the MC model for $\langle\theta_{ij}\rangle$ at the ^{16}N conditions. To ensure that the model does not break down at higher energies, or different angular distributions we show in Fig. 4.10 the comparison between data and MC for several energies and angular distribution regimes.

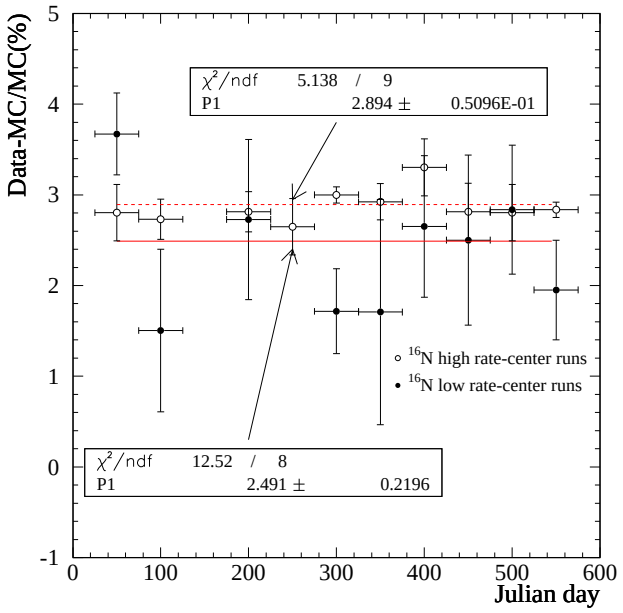

Fig. 4.9: Stability of $\langle\theta_{ij}\rangle$ ratio with time as obtained from *central* ^{16}N runs. The runs are combined in bins 50 days wide.

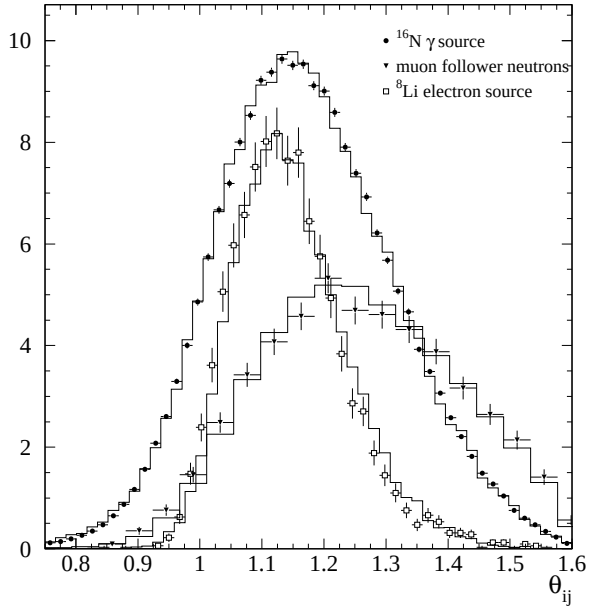

Fig. 4.10: $\langle\theta_{ij}\rangle$ agreement between data and MC for ^{16}N , ^{8}Li sources and for muon follower neutrons (see Sec. 4.4)

4.4 A "perfect" NC calibration

In order to calibrate the detector for a certain signal one would like to have a calibration source that produces events that look exactly as the signal one tries to calibrate. The ideal calibration for an experiment like SNO would be a neutrino source, producing a known flux comparable to the Sun. Unfortunately, this is very hard or impossible to achieve. For the CC and ES signals, the SNO experiment uses a variety of calibration sources and interpolates/extrapolates using MC. This has the inherent problem of point sources, as the events they produced are not distributed as the signals in volume, and calibration can be taken only at certain times. Also, for SNO, the calibration time and neutrino data taking time never overlap.

For the NC neutrons, on the other hand, there is a continuous source, that would give a very similar spatial distribution (within statistics) as the signal. This perfect calibration is the neutrons produced by muons originating in cosmic ray interactions in the upper atmosphere. As the muon propagates it will generate bremsstrahlung photons. The photons with energy higher than 2.2 MeV can photodisintegrate a deuteron, hence, the neutron production. From now on, we will call these neutrons "muon followers". During the salt phase, there are two facts that a muon follower analysis can take advantage of; one, the capture time is much shorter ($\sim$ 5.5 ms) than in the pure D_2O phase ($\sim$ 40 ms), which allows for almost a background free identification of the neutrons and second, the capture efficiency is higher than in the D_2O phase, which allows for a more statistical significant measurement. Neutrons obtained from a muon follower analysis have the extremely desirable feature in being, to a very large extent, identical to whatever signal we get from the NC interaction.

There are multiple advantages in using the muon follower calibration has over any

other source calibration. The neutrons obtained from muon followers are distributed in volume in the same way as the neutrino produced neutrons. They span precisely the same time interval as the neutrino data. The continuous flux of muons ensures that there is no aliasing effect that would somehow offset the calibration with respect to the neutrino data.

4.4.1 Selection criteria for muon follower neutrons

In order to select a sample of muon followers in salt we perform a first scan on the data to identify the muons. An event is classified as "muon" if the following conditions are fulfilled:

- There are at least 150 hit PMTs
- at least 5 OWLs fired
- It does not fail the data cleaning "neck cut"
- The most recent event with more than 5 OWLs fired was more than 5 μs ago.
- The RMS time of the normal PMTs that fired is less than 90 ADC counts
- Is not an "orphan"[7]
- Is not a **PEDESTAL**, **EXTERNAL_ASYNC** or **PULSE_GT** trigger

These are very simple criteria, but they are optimized for a large acceptance for muons, at the expense of large contribution from other type of events[8].

[7] see Sec. 2.5.3

[8] Mostly "instrumental" backgrounds, especially large pickup in the front end electronics

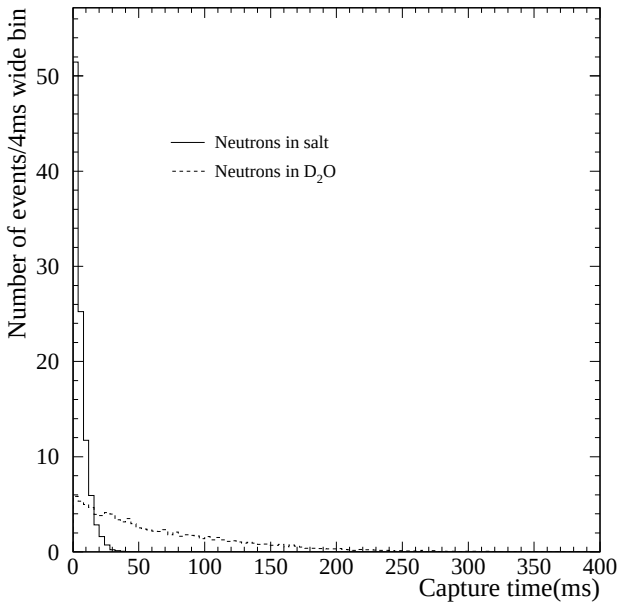

Fig. 4.11: Time between the neutron generation and neutron capture in salt (continuous line) and D_2O (dashed line)

Every event occurring within 20 ms after the muon is counted, and for each muon, a multiplicity number (the number of followers for the current muon) is saved. The 20 ms window in chosen in order to minimize the backgrounds in the window and to ensure the maximum acceptance for neutrons. The choice is justified by a Monte Carlo study, as in Fig. 4.11, which shows the time in ms between the neutron generation and neutron capture in salt and D_2O.

Events obtained in this manner are passed through the Data Cleaning cuts (excluding the burst cuts) and the ITR cut. The left side of Fig. 4.12 shows the distribution of those events in $\langle\theta_{ij}\rangle$ and energy. Clearly, two classes of events can be distinguished here. The high energy and $\theta_{ij} > 1$ (identified as neutrons) vs. low energy events (external $\beta - \gamma$). Indeed, a 600 cm cut considerably cleans up the neutron

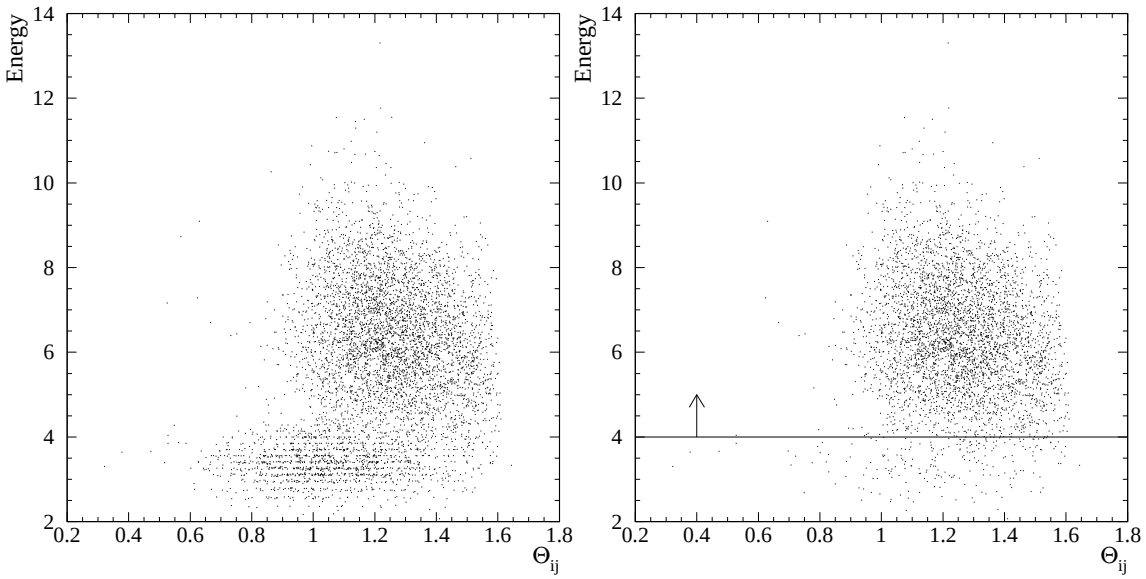

Fig. 4.12: *Left*: Sample of muon followers without a radial cut. *Right*:Sample of muon followers with a 600 cm radial cut. The line indicates the analysis threshold

sample as shown in the right side of Fig. 4.12.

In order to further reduce any contamination from low energy non-neutron events, we impose an energy cut of 4 MeV. Also, to reject any events resulting from prompt γ's and re-triggers due to very energetic events passing through the detector, the time difference between the muon and the selected event is required to be more than $50\mu s$. With a LOCKOUT (see Sec. 2.5.2) of $\sim$ 400 ns this allows a 100 events buffer.

One potential problem posed for this analysis are muon events which produce a large number of neutrons. Keeping those events in, will bias the result towards specific regions in space and time. The number of followers per muon candidate, for the selected sample is shown in Fig. 4.13. For all variables of interest we will compare the value of the variable for all events up to a multiplicity[9] of 20 to events that have

[9]This multiplicity distribution is not the distribution of neutrons following a muon in SNO because there is a large contribution of non-muon events in our muon candidate sample. This will strongly bias this distribution towards low values

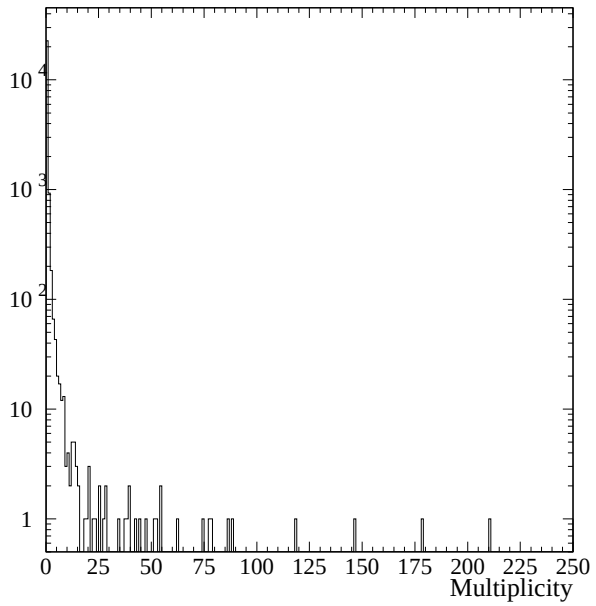

Fig. 4.13: Multiplicity distribution for the selected events

a multiplicity greater than 20.

4.4.2 Muon follower distributions

We show in Fig. 4.14 the volume distribution of neutron candidates selected from the muon follower sample. The are no regions of high density, which indicates that the selected events are relatively uniform so we should not expect any strong bias towards certain regions of the detector.

For the same bias reasons, we can repeat the same procedure for $\cos\theta_{\odot}$ and the resulting distribution is shown in Fig. 4.15 compared with the flat line from MC. We can compare these distributions using the Kolmogorov-Smironov (KS, [46]) test to get a probability that the two shapes are being drawn from the same distribution of 0.71.

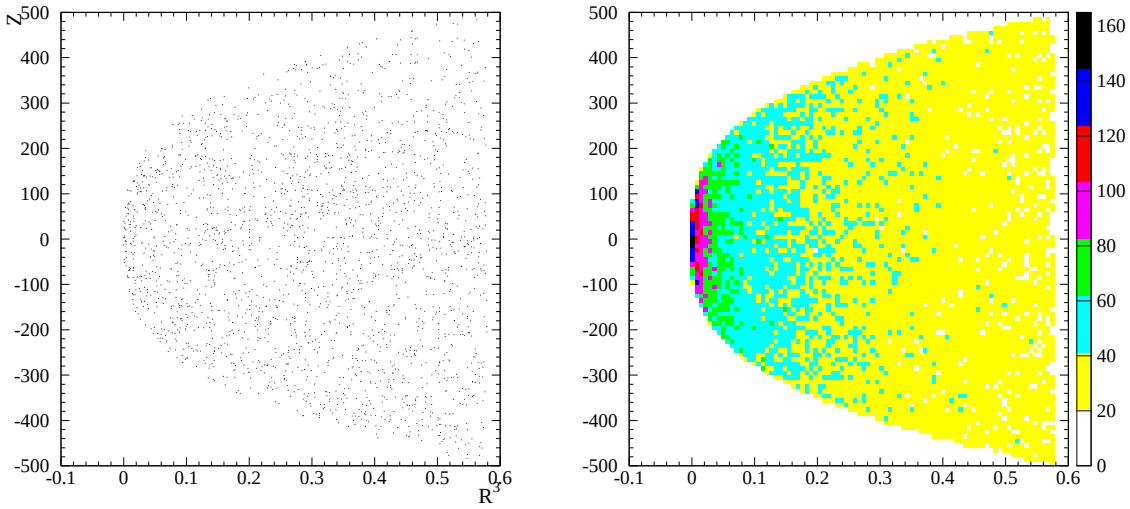

Fig. 4.14: The uniformity of the selected "muon follower" candidates in z and R^3(left). Comparison with the MC simulation of NC neutrons is shown to the right side.

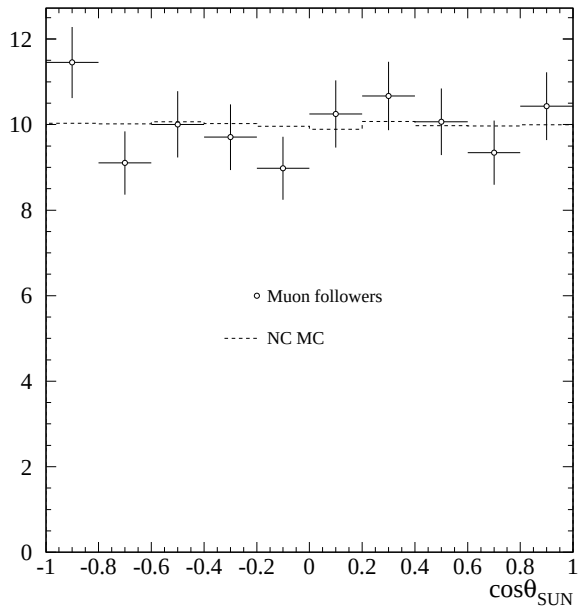

Fig. 4.15: $\cos\theta_\odot$ distribution for muon followers and NC MC

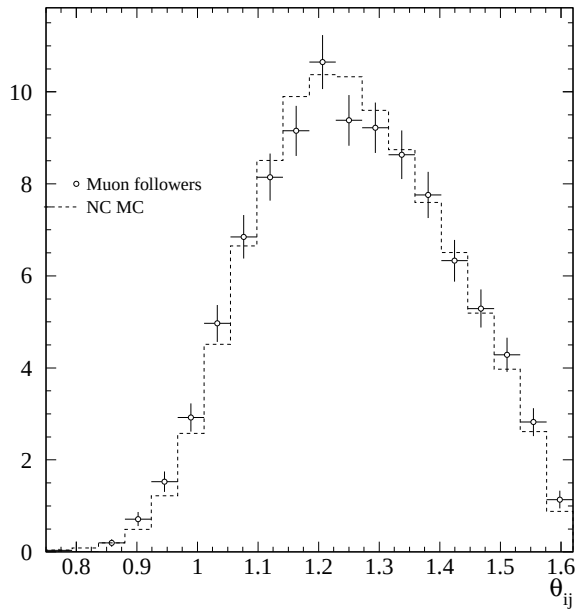

Fig. 4.16: $\langle\theta_{ij}\rangle$ distributions for muon followers and NC MC

We can also check the isotropy distribution by looking at the $\langle\theta_{ij}\rangle$ parameter. This is shown in Fig. 4.16 and the KS probability is 0.57.

4.4.3 How perfect is a "perfect" calibration?

The muon followers, as mentioned above, should be in principle the best representation of the NC neutrino signal in SNO. There are, still, certain effects, that could make certain quantities different between neutrons from neutrinos and muon follower neutrons. In this section we will concentrate on how precisely we can determine the energy scale from muon followers. There are a total of four systematic effects that we will list below:

- **Backgrounds**. There are two types of backgrounds one should consider in this analysis. First, accidental backgrounds are events that leak in our analysis window from usual events in the detector (radioactivity, high energy γ's, etc.). There are also spallation backgrounds, mostly γ's and $\beta - \gamma$'s from spallation nuclei produced by muons.

- **TimeSinceLastHit (TSLH)**. Although we had a hardware fix for salt in place, to deal with this effect (the fans), right after the muon there is a high rate/high load affecting subsequent events. This should not affect the radial distribution much, but could potentially distort the energy distribution.

- **High energy neutrons**. Unlike the NC neutrons that are in the keV range, the muon follower neutrons are produced at higher energies. Although they thermalize before they capture, there might be distortions in the radial profile because of fast neutrons that leave the D_2O near the AV. This could affect the energy distribution indirectly.

- **Multiplicity bias**. As can be seen in Fig. 4.13 we do have very high multiplicity events in the data set. Between all the distributions used in the signal separation there is a potential correlation. The isotropy parameter, for example, is strongly correlated with energy and it also shows, to a smaller degree a correlation with radius. By including high multiplicity events, we will bias the distributions towards certain regions in space and time. Depending on the degree of correlation between the spatial position and a particular distribution we are interested in, we might bias that distribution by having events with specific radial profiles.

Backgrounds

- Accidentals

  The set of cuts applied, and the 20 ms window, should provide a reasonable rejection for potential coincidental backgrounds. In order to measure the size of coincidental backgrounds, we look in a 160 ms window **before** the muon candidate. There number of events passing all the cuts is 1.6 ± 0.4 events after scaling by a factor of 8 due to time window widths, or 0.07% or the total selected data set.

- Spallation

  - Spallation on Cl and Na

    As pointed out in [47], for 300 days, even if all the decay products from ^{23}Na, ^{35}Cl and ^{37}Cl were long-lived and produced a high energy γ, the total number of events would be 0.2, so we can neglect this completely.

  - Spallation on ^{16}O

    To estimate this background we fit for different components in the capture time distribution. Several long-lived isotopes can contribute as a background to our analysis window. The high statistics data from the Super-Kamiokande experiment has been fit ([48]) for the relative admixture of different isotopes with known half-life. The largest contribution has been found to come from a half-life of 11 ms and a lifetime of 20.4 ms. The 11 ms has been identified as ^{12}Be or ^{12}N with a β end-point of 11.66 MeV and 16.38 MeV. The 20.4 ms can be attributed to ^{12}B with a β end-point of 13.37 MeV. The relative amplitudes for these two first two dominant

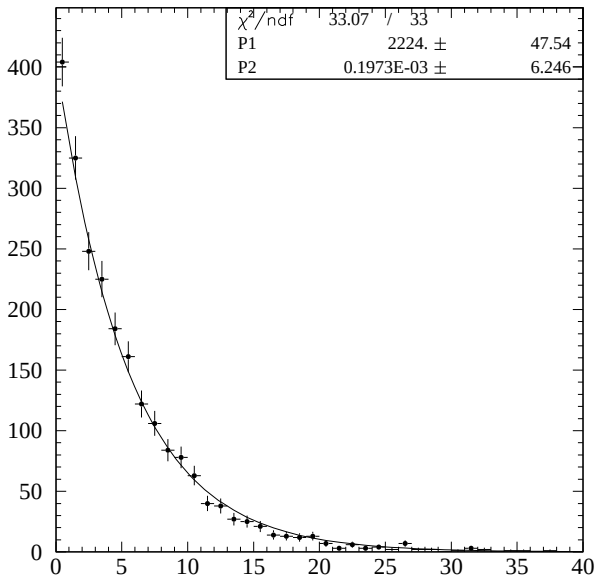

Fig. 4.17: Fit for the number of spallation background on ^{16}O in capture time distribution

components as obtained in the Super-Kamiokande data, are 22% for the 11 ms half-life and 78% for the 20.4 ms half-life. All other possible decay products are long lived, therefore, will have a smaller contribution into our time window and according to the relative admixture obtained in [48] they also have much lower production cross-sections than the ones from above. The function we fit to will be:

$$f(t) = \frac{n_1}{5.4612} e^{(-\frac{t}{5.4612})} + \frac{n_2}{26.45}[0.78e^{(-\frac{t}{29.43})} + 0.22e^{(-\frac{t}{15.87})}] \qquad (4.7)$$

where $n1$ in the number of neutrons and $n2$ is the expected background from spallation. As seen in Fig. 4.17, the $n2$ parameter ends up at zero with an uncertainty of 6 events and 24% covariance between the two parameters.

To estimate the effect of the backgrounds, we will take 6 events drawn randomly from the CC distribution and add them on top of 1750 events drawn randomly from the NC distribution in 400 hypothetical experiments and compute the average deviation in the distribution of the means and RMS's. We use CC MC, since the background is expected to have the β endpoint close to the endpoint of the CC energy distribution. The changes obtained are 0.1% for the mean and 1% for RMS. We will use these numbers as uncertainties on the scale and resolution due to the spallation backgrounds. The estimated effect on $\langle\theta_{ij}\rangle$ ratio due to background contributions was found to be negligible compared to the statistical uncertainties of the muon follower PDF.

– Neutrons produced in the outer regions.

  Although our analysis restricts the fiducial volume to 550 cm there is a possibility that neutrons created in the light water and other outer regions of the detector are propagated inside the analysis region. This could affect the energy and $\langle\theta_{ij}\rangle$ distribution in second order through slight changes in the radial profile. To estimate this effect we measure the deviation of the mean energy at two critical points from the center of the detector using the ^{252}Cf source. The deviation at +536 cm is +0.2% and at -548 cm is -3%. We can imagine a very pessimistic scenario in which the deviation from zero in the mean energy will be linear from -548 cm to the center and from the center to +536 cm. The slopes of the two lines will obviously be different.

  One can fit the z-distribution of the muon followers with a second order

polynomial and after proper normalizations calculate the mean deviation from zero throughout the detector volume by multiplying the z-distribution with the linear form derived above and integrate from -550 cm to 550 cm. We repeat the whole procedure by using the NC MC z-distribution. The difference obtained in the two ways is $< 0.02\%$. The effect on $\langle\theta_{ij}\rangle$ was also calculated in a similar manner and was found to be negligible.

- TSLH (Time Since Last Hit)

  To determine the size of the TSLH systematic we can fit a Gaussian to the prompt peak of the time residual distribution (as shown in Sec. 3.2.1) to get for the muon followers: $\mu = 1.161 \pm 0.003$ ns and $\sigma = 1.644 \pm 0.004$ ns and for the neutrino data $\mu = 1.091 \pm 0.007$ ns and $\sigma = 1.709 \pm 0.008$ ns for the neutrino data set. The reason for this discrepancy is two-fold. One, there is a small difference in the time residuals between neutrons and electrons, since there are usually multiple γ 's involved in a neutron event, and two, the muon followers are affected by TSLH. To determine the effect this might have on the reconstructed energy, we adjusted the mean (by shifting) and the resolution (by Gaussian convolution) of the time residuals for the NC MC and recalculate NPROMPT[10]. The integrated effect of this adjustment came out to be 0.02% on the mean NPROMPT and 0.01% on the NPROMPT RMS. In conclusion, we can neglect the TSLH effect on the energy distribution obtained from muon followers.

- High energy neutrons

[10]The number of PMTs hit in a ± 10 ns window around the fitted event time

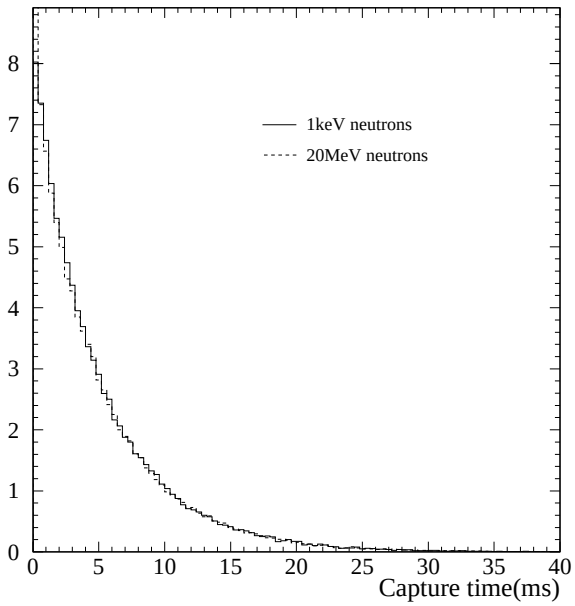

Fig. 4.18: The capture time for 1 keV and 20 MeV neutrons.

We consider the mean energy of muons in SNO to be ~ 300 GeV ([47]. Based on [49] we expect neutrons around of 10 MeV. To see how this will affect the relevant distributions we generate MC neutrons with 1 keV, which are closer to the neutrons obtained from NC neutrino interactions, and 20 MeV, which are specific for muon interactions. As seen in Fig. 4.18, the capture time for these neutrons is very similar, suggesting that the capture happens long after the thermalization occurred. Fig. 4.19 shows the difference in radius between true MC capture points in the two cases. Whatever small difference is present here, it becomes completely washed out by the reconstruction, as seen in Fig. 4.20. In what follows we will completely neglect this effect, as a potential source of systematics.

- Multiplicity bias

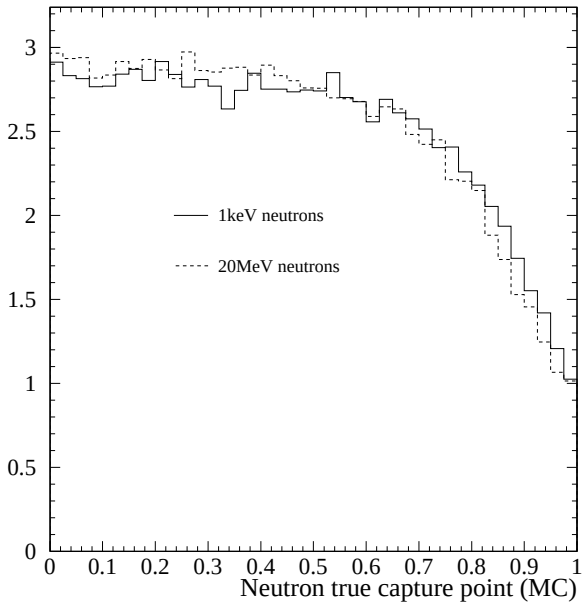

Fig. 4.19: The MC "true" generated capture position for 1 keV and 20 MeV neutrons.

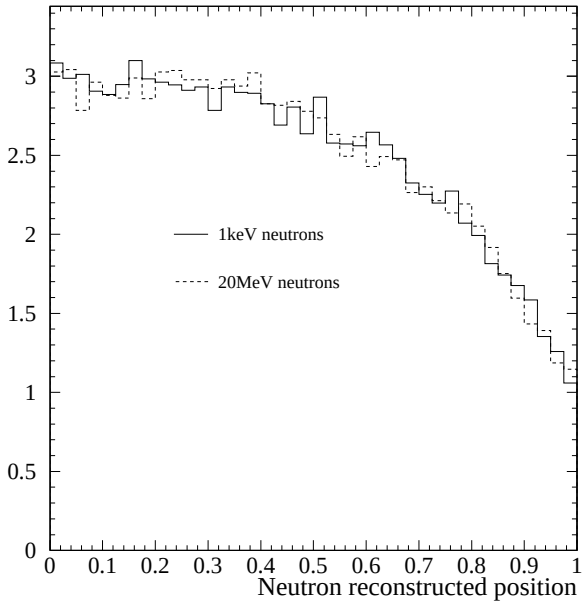

Fig. 4.20: The MC reconstructed capture position for 1 keV and 20 MeV neutrons.

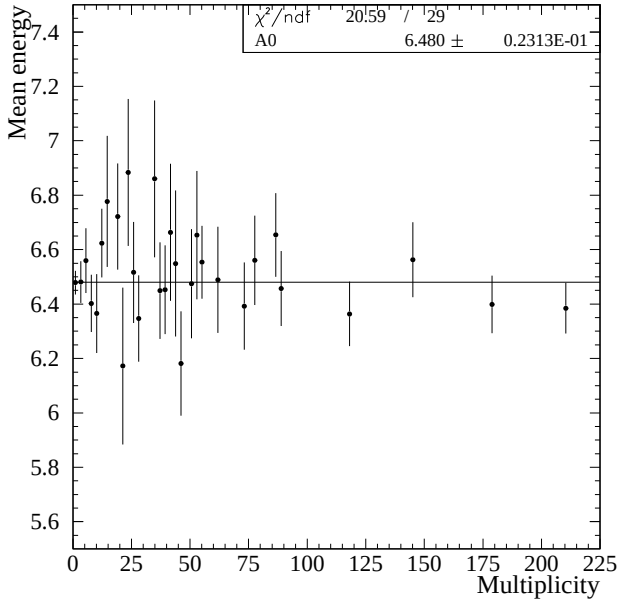

Fig. 4.21: Mean energy for each multiplicity.

The multiplicity (see Fig. 4.13) bias is the most difficult systematic we need to understand. This is partially due to the fact that we actually do not know the true distribution of neutrinos in the detector and partially due to a strong coupling between this systematic and the limited statistics of the muon followers/neutrino data sets. In order to get an insight on the magnitude of this effect, we plot in Fig. 4.21, the mean energy of the followers as a function of multiplicity, superimposed on fit with a flat line.

The uncertainty on the energy due to multiplicity biases is estimated by comparing the energy distribution below a multiplicity cut of 20 and above a multiplicity cut of 20. Based on this difference we assign a 0.1% uncertainty on the energy scale and 0.7% uncertainty on the energy resolution. We assign a 0.4% uncertainty on $\langle \theta_{ij} \rangle$ ratio due to multiplicity effects.

Systematic type	Effect on the scale	Effect on the resolution
Multiplicity	0.1%	0.7%
TSLH	0.02%	0.01%
Backgrounds	0.1%	1%
Total	0.14%	1.22%

Table 4.2: Table of systematic uncertainties on energy as determined with muon followers

If we put together all of the above, we get Table 4.2 for the energy scale and energy resolution uncertainties. Adding systematics and statistics in quadrature we obtain for the final energy scale 0.5%. The two energy distributions are shown in Fig. 4.22.

One can also check the stability of the energy scale using muon followers, although the statistics are not enough to be competitive with what was derived from ^{16}N. The energy stability as obtained from muon followers in shown in Fig. 4.23.

4.4.4 NC acceptance from muon followers

Although a useful quantity to have, the energy scale is not exactly the fundamental measurement that one needs to make in order to get the NC flux. A more useful quantity is the actual acceptance of the SNO detector to the NC events. In order to determine this we will assume, based on comparison with the calibration sources, that the MC correctly reproduces the gross features of the detector, as well as fundamental physics processes, and the small discrepancies due to subtle effects in the data, can be approximated as an extra convolution of the MC energy distribution. The second assumption is that the energy response to a single electron is Gaussian.

The first step in determining the extra convolution is to spline interpolate the energy distribution provided by MC inside a fiducial volume of 550 cm. We can

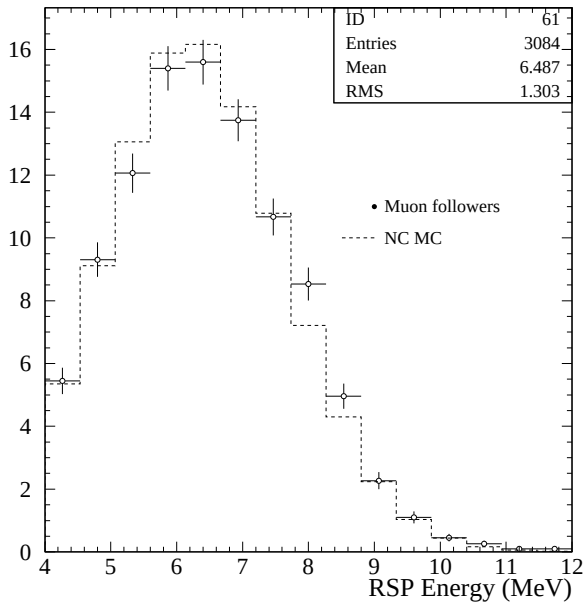

Fig. 4.22: Energy shape of muon followers and NC MC.

then fit for the convolution function, using the muon follower energy distribution. The parameters in the fit are the mean of the convolution Gaussian (scale) and the fractional difference in the resolution. The resolution is parameterized using MC as in (Eq. (4.1)) The convolution Gaussian has a width of $\sigma(E)((1+f)^2-1)$ and f is the parameter we fit for, and represents the small adjustments we need to make to the MC energy resolution. The result of this fit is shown in Fig. 4.24.

Using the unperturbed MC, we can calculate the acceptance as the integral above 5.5 MeV. To get the absolute value for the acceptance one should simply compute the number of events above threshold and divide this by the total number of events. The difference between the acceptance obtained from unperturbed MC and the one calculated after changing the two parameters as obtained in the fit in Fig. 4.24 is 0.7% which will be applied as correction to the MC. The last step is to take the fitted

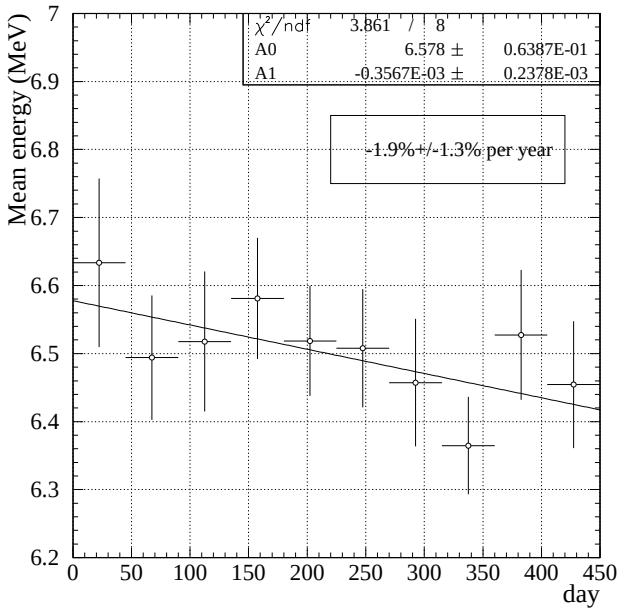

Fig. 4.23: Energy scale stability with muon followers. The drift correction as derived from ^{16}N has already been applied.

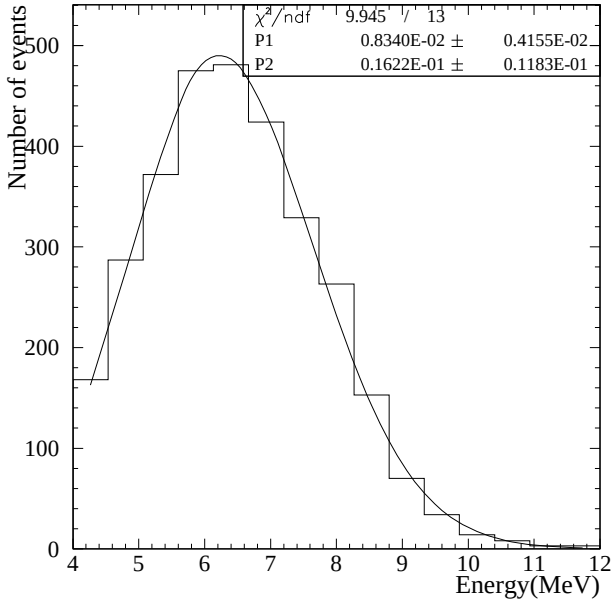

Fig. 4.24: Fit for the energy perturbation function

parameters with uncertainties and the correlation obtained from the fit and draw random numbers, subject to covariances, and integrate above the threshold every time. The resulting distribution of acceptances is shown in Fig. 4.25. A Gaussian fit will tell us the uncertainty on the acceptance: 2.5%. In principle, on top of the statistical errors one should add the uncorrelated systematics as derived above. However, these are very small relative to the statistical uncertainties so the resulting 1-standard deviation of the acceptance changes by a non-significant amount[11].

4.4.5 Neutron capture efficiency

In addition to the energy related part in the NC acceptance we also need to understand the performance for which the model represents the rest of neutron related

[11]The systematic errors are added with no correlation, simply as a random Gaussian shift

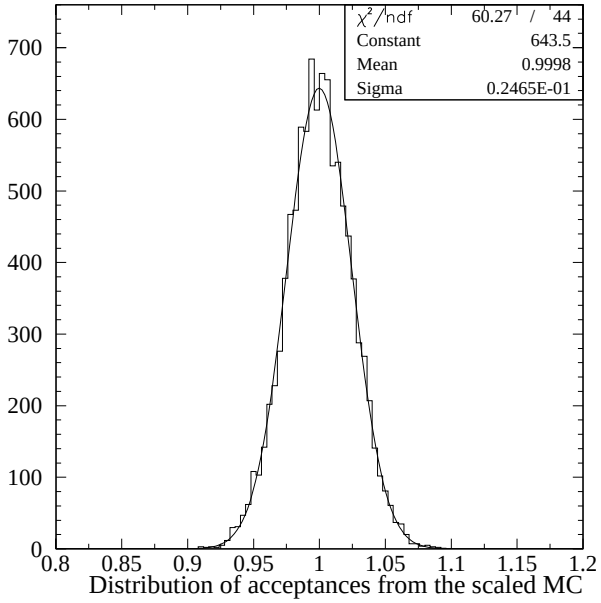

Fig. 4.25: Distribution of NC acceptance.

quantities like neutron capture, integrated cross-section, and neutron transport[12]. For this purpose we can use the ^{252}Cf source and its simulation in MC.

The efficiency is calculated as number of events above the mean energy divided by the total number of events produced by the source (or generated in MC). The calculation is done above the mean energy in order to eliminate effects related to energy scale uncertainty. The mean energy for each source position is determined by a Gaussian fit around the peak of the energy distribution.

Fig. 4.26 shows the measured efficiency at different radial locations. In order to do a sensible comparison between data and MC, we fit the efficiency curve with an empirical function as in [50].

[12]From now on we will call this generally, capture efficiency, which includes all the energy independent quantities related to the neutron capture

$$\epsilon(r) = A(\tanh(B(r-C)) - 1) \tag{4.8}$$

with the three parameters in the fit as A, B and C. The volume weighted efficiency is then:

$$\epsilon = \frac{\int_0^R \epsilon(r) r^2 dr}{\int_0^R r^2 dr} \tag{4.9}$$

with the integration being performed from 0 to R-the 600 cm AV radius. The efficiency determined in this way from the data is 28.28% whereas from MC is 27.13%. The (n,2n) channel is not modelled in MC but it will affect the results obtained from the ^{252}Cf. In [50] it has been estimated that this effect will increase the capture efficiency obtained from the data by 1%. Finally, we can estimate the correction to be applied to MC from all of the above is 1.032. For an energy threshold of 5 MeV and fiducial volume cut of 500 cm we estimate, based on MC and the above correction, a capture efficiency of 39.2%.

The two most important sources of systematic errors that have been investigated were the source positions and the source strength.

- Source strength. The strength of the ^{252}Cf source has been measured as 17.12 ± 0.17 neutrons/sec ([50]). We will assign a 1% uncertainty based on this measurement.

- Source positions. To account for uncertainties in the source position the x,y, and z coordinate of the source were varied in turn by 5 cm. The variation of x or y coordinates has a negligible effect, whereas a variation in z can account for 2.7% uncertainty on the integrated capture efficiency.

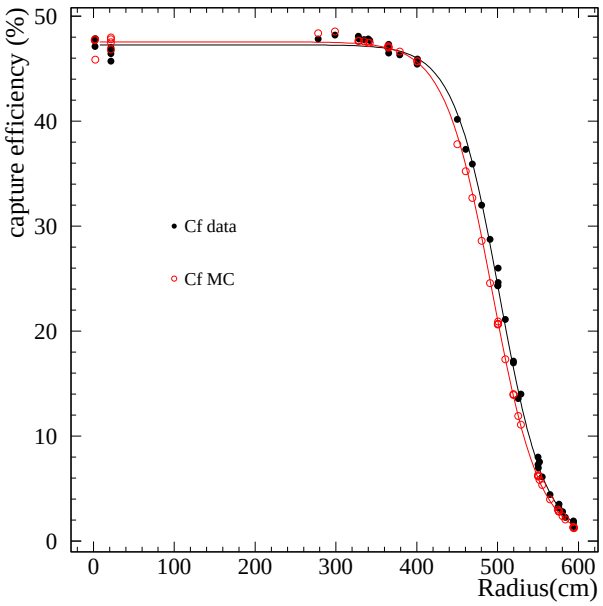

Fig. 4.26: Measured neutron detection efficiency for different ^{252}Cf source positions

Adding these two effects in quadrature we obtain a total uncertainty for the neutron capture efficiency as 2.9%.

4.5 Signal acceptance to Data Cleaning and Post-reconstruction cuts

We need to determine the acceptance of the cuts on the signal and how well this is modeled in MC. Obviously, this quantity will be dependent on the definition of our analysis region. For some of the variables that we use to build PDFs for signal separation, we showed before how the uncertainties are measured. Nevertheless, the signal region is defined also through other cuts like DAMN cuts, $\langle\theta_{ij}\rangle$ and ITR. There is also a contribution from the reconstruction algorithm, in a small number of events

Signal	Acceptance correction	Uncertainty
ES	0.9941	$^{+0.16\%}_{-0.11\%}$
NC	0.9932	$^{+0.16\%}_{-0.11\%}$
CC	0.9941	$^{+0.16\%}_{-0.11\%}$

Table 4.3: Acceptance correction to MC with uncertainties for DC cuts, ITR and $\langle\theta_{ij}\rangle$

which will fail to reconstruct. This measurement has been provided in [51] for each signal in particular and the extracted values are shown in Table 4.3. Due to our loose cuts on $\langle\theta_{ij}\rangle$ and ITR, the signal loss is dominated by the DAMN cuts.

The "sacrifice" (1-acceptance) was calculated for each CC spectral bin and as shown in Fig. 4.27, is consistent with a constant throughout our analysis region.

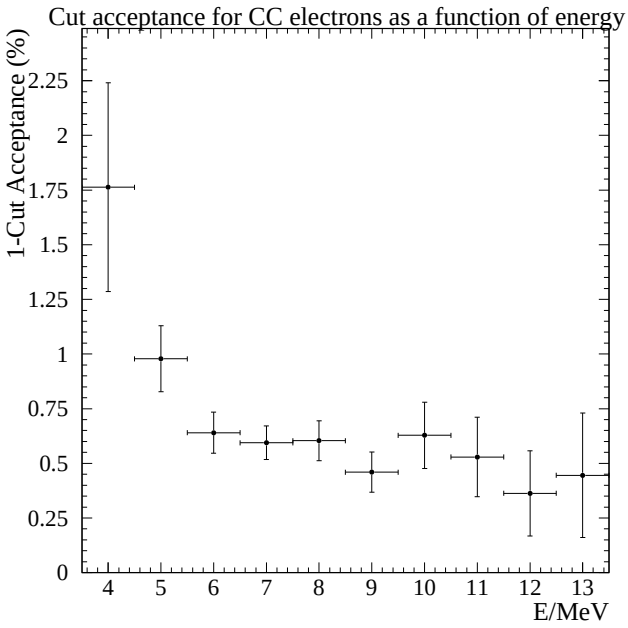

Fig. 4.27: Signal loss for CC events in each spectral bin. The analysis threshold used in this thesis is 5.5 MeV. Figure courtesy of N. McCauley.

Ch. 5

Backgrounds to the Solar Neutrino Measurement

The scientific result from any given experiment is usually sensitive to the precise knowledge of non-signal events present in the data. The SNO result, in particular, depends crucially upon the exact determination of backgrounds. SNO attempts to make an absolute measurement of the electron and non-electron neutrino flux, and the physics interpretation of this measurement will depend non-trivially on both the fluxes. Since the analysis region is defined in a low energy regime, there are a very large number of potential sources of background. The SNO collaboration has developed a large number of cuts designed to reduce or completely eliminate these unwanted events. After the reduction process (Sec. 3.3), complete analyses are developed in order to determine the residual background left in the data set.

There are multiple sources of backgrounds present in the SNO detector. We can distinguish between two major categories:

1. Instrumental backgrounds. These are events that are caused by mis-behaviors

of the detector components. The DAMN cuts and HLC designed to reject these events have been presented in 3.3

2. The Cherenkov backgrounds are $\beta - \gamma$ decays of radioactive isotopes present in the detector.

3. The neutron background events are mostly due to neutrons produced by photo-disintegration of the deuteron by a γ ray from a radioactive decay. In general, though, any process that produces a neutron in the SNO detector should be considered as a potential source of background.

In what follows, we will present the techniques developed to measure the backgrounds present in the data set after all the cuts have been applied.

5.1 Instrumental backgrounds

Although the combined power of the DAMN cuts and HLC (see Sec. 3.3.1) is very high for rejecting all these unwanted events, it is critical to measure the contamination of instrumental background still left in the data set after all those cuts have been applied. For this thesis, we used the "bifurcated" analysis technique (see [52]), to determine the contamination for our clean data set. The results obtained are consistent with zero (0.011 ± 0.007 events), and an upper limit of 3 at 95% confidence level has been established. The author has played a large role in developing this analysis for SNO during the D_2O phase and the same method is used during the current phase. The advantage a bifurcated analysis has in this case is the fact that it relies more on a precise definition of the signals rather than on a precise model of the backgrounds. For SNO, the instrumental events are almost impossible to model with any MC technique.

5.1.1 On the bifurcated analysis

The bifurcated analysis will not be sensitive to any particular background, that the cuts the bifurcated analysis makes use of, are not sensitive to. This says that we can only measure the contamination left over from a background that we know and we can place no bounds on an unknown background. The basic idea behind the analysis, is to measure the efficiency of one cut based on the separation produced by the other cut. Using the two cuts against each other one can estimate the final number of events of each type (signal vs. background) in the "signal region".

The general form of the equations for a bifurcated analysis with n cuts, having acceptances x_i on signal and y_i on background, with n types of background β_i and signal ν, is:

$$R_i = x_i\nu + y_i\beta_i \tag{5.1}$$

$$N = \nu + \sum_i \beta_i \tag{5.2}$$

The starting point in doing any bifurcated analysis is to choose two cuts and apply them to data. The formalism is easier if we assume orthogonality of the cuts, that is to say, there is no correlation between the two. In principle, nothing changes if there is a correlation, since one can always write down (5.1) with a correlation coefficient present. However, measuring that coefficient when multiple cuts are involved can be a daunting task. Assuming one type of background and orthogonality of the cuts, the general equations that will be obtained, for $n = 2$ are :

$$a + c = x_1\nu + y_1\beta \tag{5.3}$$

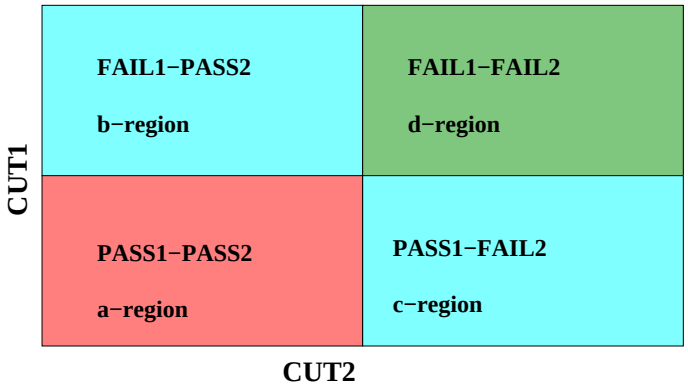

Fig. 5.1: Graphical representation for bifurcated analysis.

$$a + b = x_2\nu + y_2\beta \tag{5.4}$$

$$a = x_1 x_2 \nu + y_1 y_2 \beta \tag{5.5}$$

$$\beta + \nu = S \tag{5.6}$$

where a is the number of events in the pass1-pass2 (events passing both cuts) region, b is the number of events in fail1-pass2 (events failing one cut and passing the other) region, c is in pass1-fail2. A mode of visualizing this is shown in Fig. 5.1.

I will call one of the cuts the "rejection branch" and the other the "normalization branch". The choice of rejection and normalization, is arbitrarily, since the equations are completely symmetric.

The above system of equations can be solved analytically, although one should be very careful in using those equations. First, being a non-linear system of equations, the solutions behave in a very different way in different regions of the solution space. Consequently, before quoting the results one should make sure that the considered region is safe enough, away from any singularity regime that can develop in particular regions[1].

[1]This is simply saying that one should check the stability of the solution to small perturbations

Another assumption that we will use in order to simplify (Eq. (5.1)) is that there is only one type of background, or the relative background sensitivities must be comparable. This is a safe assumption to make, since what we want here is the contamination in a supposedly clean signal (the Cherenkov pattern). One suitable definition for an efficient cut would be " to reject everything that is not Cherenkov -like". To a good extent both DAMN cuts and HLC fall in this category.

The two cuts used for bifurcated analysis have to be orthogonal. This is required for the second term in the right-hand side of equation (Eq. (5.5)) to be correct. This is not a very restrictive requirement, because a correction to the final result can be made. One can easily work assuming orthogonality even if the cuts are not, at least on a small scale, and estimate the systematic uncertainty associated with this eventual violation of orthogonality.

The simplest way to perform this analysis is to assume that acceptances (x_1 and x_2) are 100%, so we can work with the following set of simplified equations, resulting from subtracting the third equation (Eq. (5.6)) from the first two (Eq. (5.4),Eq. (5.5)):

$$c = y_1(1 - y_2)\beta \tag{5.7}$$

$$b = y_2(1 - y_1)\beta \tag{5.8}$$

$$\beta + \nu = S \tag{5.9}$$

This system can be analytically solved. Carrying out the calculation we find the contamination in the **signal box** to be:

$$K = y_1 y_2 \beta \tag{5.10}$$

Orthogonality

As stated above, one major requirement for a bifurcated analysis to give consistent results is orthogonality of the cuts. If there is a correlation between the rejection and the normalization branch the contamination estimates from the bifurcated analysis will turn out to be below the real value for contamination.

In order to reduce the eventual correlation between the DAMN cuts and the high level cuts we perform the so called "mask reduction" procedure. In other words, we extract from the DAMN mask all the cuts that could eventually produce a correlation. By doing this, we diminish the power of the result, but we will be safe from an induced correlation which might affect the obtained number. Thus, the contamination we get from this procedure might not be the actual value, but rather an upper limit.

Out of all the cuts in the DAMN mask, when I perform the mask reduction, I keep only the following cuts:

- AMB
- OWL
- NECK
- QCluster
- Junk

The cuts selected have a very small correlation coefficient as calculated from the covariance matrix and they are sensitive to all types of backgrounds that DAMN cuts and HLC are built for. A more powerful check on the cut correlations consists in the "box relaxation" procedure in which one loosens the cuts in order to detect

any eventual correlation. More than that, by relaxing the box, we can probe the uniformity of our signal and non-signal data. Any eventual background lying very close to the box, but having large tails inside would be picked up by this method.

Before going on with the bifurcation calculation, one should make sure that there are no gross features in the "sanity check" distributions. These distributions are shown in Fig. 5.2 and they mostly reflect the fact that the expected distribution of neutrino reconstructed vertices and direction should be uniform in the detector coordinates in the absence of some biasing effects from detector components.

We are going to use the DAMN cuts as a whole (after the mask reduction) for the normalization branch. For the rejection branch we use the HLC. A graphical description of the entire procedure is shown in Fig. 5.3. The "HLC signal box" is drawn here, and also for the sake of comparison, Cherenkov events from an ^{16}N run have been added.

As was said in the beginning, we will keep only 5 cuts as the DAMN cuts normalization branch in order to reduce the eventual correlation (mask reduction). So, for the bifurcation one has:

- Normalization branch
  - AMB
  - OWL
  - NECK
  - QCluster
  - Junk
- Rejection branch

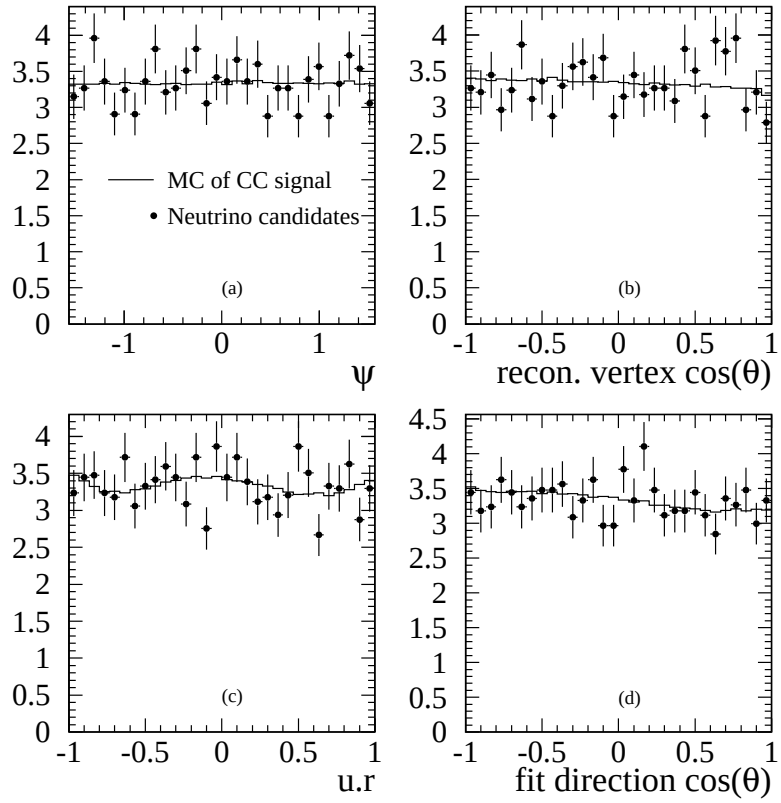

Fig. 5.2: (a)The ψ polar angle of the reconstructed vertex for selected neutrino candidates. (b)The $\cos\theta$ polar angle of the reconstructed vertex. (c)Angle between the reconstructed direction vector and the vector that connects the center of the detector with the reconstructed position. (d) The $\cos\theta$ of the fit direction

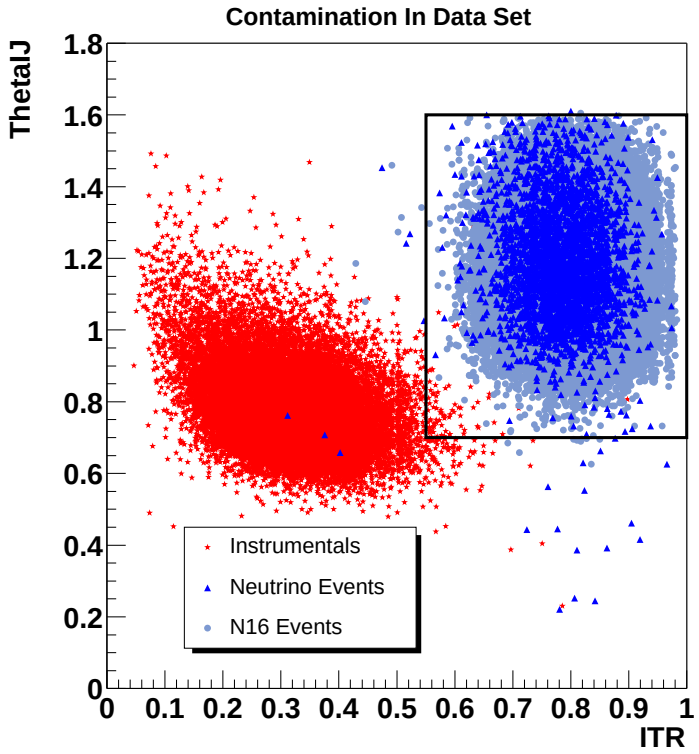

Fig. 5.3: Signal box as defined by HLC. The ^{16}N events are also shown. The events labeled as "Instrumentals" are cut by the DAMN cuts. Figure courtesy of M. Dunford

– ITR

– $\langle\theta_{ij}\rangle$

Using the cuts from above and the algorithm described, one can determine an upper limit for the number of instrumental events present in the data after all the cuts were applied . At 95% confidence level, we obtain $k = 3$ events from contamination.

Box relaxation

The first check that has to be done when dealing with the bifurcated analysis is to try to estimate the result after the box relaxation procedure. The nature of our two branches makes it hard to relax the DAMN cuts side. However, we can easily relax the rejection branch. This procedure has been used during the D_2O phase to check whether the cuts are orthogonal. To get a statistically significant result we will perform this analysis in a low energy regime and extended fiducial volume by considering all the events in the data set with a total number of hits greater than 40 and reconstructing inside 600 cm. The amount of relaxation imposed is shown in Fig. 5.4 (new box: ITR$>$ 0.5 and $0.65 < \Theta_{ij} < 1.5$).

The total number of events we count in the relaxation region, showed in 5.4, is 22. If we perform the bifurcated analysis on the relaxed box, we get $K = 29 \pm 1$ events total contamination with the relaxed cuts. Besides the 22 events in the relaxation region, one should add up the 2 events contamination obtained in the regular box, for Nhit$>$ 40 and Rfit$<$ 600, for a total of 27.5 ± 0.5. The result is in almost prefect agreement with the $K = 29 \pm 1$ number from above. This shows two things. One, there is no hidden correlation between DAMN cuts and HLC. Second, there is no strong sensitivity of the contamination result to the box size.

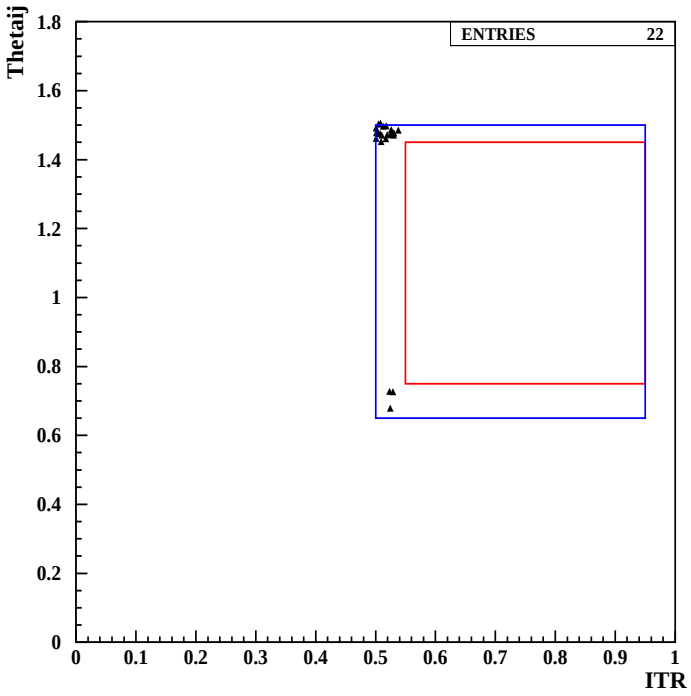

Fig. 5.4: An example of the box relaxation procedure. As stated in text, this has been perform on analysis region defined by (Nhit$>$ 40 and Rfit$<$ 600). The inner box is the usual HLC box used for analysis whereas the outer box is the "relaxed" box described in text. The astute reader will realize that the distribution of events in the relaxation region is not identical to what would be obtain from Fig. 5.3. The reason for this is the lower threshold and extended fiducial volume

5.2 Backgrounds from radioactivity

The SNO trigger rate is dominated primarily by events from radioactivity, in particular the radioactive decays in the ^{238}U and ^{232}Th chains. Avoiding this background ultimately dictates the energy threshold of the SNO solar neutrino analysis. Understanding these backgrounds and a precise measurement of any tails inside the analysis window are prerequisites for the solar neutrino measurements.

It is natural to distinguish between two categories: photo-disintegration neutron background and Cherenkov background. The former is produced by the highest energy γ 's in the decay chains (2.6 MeV and 2.4 MeV for ^{232}Th and ^{238}U respectively) which can break up a deuteron to release a neutron. The ^{232}Th and ^{238}U decay chains are shown in 5.5 and 5.6. Although the fraction of ^{208}Tl γ 's that will proceed via a $\gamma d \longrightarrow pn$ interaction is of the order of 1/500 of γ 's that undergo the usual Compton scattering interaction[2] , these can mimic the neutrons from the NC interactions and pose a serious problem to the NC measurement. The second class of low energy backgrounds, the Cherenkov backgrounds, are simply $\beta - \gamma$ decays, which occur below the analysis energy threshold or outside the fiducial volume, but appear inside the signal region due to finite resolution (both in reconstruction and energy) of the detector. Within each category, we will further discriminate between internal backgrounds, events occurring due to the heavy water radioactivity, and external backgrounds, those coming from the AV, H_2O and PSUP.

In the following, each one of the four classes of background will be described in detail. In particular, for each class we need to determine two things. One, the total number of background events leaking into our analysis window and two, the shape in

[2]This ratio is much smaller for ^{214}Bi , as shown later in text

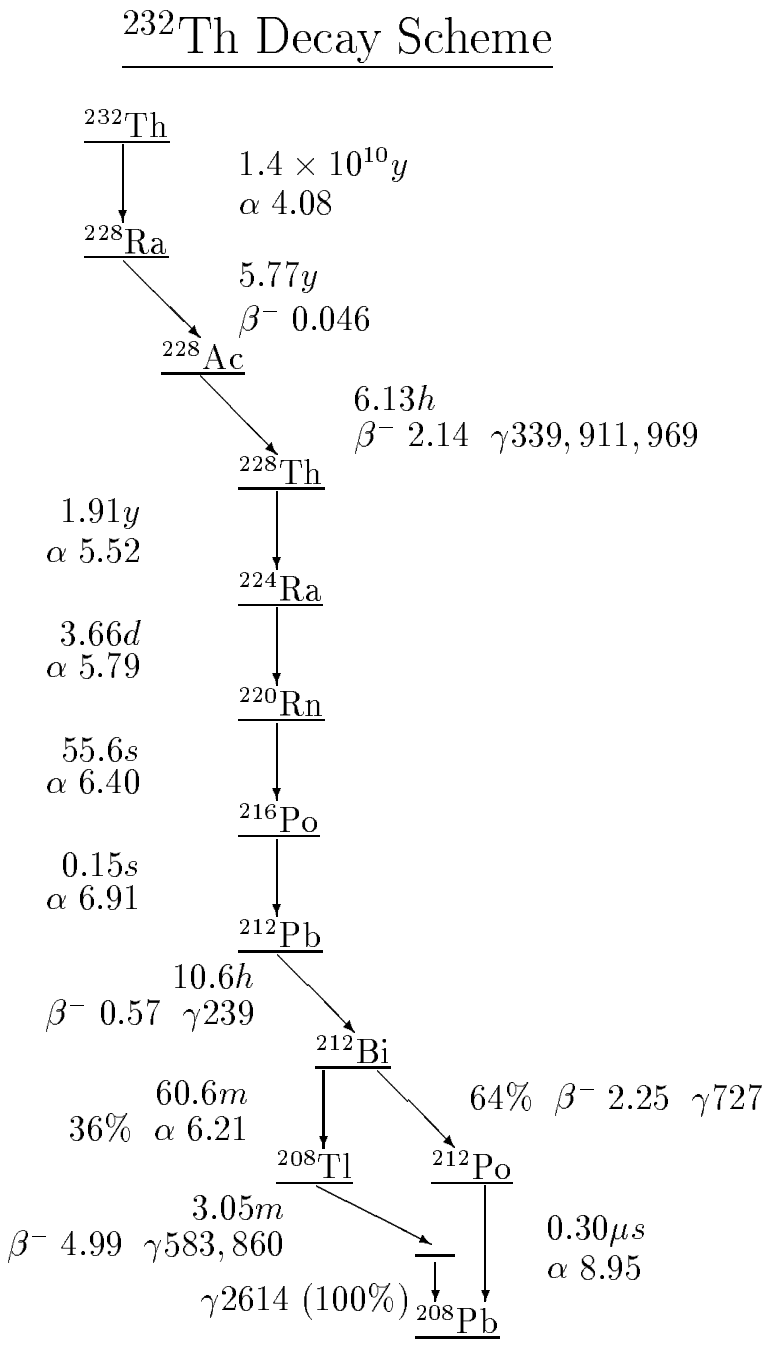

Fig. 5.5: The ^{232}Th decay chain. Taken from [53].

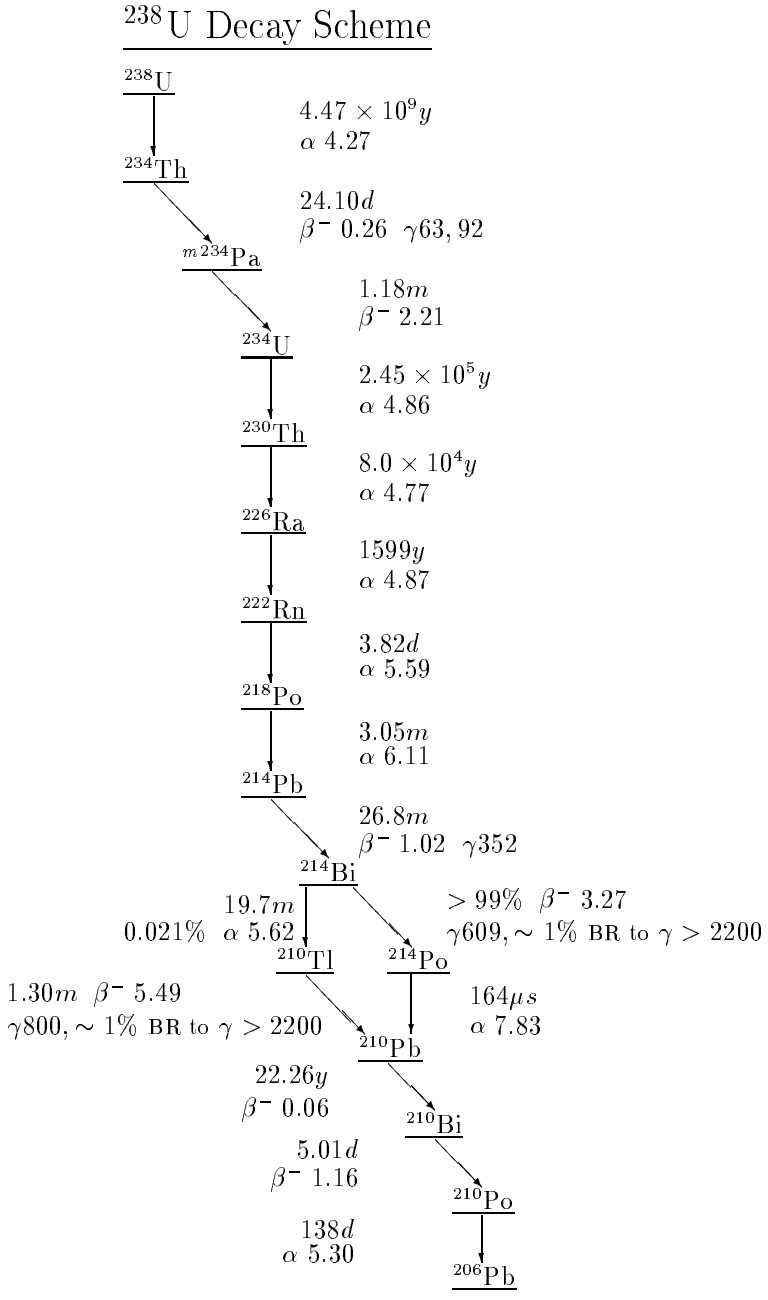

Fig. 5.6: The ^{238}U decay chain. Taken from [53].

each variable used in the algorithm for extracting the SNO signals. The latter is a subtle problem, since one needs to understand the signal from which each background should be subtracted and with the large covariances present this is not trivial. On the other hand, one hopes that these backgrounds are not large, so even non-negligible uncertainties on these shapes would be present in as a second order effect only in the final signal.

5.2.1 The internal photo-disintegration background

In order for SNO to be able to produce a significant NC neutrino flux measurement, the level of ^{232}Th concentration in D_2O has to be below a target level of 3.7×10^{-15} and ^{238}U below 4.5×10^{-14}. This levels would produce $\sim$1 n/day which will translate into $\sim$ 10% of the SSM flux prediction.

The SNO experiment employs two techniques to determine the number of neutrons coming from photo-disintegration of deuterons by γ 's from ^{238}U and ^{232}Th chains. First (*ex-situ*), radiochemical assays are done on a monthly basis to determine the ^{238}U and ^{232}Th equivalent content of the heavy water. The three methods used to determine these concentrations are:

- Extraction of Ra using MnOx beads
- Extraction of Ra, Th and Pb isotopes using HTiO membranes
- "Degassing" of ^{222}Rn from the ^{238}U chain. There are two reasons for this; one, the ^{222}Rn will be removed from the water and two, removal of the oxygen reduces the biologic contamination of the water.

When the ^{238}U and ^{232}Th equivalent concentrations are known, one can then use

MC, or even analytic calculations to calculate how many neutrons will be produced through photo-disintegration. More precisely, the high energy γ 's come from the ^{214}Bi and ^{208}Tl, which are radioactive daughters of ^{238}U and ^{232}Th , respectively. They are really what we are interested in from the photo-disintegration standpoint. To translate ^{232}Th and ^{238}U concentrations to ^{208}Tl and ^{214}Bi one has to assume secular equilibrium.

"In-situ" determination of ^{208}Tl and ^{214}Bi and the number of photo-disintegration neutrons in the signal region

A second technique (*in-situ*), with mostly different systematics, relies on the fact that ^{232}Th chain daughter, ^{208}Tl , has multiple γ 's, whereas ^{214}Bi , from ^{238}U , above any reasonable energy threshold we can consider, has one γ together with a single β with 3.27 MeV high-point. A ^{208}Tl decay appears more isotropic than the ^{214}Bi decay, so one could use an isotropy parameter to distinguish on a statistical basis between ^{214}Bi and ^{208}Tl decays.

Fig. 5.7 shows the $\langle\theta_{ij}\rangle$ distributions for ^{214}Bi and ^{208}Tl decays in a $4.5 - 5$ MeV energy window. This can be used to measure the number of γ 's capable of photo-disintegrating the deuteron and implicitly, the number of background neutrons to the NC signal.

The method simply extracts the number of ^{208}Tl and ^{214}Bi decays using a maximum likelihood fit on the $\langle\theta_{ij}\rangle$ distributions in a low energy (4.5-5 MeV) regime. Having done this separation, one can then uses MC calculations to determine how many ^{214}Bi and ^{208}Tl decays took place. The technique has been described in detail in [53]. For the salt phase analysis the concentration levels of ^{232}Th and ^{238}U inferred from *in-situ* and *ex-situ* are presented in Table 5.1.

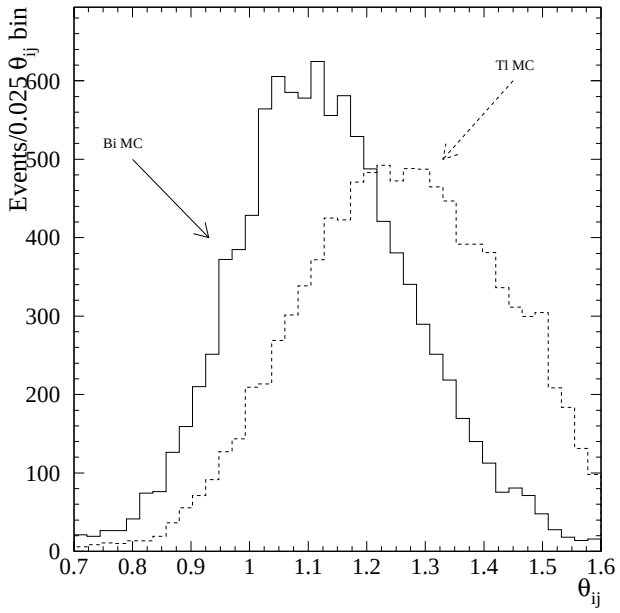

Fig. 5.7: $\langle\theta_{ij}\rangle$ distributions as obtained from ^{214}Bi and ^{208}Tl MC decays in a 4.5-5 MeV energy window.

	^{232}Th ($\times 10^{-15}$ g Th/g D_2O)	^{238}U ($\times 10^{-15}$ g U/g
in-situ	$1.20 \pm 0.57(\text{stat})^{+0.80}_{-0.96}(\text{sys.})$	$8.67 \pm 1.06(\text{stat})^{+2.4}_{-1.97}(\text{sys.})$
ex-situ	$2.82 \pm 0.56(\text{stat})^{+0.83}_{-1.50}(\text{sys.})$	-
Recommended	1.64 ± 0.84	$8.67^{+2.62}_{-2.24}$

Table 5.1: ^{208}Tl and ^{214}Bi levels in D_2O according to [54]. The recommended concentrations for ^{232}Th has been calculated as the weighted average of the two measurements

Based on SNOMAN calculations, the average number of decays needed to produce a neutron are 477.7 for ^{208}Tl and 32087 for ^{214}Bi (according to [54]). Assuming the radioactive chain to be in equilibrium we can write:

$$N_p R_p = N_d R_d \tag{5.11}$$

where N_i represents the number of nuclei of type i ($i = p, d$, parent or daughter) and R_i, the decay rate which can be related to the half-live as $R = \ln 2 / T_{1/2}$. For example, in the ^{208}Tl case, for a branching ratio for the ^{232}Th to ^{208}Tl channel of 0.36:

$$\frac{6.023 \times 10^{23}}{232} \times \frac{\ln 2}{1.405 \times 10^{10}\text{yrs}} = 1455.8 \quad {}^{208}\text{Tl} \quad \text{decays/s/g} {}^{232}\text{Th} \tag{5.12}$$

For ^{214}Bi , the branching ratio is 0.99979 and the above calculation gives 12441 ^{214}Bi decays/s/g ^{238}U . Combining all the previous numbers, one can determine the *produced* number of neutrons per second in the data set from ^{232}Th and ^{238}U :

$$n = C \times M_{D_2O} \times R \times N_n \tag{5.13}$$

where C is the concentration, M_{D_2O} is the D_2O mass (1000 tones), R is the number of daughter decays per gram of parent per second and N_n is the average number of decays needed to produce a neutron. For ^{232}Th we obtain 0.43 ± 0.22 neutrons/day, while for ^{238}U , $0.291^{+0.088}_{-0.075}$ neutrons/day. To go from here to neutron backgrounds in the data set we multiply the number of produced neutrons with the neutron capture efficiency for our signal box.

As far as shapes are concerned, the photo-disintegration neutron background is

trivial. The events are neutrons, with the same distribution as the NC neutrons, so they can get subtracted in a straightforward way from the NC result.

5.2.2 Internal Cherenkov backgrounds

Internal Cherenkov backgrounds, as mentioned above, are defined as low energy $\beta - \gamma$ events, originating in D_2O, that reconstruct inside our signal region due to finite detector resolution. The calculation of these backgrounds relies on the measurement of the number of photo-disintegration neutrons. Since both come from the same source (^{238}U and ^{232}Th decay chains), one is able to determine the number of Cherenkov events above threshold as a constant fraction of the number of detected photo-disintegration neutrons above the same threshold. Obviously, these fractions will not be the same for different decays since the energy distributions will be different. We present in Fig. 5.8 and Fig. 5.9 the energy distributions for ^{214}Bi and ^{208}Tl as obtained from MC.

To account for any systematic effects, we randomly pick uncorrelated values from the $\pm 1\sigma$ interval for the defining variables. The defining variables are all the parameters that determine our signal box. In the end we can recalculate the Cherenkov -to-neutrons ratio with these new values for the defining variables. The spread obtained represents the band of systematic uncertainties.

There are nevertheless some problems inherent to the method. The MC has implicit assumptions, like the uniform distribution of radioactivity inside the fiducial volume. The analysis assumes that the uncertainties derived at higher energies (^{16}N) applies also at the low energies, specific for the $\beta - \gamma$ decays. To check all these assumptions, and also to find a way to lower the uncertainties, a "perfect" source was

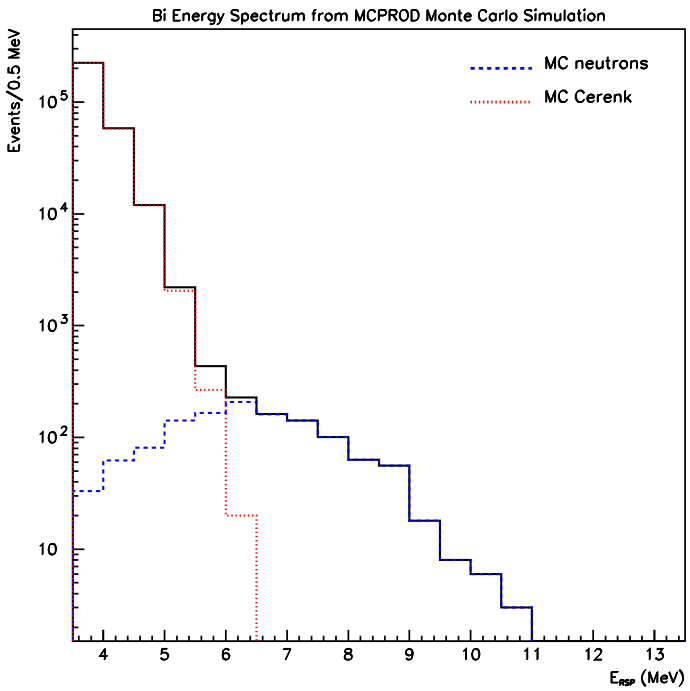

Fig. 5.8: Energy distribution for ^{214}Bi MC with the Cherenkov and neutron components. Figure courtesy of J. Klein

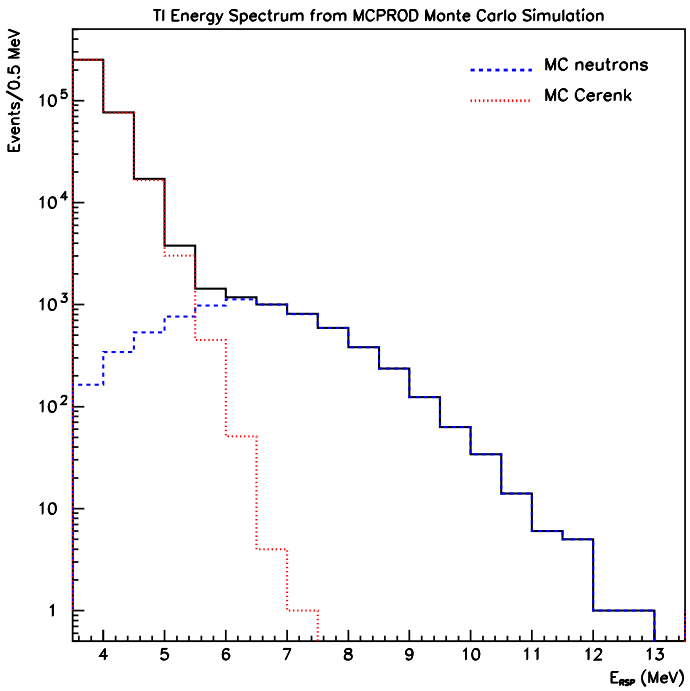

Fig. 5.9: Energy distribution for ^{208}Tl MC with the Cherenkov and neutron components. Figure courtesy of J. Klein

deployed in the D_2O volume. This was a controlled ($\sim 80\,Bq$) ^{222}Rn spike injected into the heavy water. The strength of the spike was estimated to be over a thousand times larger than the expected level of ^{222}Rn activity in the D_2O. The injection was done by inserting known quantities of radon-enriched D_2O at several locations within the detector. The spike analysis uses 212 h of high radioactivity data after the injection and subtracts 304 h of "quiet" neutrino data which was taken right before the injection, to ensure stability of the result against any long time variations in the detector. The "quiet" data is subtracted in a livetime normalized way, for any distributions of interest that would be obtained from the ^{222}Rn spike. This ensures that the resulting distributions represent only the introduced ^{222}Rn components in the detector.

The spike provides useful checks on the MC. The comparison of the energy distributions is shown in Fig. 5.10. In order to find a meaningful way to asses systematics one can fit the data (spike) with the model (MC), allowing a small number of parameters to vary (the height of the Cherenkov background, the height of the neutron peak, the energy scale and the energy resolution). Indirectly, this also provides a check on the estimated energy scale and resolution from other sources (^{16}N, ^{8}Li). Fig. 5.11 shows the best fit together with the Cherenkov and neutron components. To find the Cherenkov-to-neutrons ratio one just has to integrate the two curves above the threshold. For our 5.0 MeV total energy threshold the obtained Cherenkov -to-neutrons ratio turns out to be $0.48^{+0.10}_{-0.06}$.

The ratio determined before is valid just for ^{214}Bi , since ^{222}Rn is part of the ^{238}U chain upstream from ^{214}Bi . To get a similar number for ^{208}Tl we would have to use a ^{224}Ra spike, which is yet to be deployed. Therefore, for ^{208}Tl one has to use the MC as described above. The obtained Cherenkov -to-neutrons ratio for

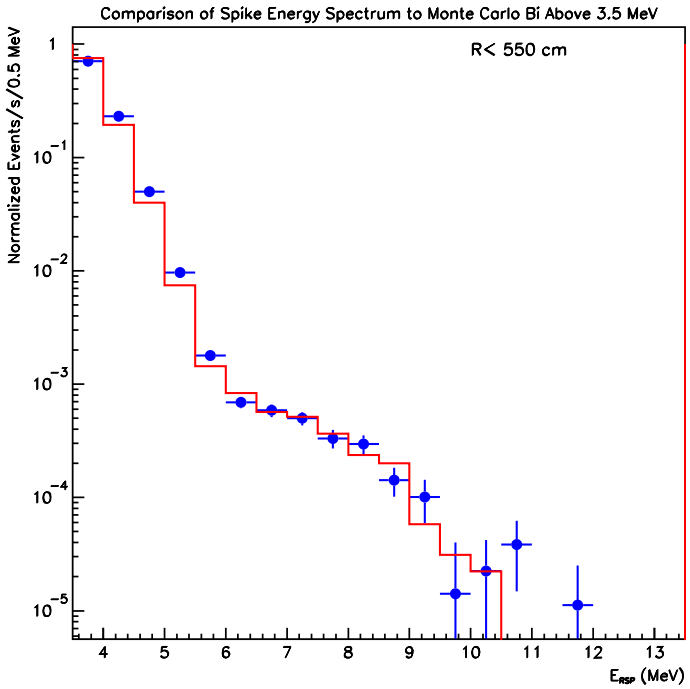

Fig. 5.10: Comparison between ^{214}Bi MC and the Rn spike energy distributions. Figure courtesy of J. Klein

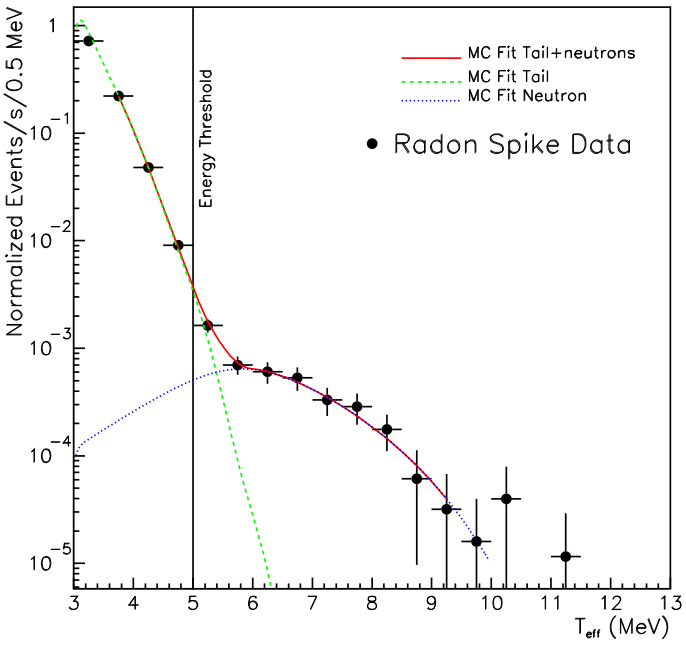

Fig. 5.11: Fit on the spike data using the ^{214}Bi MC. There are four parameters allowed to vary: the height of the Cherenkov wall, the height of the neutron peak, the energy scale and the energy resolution. Figure courtesy of J. Klein

^{208}Tl is $0.080^{+0.035}_{-0.015}$. The ^{214}Bi Cherenkov -to-neutrons ratio has also been computed as $0.33^{+0.13}_{-0.08}$ for comparison with the one obtained from the spike. As shown below, we expect a number of neutrons from ^{24}Na activation. This decay will also produce $\beta - \gamma$ events. The calculated ratio is $0.51^{+0.17}_{-0.08}$. The details on this analysis are presented in [55].

5.2.3 External Cherenkov backgrounds

The analysis for the Cherenkov backgrounds from the AV, H_2O and PMTs is relatively similar to the *in-situ* for the internal backgrounds. Instead of using an asymmetry parameter one can use the different characteristic radial profiles given by the three

regions of interest[3]. Unfortunately, the MC modeling of the detector grossly breaks down as one passes the AV boundary. Since we cannot use MC, we have to produce a simulation of the radioactivity in the three regions by using calibration sources. A perfect choice is the acrylic encapsulated Th sources [56] which have been deployed throughout the outer regions in both D_2O and salt phases. For the H_2O region, one has to rely on a volume weighting algorithm to compensate for the point sources used. This method has been developed during the D_2O phase by the author and is currently used for the current phase too.

Close to the end of the salt data taking, right after the D_2O ^{222}Rn spike, the SNO collaboration decided to deploy an H_2O Rn spike. This solved two problems: one, there was no need for a volume weighting and two, ^{222}Rn is part of the ^{238}U chain, therefore provided the needed cross check to the ^{232}Th chain only events produced by the sources.

The total integrated lifetime from the two Rn injections into the H_2O we use is 4.92 days. H_2O circulation was stopped after 3 hours in the second injection provided in this way a somewhat different radial distribution between spikes which can also help from assessing systematics from recirculation.

The AV PDF is built using encapsulated Th runs at 595 cm radius. The major problem for building this PDF is the high contamination in the Cherenkov region from neutrons, since the 2.614 MeV γ ray resulting from ^{208}Tl can photo-disintegrate the deuteron. This can be easily seen in Fig. 5.12. In order to subtract the neutrons from the source we generate Monte-Carlo with the specific conditions of the runs taken. As shown in Fig. 5.13, above 6.5 MeV the vast majority of events from the source are neutrons, so we can define a "Cherenkov free" region above some relatively

[3]AV, H_2O , PSUP

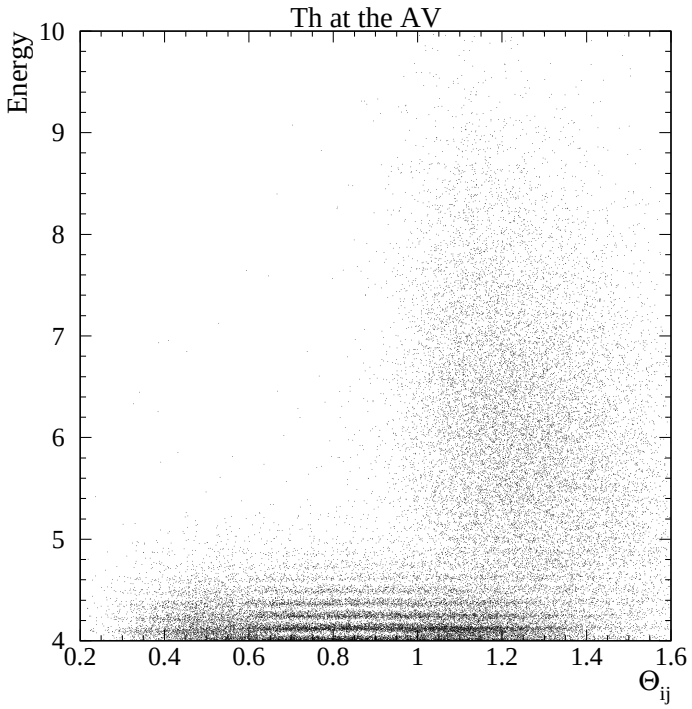

Fig. 5.12: Run 25773 encapsulated Th at 595 cm. There are clearly two populations in this plot. The neutron region is defined by a relatively high energy and large values for θ_{ij} whereas the $\beta - \gamma$ region lies more towards low energies and smaller θ_{ij}. The astute reader will realize that the $\langle\theta_{ij}\rangle$ distribution in this figure is different than then $\langle\theta_{ij}\rangle$ distribution in 5.7. This is a geometry effect which will decrease $\langle\theta_{ij}\rangle$ as one approaches the AV.

high energy threshold, normalize to the total number of events in this region and extrapolate the number, the radial and the energy shape of the neutrons at any energy based on MC.

The PMT PDF is the simplest construction of the three. It uses a very intense ("superhot") encapsulated Th source deployed near the PSUP. The "neutrino subtraction" is done in the same way as for the AV and H_2O PDFs. The runs used have a total integrated run time of 41.66 hours. The obtained radial PDF is shown in Fig. 5.14.

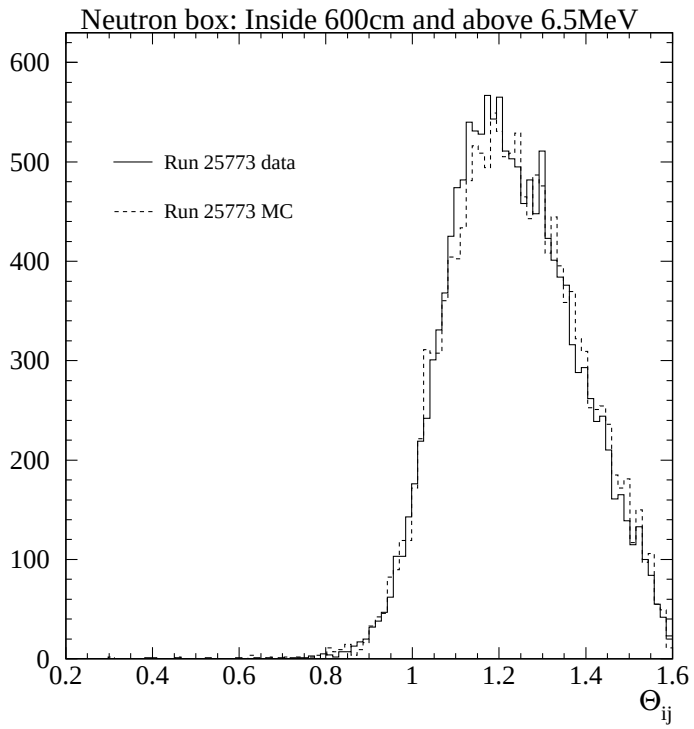

Fig. 5.13: θ_{ij} comparison between data and MC for acrylic source neutrons

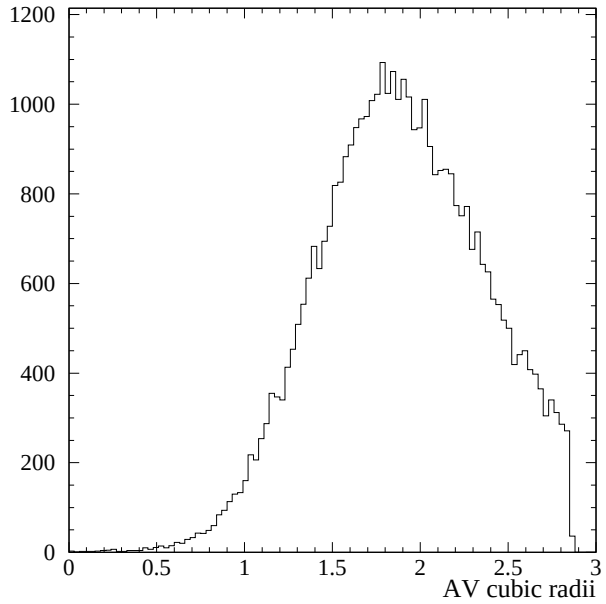

Fig. 5.14: The radial PDF derived from the superhot Th run above an energy threshold of $T_{eff} > 4.5\,\mathrm{MeV}$.

The radial fit

In order to determine the tail of low energy backgrounds into the neutrino signal region, we fit the radial distribution of events in the neutrino data sample in the light water to a linear combination of the three radial PDFs. The fit is done by performing an Extended Maximum Likelihood method with binned data and PDFs (a description of the generalized maximum likelihood method will be given in Sec. 6.1) . In order to minimize the effect of neutrino events or heavy water backgrounds we restrict the fit between 1.1 and 2.5 cubic AV radii and consider 43 bins for both data and PDFs.

Systematic uncertainties for the radial fit in the light water

In what follows we present the largest systematics that can affect the measurement of the Cherenkov light water contribution inside the fiducial volume.

- $z-$asymmetry The Rn spike was deployed only at the bottom of the detector. To investigate the z-asymmetry we use the Th encapsulated source. We can define the radial response to the Th Cherenkov events as the number of events that reconstruct above 5.0 MeV and inside fiducial volume to the total number of events above 5.0 MeV from the acrylic sources. Fig. 5.15 shows this response for the two hemispheres. We can fit exponentials as a model for this response function and take the fractional difference in normalizations of the two as the uncertainty related to the z-asymmetry. That comes out to be 3%.

- Time variations

  Since we do not have a consistent measurement of the time variations (both in reconstruction and energy response) in the light water we will use the neutrino

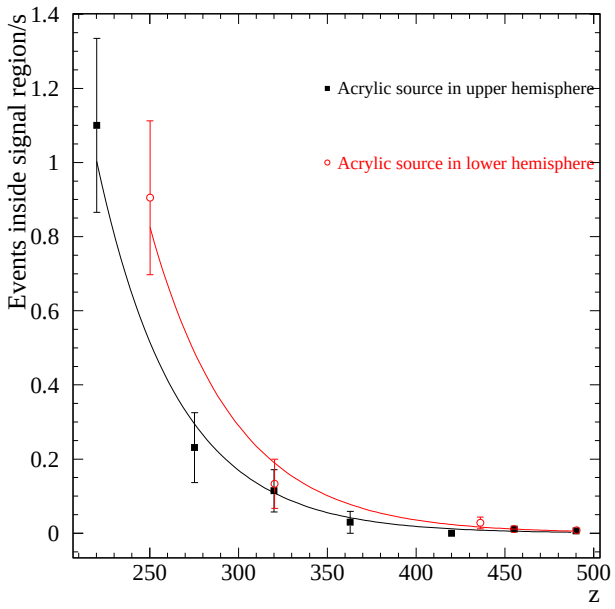

Fig. 5.15: The $z-$asymmetry based on ^{232}Th sources

data itself to tell us about possible time dependencies. Of course this has the unavoidable caveat that there are a lot of effects we are looking at here besides changes in reconstruction/energy, like unintended radioactivity spikes in the light water from power failures. Fig. 5.16 shows the ratio of events reconstructed inside the fiducial volume and between 3.5 and 4 MeV with $u{\cdot}r > 0.75$ and events reconstructed between 650 and 750 in the same energy range and $u \cdot r > 0.5$. A value of $u \cdot r > 0$ corresponds to events going outward whereas a negative value, to events going inwards. The uncertainty in the average reconstruction ratio is 3%.

The same procedure can be used to identify the stability of the PMT reconstruction ratio using as the normalization the region between 720 and 850 with $u \cdot r < -0.5$. For this, we assign a conservative 10% uncertainty.

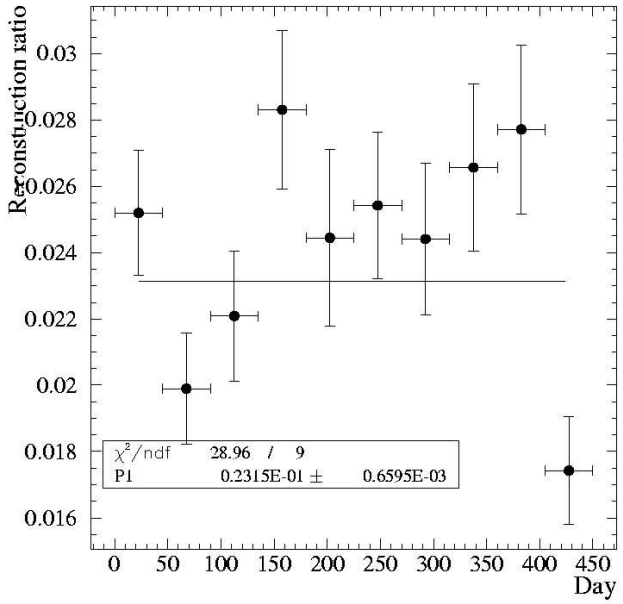

Fig. 5.16: Time variations on light water reconstruction.

- U and Th differences

  For PMT $\beta - \gamma$ we will assume there is no difference between Bi and Tl. This should be the case since, close to the PSUP, the reconstruction and energy resolutions should completely wash out any potential differences.

  For the H_2O $\beta - \gamma$'s we have the encapsulated ^{232}Th sources and we can simply repeat the fitting procedure using the H_2O PDF as constructed in Ch. A. The fit is shown in Fig. 5.17 and the difference in estimated H_2O backgrounds between the source technique and the ^{222}Rn spike technique is 57%. This is in good agreement with the estimated U/Th difference ($\sim$ 60%) based on MC presented in [57].

  The AV PDF was determined using the encapsulated Th source. We also have

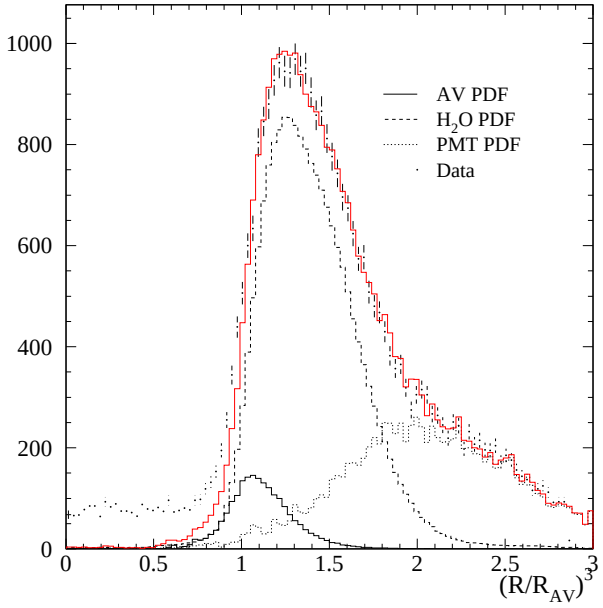

Fig. 5.17: 4.5 MeV fit with the acrylic sources used to build the H_2O PDF

U sources deployed at roughly the same radius. We can substitute the U source for the Th source and repeat the analysis. The estimated backgrounds from the AV change by 8%.

- Neutron energy scale and resolution for the AV PDF subtraction

  Although this analysis is specifically designed not to rely on the MC calculations, one place this becomes unavoidable is for the AV PDF. As mentioned above, in order to obtain the Cherenkov tail backgrounds from the AV we need to subtract the photo-disintegration neutrons, and the only way we can currently do this is using MC.[4] This becomes especially hard in salt, where the capture efficiency does not drop rapidly when close to the AV, and as it can be seen in Fig. 5.18 the neutrons completely dominate above ~ 6 MeV. This is actually

[4]It would make a great improvement if we would have the Cf source deployed at the AV

one of the reasons the fit is done at 5 MeV, since obviously one has no chance of extracting in a statistically significant way the Cherenkov events from the neutron events. Given this, one would expect a huge statistical uncertainty on the AV background. However, since we took much more data than the integrated activity on the AV, the scaling factor is very small ($\sim 1\%$) so one can accept large uncertainties. However, the exact reproduction of the energy scale and resolution of the neutrons near the AV is still crucial for extracting the AV background. In an attempt to determine the scale and resolution we fit a Gaussian on data and MC from 5.7 MeV to 9 MeV in energy. The difference in mean between data and MC is 0.4% and 3% in resolution. Gaussian convolution of MC using these numbers changes the extracted AV background by 18% due to energy scale and 25% due to energy resolution.

- Pile-up from the source

  We use MC to determine the level to which pile-up from the source affects the analysis, since the rate of 5000 Hz could in principle pose a serious problem to the analysis. Considering the 400 ns trigger window and the 5 kHz rate, we can infer the coincidence rate to be $R = r \times r \times \tau = 1$ Hz. Generating MC for the run closest to the AV (24187) at 10 Hz coincident 2.6 MeV γ 's from the source position the number of events reconstructing inside 550 and above 5.0 MeV was determined to be 4 events. Since the actual rate of coincidences is 1 Hz, the contribution of pile-up to the first run is 0.4 events. Compared to the actual number of events from the source passing the analysis cuts this is negligible, so the pile-up will be ignored.

- Volume distribution of radioactivity This is the most difficult systematic to

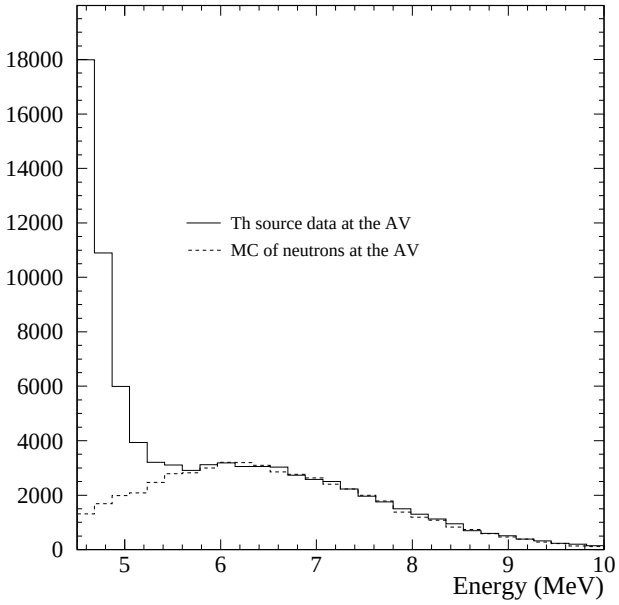

Fig. 5.18: Energy profile of events reconstructed inside 550 from the Th source deployed at the AV

evaluate. In principle, aside from z-asymmetries there are subtle effects due to the fact that the Rn spike distribution and the superhot source do not have exactly the same volume distribution as the real radioactivity in the outer detector regions. A powerful test on how well we model this with sources and the spike is obviously the fit itself, since there is no gross mismatch between the data and our fitted radial profile.

There are multiple ways one should change these radial distribution to account for all possible variations in the radial profiles. It is both hard to be sure that all the variations have been accounted for and this is also technically difficult. Instead, we take a more practical approach and assume a 2% radial shift to be applied to H_2O PDF and PMT PDF. This, although likely to be an overestimate, will change the H_2O backgrounds by 40% and the PMT backgrounds by 47%.

ML fit on the neutrino data set

We performed the described analysis on the neutrino data set. The actual fit is done from 1.1 to 2.5 AV cubic radii, which roughly corresponds to 620 to 811 cm. Aside from the energy threshold specified we also apply a high energy cut at 8 MeV, in order to reject any pathological events from the source. Table 5.2 shows the extracted number of events at different analysis thresholds and fiducial volumes.

As mentioned above, at higher thresholds this analysis breaks down since we have other types of events that are not negligible anymore. Therefore, in order to obtain a meaningful number we will repeat the procedure used for D_2O phase and scale to higher energies the number of background events inside the neutrino signal region based on the fitted amplitudes at 4.5 MeV which are for AV, H_2O and PMT

Fiducial cut(cm)	Threshold(MeV)	AV	H_2O	PMT
550	4.5	44 ± 10	86 ± 11	47 ± 10
	5.0	4 ± 5	9 ± 6	16 ± 12
	5.5	0 ± 5	-3 ± 5	14 ± 12
500	4.5	12 ± 3	13 ± 7	5 ± 7
	5.0	0 ± 3	-4 ± 5	-3 ± 9

Table 5.2: Extracted number of background events for several analysis thresholds. Errors are statistical only.

Fiducial cut(cm)	Threshold(MeV)	AV	H_2O	PMT
550	4.5	1760 ± 425	104 ± 13	38 ± 8
	5.0	184 ± 205	12 ± 9	8 ± 6
	5.5	-8 ± 183	-4 ± 4	5 ± 4
500	4.5	494 ± 115	15 ± 9	4 ± 5
	5.0	20 ± 106	4 ± 6	1 ± 4

Table 5.3: Number of events from the external Cherenkov backgrounds PDFs that reconstruct in the signal region

respectively 0.025, 0.824 and 1.228. Table 5.3 shows the number of events in the signal region at the 3 analysis thresholds.

Using the numbers from Table 5.3 and the scales at 4.5 MeV, one can derive the number of background events in our signal region. The results for 5.0 and 6 MeV are shown in Table 5.4.

This measurement is completely dominated by statistical uncertainties particularly at high energy threshold. Table 5.5 presents the largest systematic uncertainties

Fiducial cut(cm)	Threshold(MeV)	AV	H_2O	PMT
550	5.0	3 ± 5	10 ± 7	13 ± 7
	5.5	0 ± 4	-3 ± 4	6 ± 5
500	5.0	0.5 ± 2	3 ± 5	1 ± 5

Table 5.4: Scaled number of external Cherenkov background events

Systematic type	AV(%)	H_2O (%)	PMT(%)
z-asymmetry	3	3	3
Radial profile	-	40	47
Neutron subtr.	31	-	-
Stability	3	3	10
U/Th	8	57	-
Total	32	69	48

Table 5.5: Table of systematics for the external Cherenkov background analysis

that were found above.

One can add the statistical and systematic uncertainties together, for each PDF and superimpose the final fit on the neutrino radial distribution. That is shown in Fig. 5.19 where the width of the bands represents the size of combined statistical and systematic uncertainties on the resulting fit.

The shape measurement for the external Cherenkov background is very hard due to the limited statistics we have. However, above an energy threshold of 5.0 MeV and inside 500 cm the total number of event we determine in Table 5.4 is 4 with an uncertainty of 7. To obtain shapes for these events could be technically challenging, but since the number is relatively small, we will take a more practical approach and assign an additional uncertainty of 11 events to CC and NC signals.

5.3 External neutron backgrounds

Similar to the photo-disintegration neutrons produced by ^{238}U and ^{232}Th decays in D_2O there is a contribution from ^{238}U and ^{232}Th decays in H_2O , AV or other outer region of the detector. Also, one expects neutrons from (α, n) reactions on ^{2}H, ^{17}O and ^{13}C which are abundant throughout the acrylic vessel.

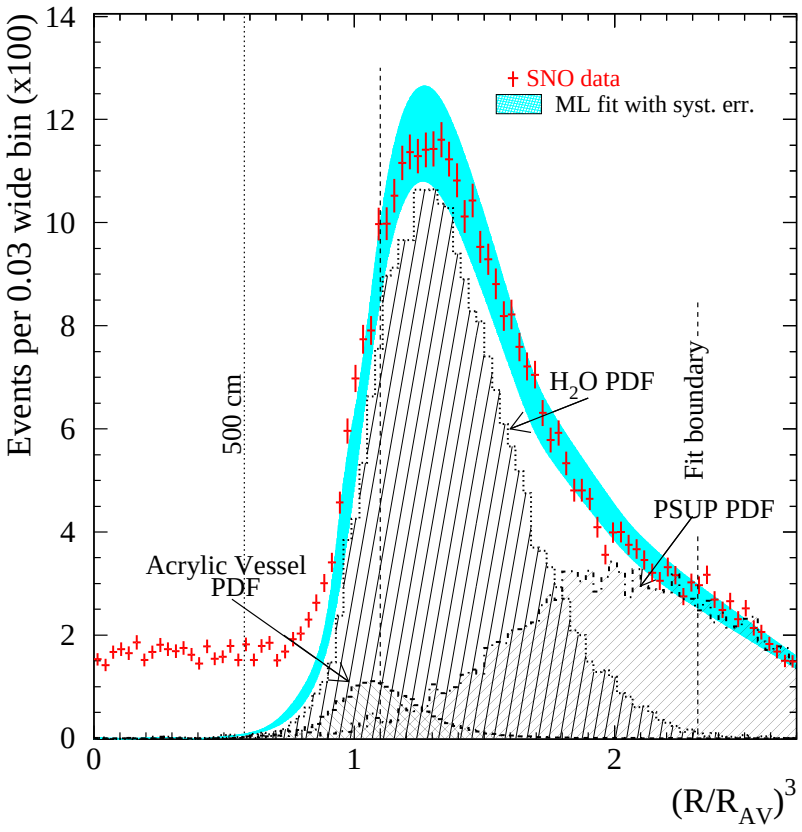

Fig. 5.19: 4.5 MeV fit on the neutrino data using the derived PDF for external Cherenkov backgrounds. The width of the bands represent the size of combined statistic and systematic uncertainties.

In order to determine the neutron contribution to the data from sources outside the D_2O we will fit inside a fiducial volume of 550 cm, adding to the 3 signals (ES, CC, NC) a separate PDF to represent the external neutron contribution. This PDF is taken from a ^{252}Cf source run very close to the AV. In order to ensure a Cherenkov background free region we will perform this extraction at a higher energy threshold (5.5 MeV kinetic energy). The details of how the signal extraction is done will be presented in Ch. 6. How well we can fit the radial shape is shown in Fig. 5.20.

The systematic uncertainties are calculated assuming $\pm 1\sigma$ on all variables of interest (energy scale, resolution, vertex resolution, etc.). Two additional uncertainties have to be considered:

- Where the neutrons are coming from. If we consider the AV as a source for the external neutrons, we can have the radioactivity plated inside or outside the AV. To determine how much an effect can that have, we can use ^{252}Cf runs right inside and right outside the AV. This accounts for 10% uncertainty on the neutron number.

- The ^{252}Cf source is a point source, whereas the radioactivity should be distributed on the surface of the AV. Using a different position for the source we estimate a 5% uncertainty due to differential detector response in different regions.

Finally, above an energy threshold of 5.5 MeV and inside 550 cm, we measure 51 ± 33 neutrons from external sources. In order to calculate this number for our nominal analysis threshold and fiducial volume, we scale based on the energy and radial profile of the events from the ^{252}Cf source deployed near the AV.

Knowing the strength of the ^{252}Cf source we can infer the neutron production

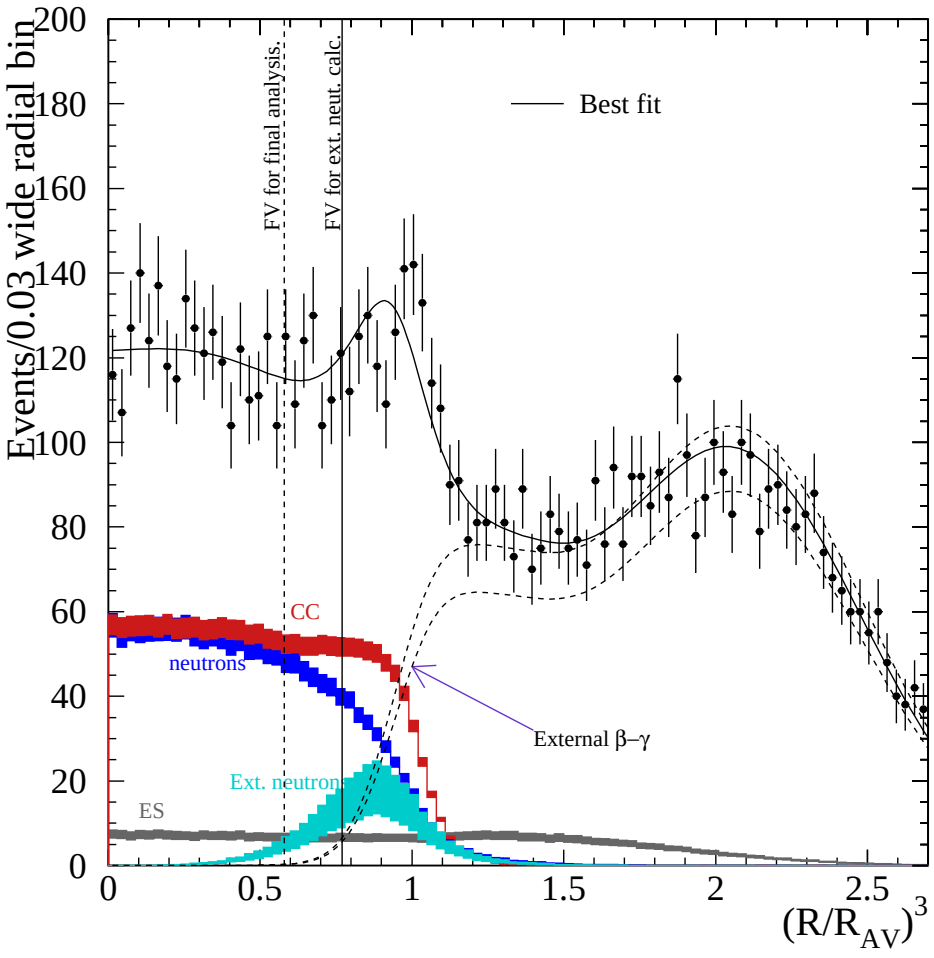

Fig. 5.20: The radial fit for external neutrons. The analysis threshold is 5.5 MeV chosen in order to reduce the Cherenkov background inside the fiducial volume. The dashed lines represent the low-side and the high-side uncertainties on external $\beta - \gamma$.

rate from the outer regions of the SNO detector. This was determined to be 3.4 ± 2.5 neutrons/day. The calculated expected neutron production rate is $2.4^{+0.8}_{-0.9}$ neutrons produced each day. Our activity measured from the data is consistent with this production rate.

5.4 Other backgrounds

Aside from what was presented above, there are several other sources of backgrounds, which although small relative to the photo-disintegration of deuterium by ^{238}U and ^{232}Th , still have to be taken into account and investigated. A list of this potential backgrounds to the neutron measurements is presented here.

- Cosmic ray interaction (spallations formed by muons and neutrinos). The number of events passing the "muon follower" cut in the DAMN mask has been determine to be < 1 event according to [47]

- Atmospheric neutrino charged-current and neutral-current interactions with a lepton below threshold. They lead to neutron production not associated with any visible tag[5]. This has been estimated in [58] to be 47 neutrons/kt/y.

- ^{24}Na activation by neutrons from muons, calibration, recirculation and the neck. The ^{24}Na has a half-life of 14.95 hours and decays to an excited state of ^{24}Mg. The de-excitation of ^{24}Mg produces a 2.7 MeV γ which can, in turn, photo-disintegrate the deuterium. It has been calculated in [58] that for the data set, the number of produced neutrons are as follow: 0.09 from muons, 2.2 ± 0.4 from calibrations, 3.0 ± 1.6 from recirculation and 2.0 ± 1.3 from the neck. The neck

[5]Unlike the neutrons produced by muon spallations

contribution is assumed to be included in our fit for external neutrons from Sec. 5.3.

- Reactor and terrestrial anti-neutrinos. In [58] the neutral-current and charged-current interactions of anti-neutrinos from reactors and from ^{238}U and ^{232}Th decays in the surrounding rock has been estimated to be 8 neutrons/kt/y. Scaled to our livetime and detection efficiency this will account for less than two neutrons in our signal region.

- Neutrons from the CNO solar neutrinos. The flux of mono-energetic neutrinos from electron capture decay of ^{15}O and ^{17}F has been estimated in [13] to be 4.77×10^5 and $0.08 \times 10^5\,\mathrm{cm}^{-2}\mathrm{s}^{-1}$respectively. From this we can infer the rate of produced neutrons in SNO to be 1 neutron/year. After scaling to livetime and capture efficiency this becomes a negligible background.

5.5 Summary

In this chapter we discussed the production of the main SNO backgrounds and how analysis techniques have been developed to reject them and to measure the contamination of the final neutrino data set. The summary of all the backgrounds investigated are presented in Table 5.6.

Background type	Estimated number of events
Instrumental	$< 3(95\%)$ CL
Internal Cherenkov (^{214}Bi)	14 ± 8
Internal Cherenkov (^{208}Tl)	3 ± 2
Internal Cherenkov (^{24}Na)	4 ± 2
External Cherenkov	$< 11(65\%)$ CL
Internal photodisintegration	72 ± 23
External neutrons	21 ± 10
Neutrons from atm. neutrinos	9 ± 2
Neutrons from ^{24}Na activation	5 ± 2
Neutrons from reactor and terrestrial $\overline{\nu}$	< 2

Table 5.6: Summary of SNO backgrounds

Ch. 6

Extracting SNO signals

As has been shown in the previous chapters, one can select from the SNO data a collection of neutrino event candidates, identify the largest backgrounds and measure them and quantify any sources of systematic uncertainties that can affect the neutrino measurement. In order to achieve the physics result, the final data set has to be classified as one of the three signals (ES, CC, NC) or as a background. Unfortunately, there is no way to do this classification as an event by event separation. Therefore, one has to rely on statistical techniques to determine the number of events in each category. As was shown in [59], the method of Maximum Likelihood will provide a good way of separating the SNO signals. This chapter will provide the statistical techniques needed and ways to implement the method for SNO.

6.1 A maximum likelihood extraction

Assuming a collection of data points, $\overline{x}_i$, which we can consider as an n-dimensional vector (x_i^j, with $j = 1, n$) and a set of parameters we need to estimate $\overline{\theta}$, an m-

dimensional vector (θ_i, $i = 1, m$) with $f(\overline{x}_i; \overline{\theta})$, the probability density function, (PDF) of measuring $\overline{x}_i$ given the parameter set $\overline{\theta}$. We can define the likelihood function as the joint probability of measuring the set $\overline{x}_i$ given $\overline{\theta}$ as:

$$\mathcal{L} = \prod_{i=1}^{n} f(\overline{x}_i; \overline{\theta}) \tag{6.1}$$

Maximizing $\mathcal{L}$ with respect to the set $\overline{\theta}$ will return the most probable values for $\overline{\theta}$ given the collection $\overline{x}_i$. As in [60], we can also consider random fluctuations on the total number of events n in the data set. Mathematically, this can be described by Poisson probability distribution in (Eq. (6.1)) with the mean value ν. (Eq. (6.1)) becomes then:

$$\mathcal{L} = \nu^n \frac{e^{-\nu}}{n!} \prod_{i=1}^{n} f(\overline{x}_i; \overline{\theta}) \tag{6.2}$$

This method is known as the Generalized Maximum Likelihood and is presented in detailed in [60] and [46].

For SNO, the problem simplifies somehow, since we want to estimate the total number of events of each type. In this case, the PDFs f in (Eq. (6.2)) become linear in the parameters $\overline{\theta}$:

$$f(\overline{x}_i; \overline{\theta}) = \sum_{j=1}^{m} \theta_j f(\overline{x}_i) \tag{6.3}$$

In the most general case, the vector $\overline{x}_i$ can be constructed out of the four variables that have different shapes for the three signals. These four are the energy, the radius, the isotropy parameter and the angle between the direction of the event and the direction of a vector pointing from the Sun: $\overline{x} = (R, T, \langle\theta_{ij}\rangle, \cos\theta_{\odot})$. They are shown

for each signal in Fig. 6.1. The vector of parameters to be estimated is composed of the number of events of each signal type: $\overline{\theta} = (N_{ES}, N_{NC}, N_{CC})$. (Eq. (6.3)) becomes then:

$$f(\overline{x}_i; \overline{\theta}) = N_{ES} f^{ES}(\overline{x}_i) + N_{CC} f^{CC}(\overline{x}_i) + N_{NC} f^{NC}(\overline{x}_i) \tag{6.4}$$

The PDFs used in the likelihood function can be obtained from MC or calibration, as histograms or from parameterizations of the detector response, as analytic functions. The calculation of the set of parameters that will maximize the likelihood function is done numerically, using the CERN's MINUIT package described in [61].

6.1.1 Constrained vs. unconstrained fit

The fit described in (Eq. (6.2)) and (Eq. (6.4)) is called the constrained fit, since we use in the fit the CC electron energy spectrum, which requires a specific ^{8}B neutrino energy spectrum. However, the neutrino oscillations are energy dependent, so the survival probability (see Sec. 1.2.3) can affect the energy spectrum in a differential way. In salt, the isotropy parameter carries a relatively large amount of information about each particular signal, so one can renounce the CC energy spectrum and try to do an extraction bin-by-bin in energy. This way, there is no constraint on the extracted fluxes so we have a model independent measurement. In principle, one should also consider the effect of a differential survival probability for the ES spectrum. The dependence of the ES electron energy on the neutrino energy is smaller than for CC interactions and the expected number of ES events is much smaller than the expected CC or NC. Consequently, we will neglect the effect of spectral distortion on the ES energy profile.

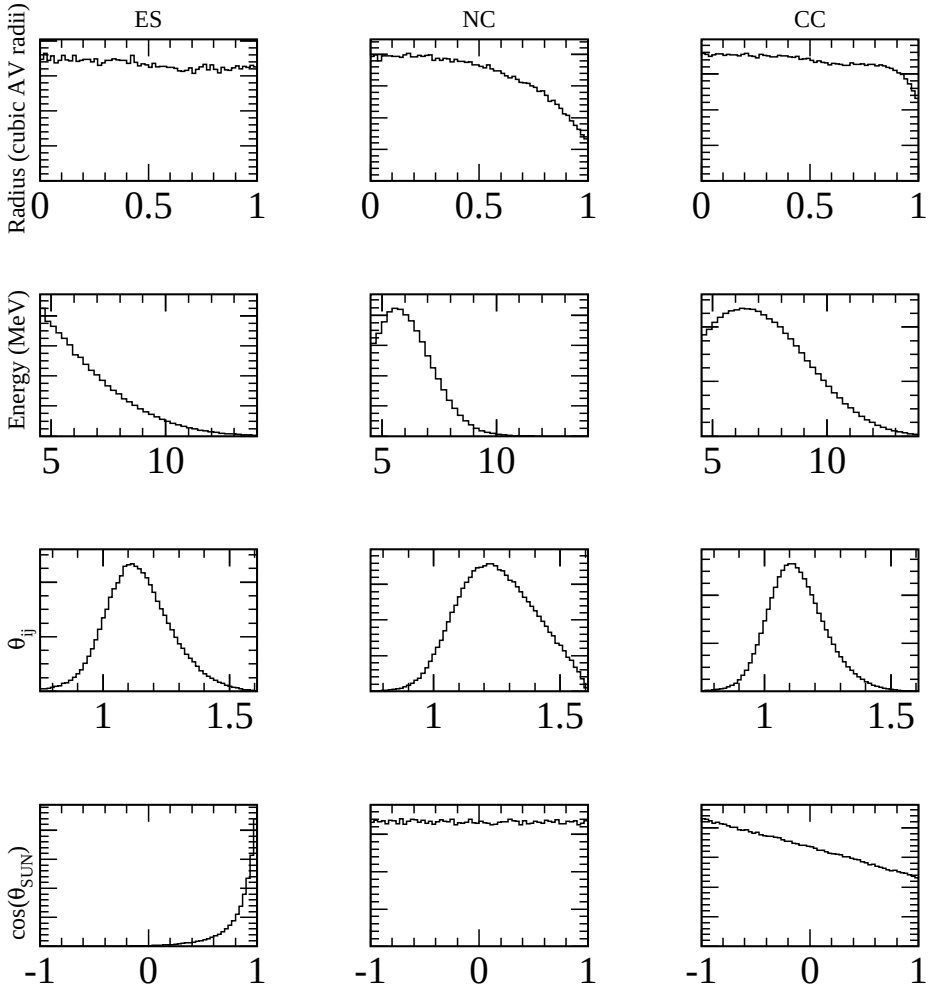

Fig. 6.1: The shape of the four variables we extract signals on.

Even if we do not consider the energy shape of the CC events, we can still impose the energy shape constraint on the NC, since the detected neutron energy has lost all the energy information present in the initial neutrino that interacts through the NC reaction and the neutron energy spectrum in SNO is well known through calibration. Finally, we can write (Eq. (6.4)) for the unconstrained case as:

$$f(\overline{x}_i;\overline{\theta}) = N_{ES} f^{ES}(\overline{x}_i) + \sum_{j=1}^{n_{cc}} N_{CC}^{j} f_j^{CC}(\overline{x}_i) + N_{NC} f^{NC}(\overline{x}_i) \tag{6.5}$$

where n_{CC} represents the number of energy bins in which the extraction is performed and N_j^{CC} is the number of CC events extracted in the j'th energy bin. For the CC PDF f^{CC}, we have now:

$$f_j^{CC}(\overline{x}_i) = h(\overline{y}_i)\eta_j(T_i) \tag{6.6}$$

Here, $\overline{y}_i$ contains all the usual variables in $\overline{x}_i$ except T_i, the energy of the i'th event in the data set and $\eta_j(T_i)$ is:

$$\eta_j(T_i) = \begin{cases} 1, & E_j \leq T_i < E_{j+1} \\ 0, & \text{otherwise} \end{cases} \tag{6.7}$$

where E_j and E_{j+1} represent the boundaries of the j'th energy bin.

6.1.2 Including the backgrounds

Apart from signal, one could have non-zero backgrounds present in the data set. The effect of backgrounds is two-fold: they get subtracted form the signal and the uncertainties in the background determination affects the final signal uncertainties. For a simple counting experiment this procedure works without any complication

and this is the exact case of the neutron backgrounds for our 500 cm fiducial volume. Since they have exactly the same characteristics as the NC events, there is no way to distinguish between them, therefore they get subtracted from the measured NC number only and the uncertainties are simply added in quadrature to the NC signal uncertainties.

For Cherenkov backgrounds though, the situation is not so simple. Since they hardly look like any single signal, they have to be added to the fit with the prior knowledge of their magnitudes, uncertainties and shapes. Having the shapes of these backgrounds on all variables of interest, one can add the backgrounds as additional entries in the vector $\overline{\theta}$ and fit them out of the data. Moreover, if we know the expected number of events of a particular backgrounds, we can also add a constraint on them as a Gaussian prior, centered on the expectation, with a width equal to the uncertainty in the background measurement. Finally, (Eq. (6.2)) becomes:

$$\mathcal{L} = \nu^n \frac{e^{-\nu}}{n!} \prod_{i=1}^{n} f(\overline{x}_i; \overline{\theta}_s, \overline{\theta}_b) \prod_{j=1}^{n_b} e^{-\frac{1}{2}\left(\frac{\theta_b^j - \hat{\theta}_b^j}{\sigma_j}\right)^2} \tag{6.8}$$

where $\overline{\theta}_b$ represents the background entries in the vector θ, $\hat{\theta}_b^j$, the measured values of j'th background being considered and σ_j, the uncertainty on that background measurement.

Using this method, the background subtraction will be done in a natural way and all the uncertainties on the backgrounds estimation will be propagated into the signal uncertainties, with all the correlations properly taken into account.

6.2 Statistical bias and uncertainties in signal extraction

The traditional SNO approach for extracting signals during the D_2O phase, when the variables used were only radius (R), energy (T) and $\cos\theta_\odot$, was to ignore the correlations between the extraction variables and write the global PDF $f(\overline{x};\overline{\theta})$ as:

$$f(\overline{x};\overline{\theta}) = \mathcal{R}(R)\cdot\mathcal{T}(T)\cdot\mathcal{C}(\cos\theta_\odot) \tag{6.9}$$

As long as the correlations between these variables are small, this simplification will not affect the result in any way. Nevertheless, in salt, there is a large correlation between the isotropy parameter and the energy of the event and this approximation breaks down. The obvious way out is the usage of multi-dimensional PDFs, where all the correlations are automatically included.

6.2.1 Sources of statistical bias

In order to study the statistical bias, the approach we take is to generate a large number of independent MC data sets (300) with known fractions of ES, NC and CC events and perform the extraction on each of them. The results obtained are expected to have a normal distribution around the known number of events from each type in the data set. Instead of using a fixed number of events of a certain type, we will allow for statistical fluctuations in the total number of events according to Poisson statistics. There are four source of statistical bias that were identified:

- Lack of data sets statistical independence

- Overlaps between the PDF and the data sets
- Ignored correlations
- Number of events in the PDF

The first two points are somewhat obvious and they are overcome in a straight forward way by generating enough statistical independent data sets and PDFs.

As mentioned in the previous section, ignoring the correlation between the $\langle\theta_{ij}\rangle$ and energy results in a significant statistical bias on the final result. Fig. 6.2 shows how the introduction of $\langle\theta_{ij}\rangle$ without properly accounting for correlations, changes the mean extracted CC number of events. The simple prescription to take into account the correlations in a natural way, is to make use of multi-dimensional PDFs. The statistical bias is eliminated for all practical purposes this way, as shown in Fig. 6.3.

6.2.2 A limited statistics PDF - the muon followers

In order to determine the statistical uncertainties, due to a PDF generated from a small number of events, we create 300 MC random data sets[1] and for each of them we will also randomly pick 300 NC PDFs with a fixed number of events in each PDF. The ES and CC PDFs have large statistics and they are kept the same for each MC experiment. On each MC data set we perform an unconstrained signal extraction with 10 CC energy bins from an energy threshold of T_{eff} >5.0 MeV. This whole procedure is repeated several times for different number of events in the NC PDFs. The results are summarized in Fig. 6.4, Fig. 6.5 and Fig. 6.6.

The uncertainties in the ES signal, as expected, do not depend on the number of events in the NC PDF, since it separates so cleanly through $\cos\theta_{\odot}$. The CC and NC

[1] 150 ES events, 1800 NC events and 1500 CC events, all subject to Poisson fluctuations

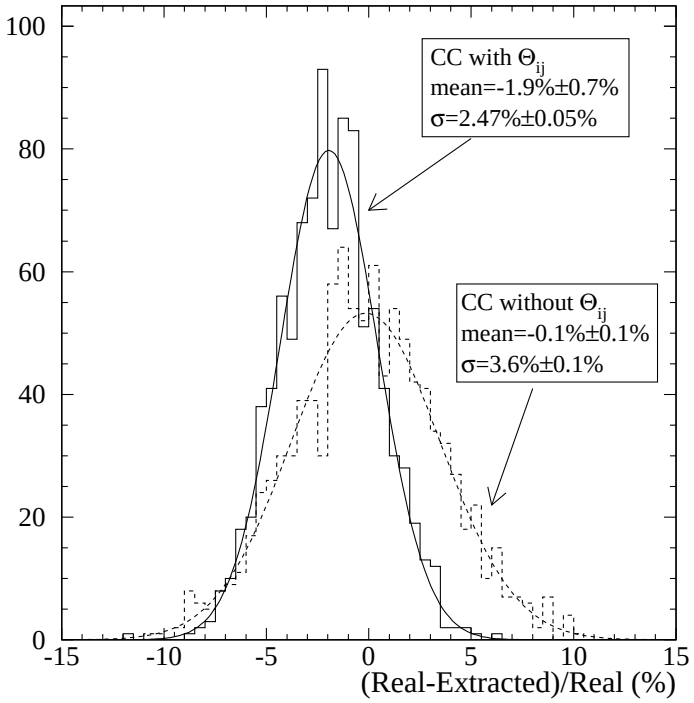

Fig. 6.2: Extraction on 300 MC data sets with and without $\langle\theta_{ij}\rangle$ ignoring the correlations

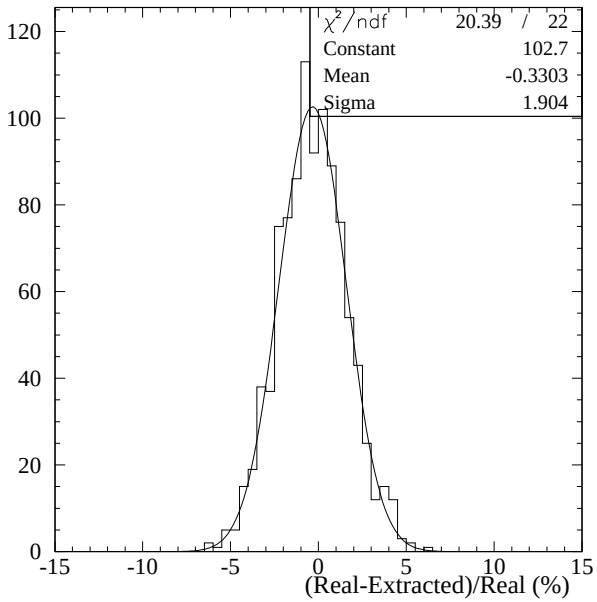

Fig. 6.3: Extraction on 300 MC data sets with $\langle\theta_{ij}\rangle$. The correlations between $\langle\theta_{ij}\rangle$ and energy are taken into account by simply building 2D PDFs.

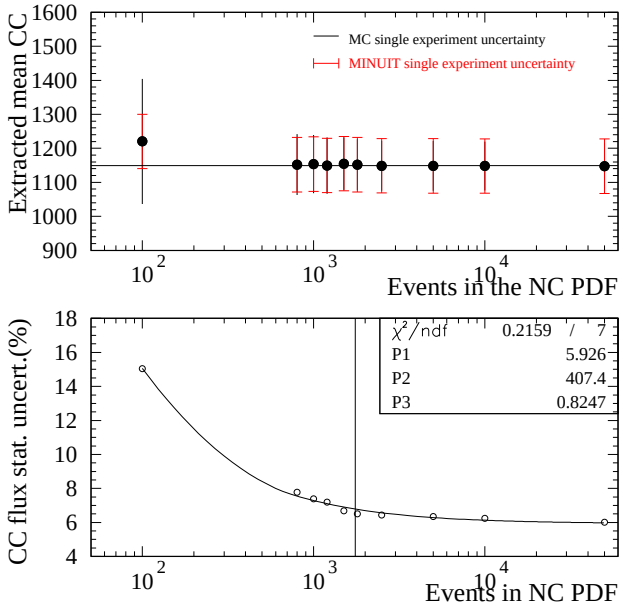

Fig. 6.4: Top: Mean CC extracted events for in the 300 trials. Bottom: Statistical uncertainty for an individual extraction as a function of number of events in the NC PDF

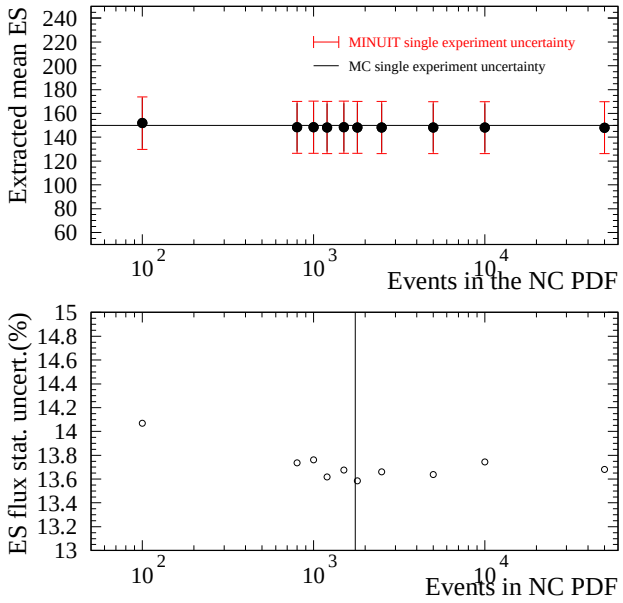

Fig. 6.5: Top: Mean ES extracted events for in the 300 trials. Bottom: Statistical uncertainty for an individual extraction as a function of number of events in the NC PDF

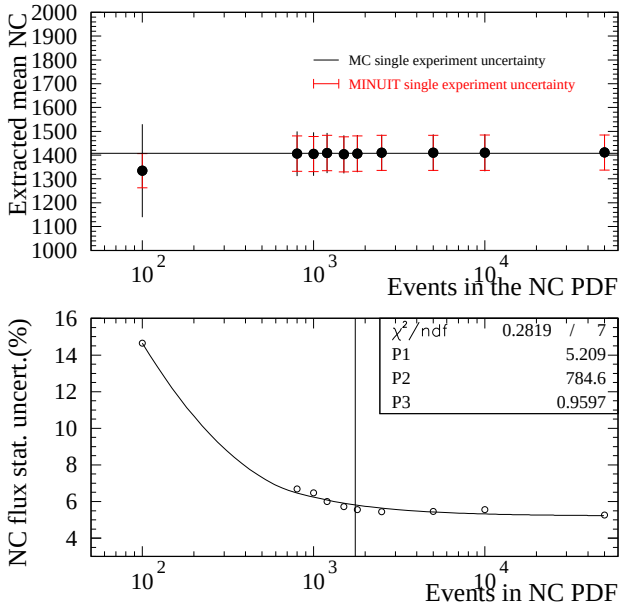

Fig. 6.6: Top: Mean NC extracted events for in the 300 trials. Bottom: Statistical uncertainty for an individual extraction as a function of number of events in the NC PDF

are covariant, so the uncertainty in the NC PDF reflects in the statistical uncertainty on both these two signals. The graphs from above show that for any practical purposes, the uncertainties obtained from the minimization algorithm (MINUIT[2].) are similar to the one obtained as the spread in the 300 extraction results.

The number of events in the muon follower PDF is ~ 1800 above a kinetic energy threshold of 5.0 MeV. The bottom graph in Fig. 6.6 can be fitted with the following function (see figure):

$$f(x) = 5.20 + \frac{786.7}{x^{0.96}} \tag{6.10}$$

which can be used to calculate the relative uncertainty (assuming our number of events) as a function of the number of events in the NC PDF. For the ~ 1800 events in the muon followers we obtain an uncertainty of 5.7% which is in good agreement with the uncertainty obtained from MINUIT. This uncertainty will depend on the actual number of events in the sample.

6.3 Fitting for flavor content

The three SNO signals are not independent variables. Assuming that the flux of neutrinos from the Sun is made only of active neutrinos, we can separate it as ϕ_{ν_e} (the flux of electron neutrinos) and $\phi_{\nu_{\mu\tau}}$ (flux of active non-electron neutrinos) and have:

$$\phi(^8B) = \phi_{\nu_e} + \phi_{\nu_{\mu\tau}} \tag{6.11}$$

[2]The MINUIT errors are derived from the covariance matrix, obtained by inverting the matrix of the second derivatives of the function to be minimized. More about MINUIT in [61]

The detected number of events for each SNO signal (N_{ES}, N_{CC} and N_{NC}) can then be related to ϕ_{ν_e} and $\phi_{\nu_{\mu\tau}}$ as:

$$N_{CC} = \sigma_{CC}\phi_{\nu_e} \tag{6.12}$$

$$N_{NC} = \sigma_{NC}(\phi_{\nu_e} + \phi_{\nu_{\mu\tau}}) \tag{6.13}$$

$$N_{ES} = \sigma_{ES}^{\nu_e}\phi_{\nu_e} + \sigma_{ES}^{\nu_{\mu\tau}}\phi_{\nu_{\mu\tau}} \tag{6.14}$$

where σ_{CC} and σ_{NC} are the average charged-current and neutral-current neutrino cross-sections on deuteron and σ_{ES} is the elastic scattering cross-section for neutrinos on electrons, which is different for ν_e and ν_μ or ν_τ. The above cross-sections are integrated over the number of targets and multiplied by the livetime of the experiment. The reason for this difference is the fact that ν_e can interact with an electron through a Z or W-exchange, whereas ν_μ and ν_τ can interact only through a Z-exchange. For the energies we are interested on we have that $\frac{\sigma_{ES}^{\nu_{\mu\tau}}}{\sigma_{ES}^{\nu_e}} \approx 0.154$, therefore, we can rewrite the last equation in (Eq. (6.14)) as:

$$N_{ES} = \sigma_{ES}^{\nu_e}(\phi_{\nu_e} + 0.154\phi_{\nu_{\mu\tau}}) \tag{6.15}$$

Having made this substitution, we can then fit for the two independent variables ϕ_{ν_e} and $\phi_{\nu_{\mu\tau}}$ in (Eq. (6.8)) as opposed to the three variables we used so far (N_{ES}, N_{NC} and N_{CC}).

Ch. 7

Results

Previous chapters showed how the data is processed and selected and how we reject and measure the most important backgrounds. Using the Generalized Maximum Likelihood technique described in Ch. 6 we can perform a fit on the data using the PDFs described in Ch. 4 to extract the signals of interest. In what follows we will present the analysis of 254.158 days of solar neutrino data from the salt phase of SNO. In the end we will make a measurement of the electron solar neutrino flux and non-electron solar neutrino flux.

7.1 Corrections to the MC predicted neutrino flux

To obtain the neutrino flux from the extracted number of events of each type we need to use the MC prediction for events inside the signal region as the normalization. After the MC is generated, a number of correction at a percent level have to be applied to account for small effects not taking into account in MC. Below is a list of all the corrections we apply.

1. Livetime: The MC is generated according to the measured livetime of each run. However, the "burst" cuts from the DAMN mask will introduce a small "dead-time" which has to be corrected for. The total "dead-time" and the correction has been measured in [62]

2. Number of targets in the fiducial volume: The simulation is done with fewer electrons and deuterons than there are in the detector. We use the actual number of electrons and deuterons from [63] as an overall correction.

3. DAMN and HLC acceptance: Using the acceptances discussed in Sec. 4.5 we will correct the simulation to account for loss of events due to the above cuts.

4. g_A correction: The neutrino cross-sections on deuterons used in the SNO MC are derived in [64] based on an effective field theory. More recent calculations in [65] pointed out that the weak axial coupling to nucleons is not the latest in literature and a correction should be made.

5. $L_{1,A}$: In the effective field calculations, the two-body axial exchange current counter-term, $L_{1,A}$, is the only unknown parameter to the Next-to-Next-to-Leading order. We make a correction on the cross-sections to account for the most up to data value recommended in literature ([66], [65]).

6. Radiative corrections: The MC simulation does not take into account the radiative components to the neutrino cross-sections. These are applied as corrections through proper weighting of the PDFs using the formulae shown in [63]. In the following, T is the kinetic energy of the electron and $f(T)$ is the correction factor derived.

- ES

$$w_{ES} = 0.9764 - 7.8110^{-4}T - 1.3110^{-4}T^2 + 3.6410^{-6}T^3 \qquad (7.1)$$

- CC

$$w_{CC} = 1.0318 - 7.4510^{-4}T + 4.7210^{-6}T^2 \qquad (7.2)$$

- NC

$$w_{NC} = 1.0154 \qquad (7.3)$$

7. Capture efficiency: We will re-scale the capture efficiency in MC based on Sec. 4.4.5

8. MC propagation error: Very seldom, the MC will fail to properly propagate all the Cherenkov photons created. This will result in an error, such that, the total number of events that fall in the signal region is lower than what it should be.

9. NC MC acceptance: We have to re-scale the MC acceptance for NC events as derived in Sec. 4.4.4.

10. SSM: For simulation purposes, SNO uses for the total neutrino flux calculation in [13] (BP2000), which predicts a solar flux of $5.15 \times 10^6 \mathrm{cm}^{-2}\mathrm{s}^{-1}$. This calculation has been revisited and the new prediction for the total flux changed slightly to $5.05 \times 10^6 \mathrm{cm}^{-2}\mathrm{s}^{-1}$.

11. CC interaction on ^{16}O and NaCl: Since ^{16}O and NaCl are abundant in the detector, there is a non-zero probability for a neutrino CC interaction on these nuclei. The correction to be applied for these processes has been derived in [58].

Correction	ES	CC	NC
Livetime	0.9821	0.9821	0.9821
Number of electrons	1.0151	-	-
Number of deuterons	-	1.0122	1.0122
DAMN+HLC acceptance	0.9914	0.9943	0.9932
g_A	-	1.0111	1.0111
$L_{1,A}$	-	0.984	0.979
CC on O,NaCl	-	1.0081	-
Radiative	see text	see text	1.0154
Capture Efficiency	-	-	1.032
MC round-off	1.0045	1.0054	1.0052
MC acceptance for NC	-	-	0.993
SSM	0.9806	0.9806	0.9806
Total	**0.974**	**0.977**	**1.002**

Table 7.1: Corrections to flux predictions from MC

7.2 Constrained fit results

After applying all the cuts described before we select for the final data set 2729 events above an energy threshold of 5 MeV and inside 500 cm. First we will fit the neutrino data using the constraint imposed by the ^{8}B energy spectrum. As described in Sec. 6.1.2, the backgrounds are included with Gaussian priors in the fit. Therefore the uncertainties in the background determination will come out as statistical uncertainties and will be included in the uncertainties shown in Table 7.3. There are four backgrounds categories we include: neutrons (which includes photo-disintegration, external and any other neutrons), and three Cherenkov backgrounds, ^{214}Bi , ^{208}Tl and ^{24}Na . The central values and the uncertainties on these are shown in Table 5.6. The number of events of each signal/background we fit for is shown in Table 7.2

The quality of the fit in all three variables, energy, $\cos\theta_\odot$ and $\langle\theta_{ij}\rangle$ is shown in Fig. 7.1, Fig. 7.2 and Fig. 7.3.

	ES	CC	NC	neutrons	^{214}Bi	^{208}Tl	^{24}Na
Number of events	151	1166	1297	107	11	2.8	3.8
Stat. uncertainty	22	58	65	25	8.6	2	1.7

Table 7.2: Extracted number of events of each type with statistical uncertainties as obtained from the constrained fit

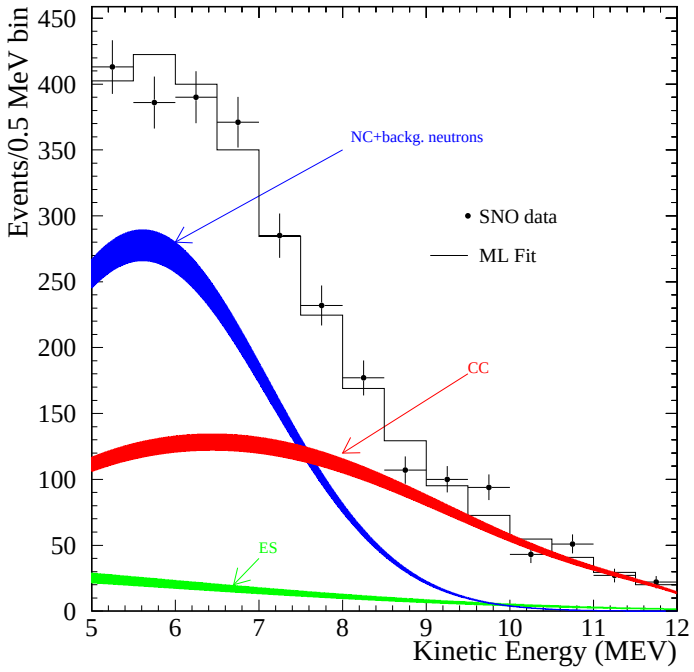

Fig. 7.1: Fit to the data in energy. The width of the bands represent the statistical uncertainty

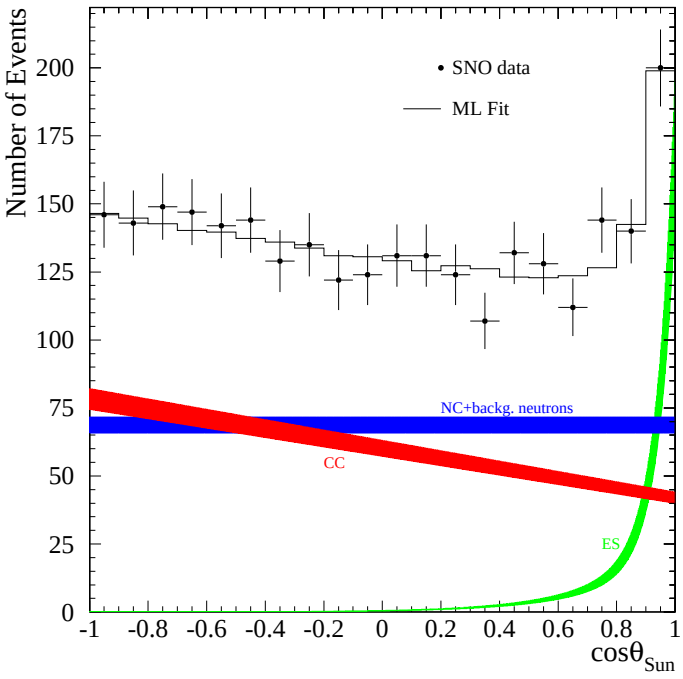

Fig. 7.2: Fit to the data in $\cos\theta_{\odot}$. The width of the bands represents the statistical uncertainty

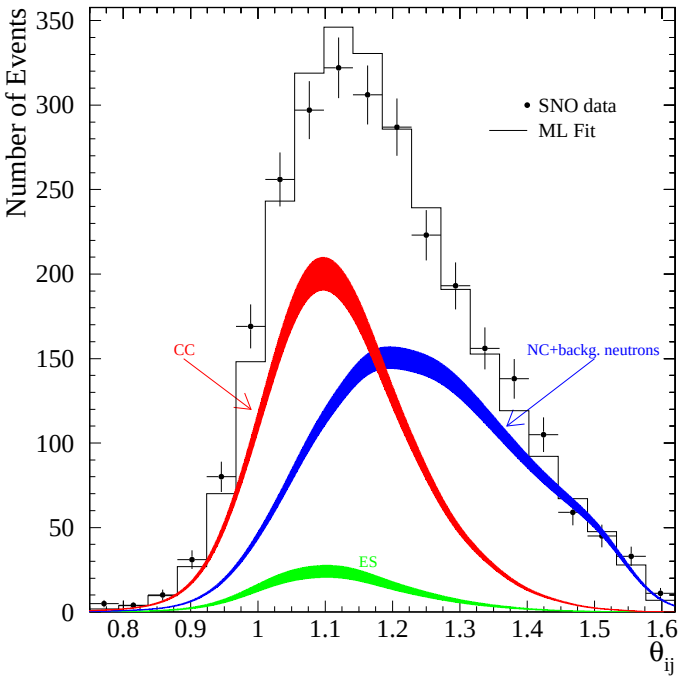

Fig. 7.3: Fit to the data in $\langle \theta_{ij} \rangle$. The width of the bands represents the statistical uncertainty

	ES	CC	NC	neutrons	^{214}Bi	^{208}Tl	^{24}Na
Number of events	151.3	1179.7	1270.8	107.0	13.7	2.8	3.8
Stat. uncertainty	22	63	74	25	8	2	2

Table 7.3: Extracted number of events of each type with statistical uncertainties as obtained from the unconstrained fit. The reader is reminded that the statistical uncertainties include the uncertainty in the backgrounds determination

	ES	CC	NC	neutrons	^{214}Bi	^{208}Tl	^{24}Na
Number of events	150.6	1178.0	1273.3	107.0	13.5	2.8	3.8

Table 7.4: Extracted number of events of each type as obtained from the unconstrained fit using the MC NC PDF

7.3 Unconstrained fit results

As presented in Sec. 6.1.1, we can extract the signals without any constraint on the CC energy spectrum. The actual extraction uses 1 MeV wide energy bins from threshold to 14 MeV and an overflow bin from 14 MeV to 20 MeV. The number of events extracted for ES, NC and CC signals is shown in Table 7.3.

Based on the extracted numbers from Table 7.2, we see a difference of ~ 20 events for the NC, between constrained and unconstrained fits. This is well within the quoted statistical uncertainties. Also, there is a change of 4 events in the total number of signals extracted, due to a statistical variation in the extracted number of ^{214}Bi Cherenkov backgrounds.

We can use MC for the NC PDF rather than the muon followers. For an unconstrained fit, the extracted number of events are shown in Table 7.4. The differences are again well within the quoted statistical uncertainties.

7.3.1 Systematic uncertainties

Systematic effects impact the final measured fluxes in two ways. One, as a change in the PDF shapes and therefore a change in the extracted number of events and two, as a change in the overall acceptance, which will change the total MC prediction. The effects considered and their related uncertainties were presented in Ch. 4. To estimate the effects on fluxes we will change each parameter by one standard deviation and recalculate the fluxes. Finally, all the derived uncertainties are added in quadrature assuming no correlation among the systematic effects. The list of systematic effects considered and how we propagate them to the final fluxes is listed below. The quantitative impact these uncertainties have on the fluxes are shown in Table 7.5.

- Energy scale and resolution: In Sec. 4.1 we showed how the energy response of the SNO detector can be characterized in terms of scale and resolution. We change the energy of every MC CC and ES event by $\pm 1.1\%$ to account for the uncertainty in the energy scale. This will change both the extracted number of events (the shapes change) and the MC prediction. For NC, we proceed in the same way by using the uncertainty derived in Sec. 4.4 for the extracted number of events. To the prediction derived from MC we assign a $\pm 2.5\%$ uncertainty as it was derived in Sec. 4.4.4. The uncertainty on the energy resolution is presented in Sec. 4.1.1. Each MC event is multiplied by a Gaussian deviate with width $\sigma(E)((1+0.035)^2 - 1)$, where 3.5% is the uncertainty from Sec. 4.1 and $\sigma(E)$ is the resolution dependence on energy from (Eq. (4.1)).

- Reconstructed position and reconstruction resolution: The radius of each MC event is changed by $\pm 1\%$ to account for the uncertainty on the MC reconstructed position (see Sec. 4.2.1). As in the case of energy, the x, y and z coordinates of

an event are deviated with a Gaussian with width $17((1+0.15)^2-1)$, where 17 cm is the reconstruction resolution as derived from ^{16}N studies and 15% is the uncertainty quoted in Sec. 4.2.1.

- Angular resolution: This will have a relatively large impact on the ES $\cos\theta_\odot$ distribution, which is strongly peaked towards 1. The CC $\cos\theta_\odot$ distribution has a -1/3 slope, so the effect will be less important while the NC is unaffected by this angular resolution. To simulate the effect of the uncertainties presented in Sec. 4.2.2 we will increase/decrease the width of the ES peak and the CC slope accordingly. Since we fit throughout the physical range of the $\cos\theta_\odot$ distribution, the angular resolution will impact the fluxes only through the change in the fitted number of events.

- $\langle\theta_{ij}\rangle$ ratio: We change the $\langle\theta_{ij}\rangle$ ratio by $\pm 1.9\%$ to account for the uncertainty in Sec. 4.3.1. This uncertainty was applied for CC and ES signals only. The NC uncertainty is much smaller, due to the particular PDF we use. It is taken to be 0.4% and not correlated with the one on ES and CC signals. To derive the systematic on the final flux, we perturb the CC and ES distributions and then, separately, the NC one. The final uncertainties are added in quadrature. It is obvious the the final uncertainties are dominated by the $\pm 1.9\%$ on the CC and ES signals, and the NC uncertainty is almost negligible for the final result. The $\langle\theta_{ij}\rangle$ ratio will also have an effect on the extracted number of events only.

- Cherenkov background shapes: As discussed in Sec. 5.2.2, the only uncertainty in the shapes of the Cherenkov backgrounds comes from $\langle\theta_{ij}\rangle$ ratio. We will change this ratio accordingly and re-fit the data. For external Cherenkov backgrounds we also assign 7 events uncertainty on each signal.

Systematic	ES	CC	NC
Energy scale	$^{+2.2(-0.1)}_{-1.5(+0.5)}$	$^{+1.0(-0.2)}_{-1.0(+0.1)}$	2.5(0.1)
Energy resolution	+0.3(+0.2)	+0.3(−0.0)	
Vertex shift	$^{+2.8(-0.1)}_{-2.7(+0.1)}$	$^{+2.8(-0.1)}_{-2.7(+0.1)}$	$^{+2.8(0.1)}_{-2.8(-0.1)}$
Vertex resolution	−0.1(+0.0)	+0.1(+0.1)	+0.0(−0.1)
Angular resolution	$^{+2.6(+2.6)}_{-1.5(-1.5)}$	$^{+0.1(+0.1)}_{-0.1(-0.1)}$	$^{+0.2(-0.2)}_{-0.0(-0.0)}$
θ_{ij}	±1.3(±1.3)	±2.8(±2.8)	±2.8(±2.8)
Cer. backg. shape	$^{+0.2(+0.2)}_{-0.2(-0.2)}$	$^{+0.6(+0.6)}_{-0.6(-0.6)}$	$^{+0.5(0.5)}_{-0.4(-0.4)}$
Ext. Cherenkov backgrounds	±0.0	±0.5	±0.5
Cut efficiency	$^{+0.16}_{-0.11}$	$^{+0.16}_{-0.11}$	$^{+0.16}_{-0.11}$
Capture eff.	±0.0	±0.0	±2.9
Cross-section	±0.0	±1.8	±1.3
Total	$^{+4.6}_{-3.7}$	$^{+4.5}_{-4.4}$	$^{+5.7}_{-5.6}$

Table 7.5: Systematic uncertainties (%) on the neutrino fluxes. In parenthesis, we show the effect of a particular systematic on the extracted number of events. The reader is reminded that the uncertainties on the *number* of background events will come out as "statistical uncertainty" due to the fitting technique used

- Neutron capture efficiency: This will influence the NC flux only and the 2.9% uncertainty in Sec. 4.4.5 will be added to the total NC uncertainty.

- Neutrino cross section on deuteron: We assign a 1.3% uncertainty on the NC and 1.8% uncertainty on the CC for the theoretical calculations. This includes uncertainty on the g_A, difference between [64] and [66], radiative corrections uncertainties and theoretical cross-section uncertainty from [67].

Table 7.5 summarizes the systematic uncertainties derived on the measured neutrino fluxes for an unconstrained analysis. We show in parenthesis the effect a particular systematic has on the extracted number of events.

ES	CC	NC
362.4	3653.0	1296.3

Table 7.6: The expected MC production rates for our livetime

7.3.2 ES, CC and NC neutrino fluxes

Inside our signal region we expect, based on MC, the number of events shown in Table 7.6. Based on these rates and after the corrections have been applied we can obtain the solar neutrino flux as measure via each of the three reaction in SNO. The results obtained in a model independent way without imposing any constrain on the energy spectrum of the neutrinos are ($\times 10^6 \mathrm{cm}^{-2}\mathrm{s}^{-1}$):

$$\phi_{ES} = 2.16 \pm 0.31(\mathrm{stat.})^{+0.10}_{-0.08}\ (\mathrm{syst.})$$

$$\phi_{CC} = 1.67 \pm 0.10(\mathrm{stat.})^{+0.07}_{-0.07}\ (\mathrm{syst.})$$

$$\phi_{NC} = 4.94 \pm 0.31(\mathrm{stat.})^{+0.28}_{-0.28}\ (\mathrm{syst.})$$

We remind the reader that the fluxes published by SNO in [19] for the pure D_2O phase for a constrained analysis are shown below. There is an agreement at less than 1 statistical standard deviation.

$$\phi_{ES} = 2.39^{+0.24}_{-0.23}(\mathrm{stat.})^{+0.12}_{-0.12}\ (\mathrm{syst.})$$

$$\phi_{CC} = 1.76^{+0.06}_{-0.05}(\mathrm{stat.})^{+0.09}_{-0.09}\ (\mathrm{syst.})$$

$$\phi_{NC} = 5.09^{+0.44}_{-0.43}(\mathrm{stat.})^{+0.46}_{-0.43}\ (\mathrm{syst.})$$

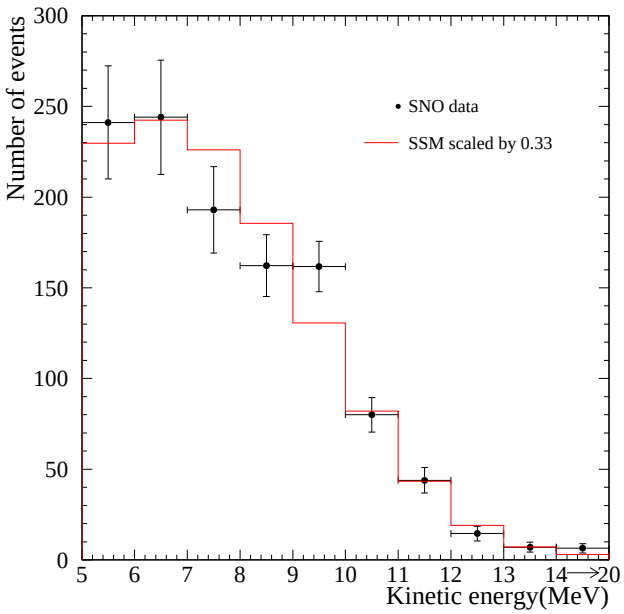

Fig. 7.4: The extracted number of events in each CC energy bin together with the MC prediction. The overall MC normalization has been scaled by 0.33. The extraction is done in 1 MeV wide bin from 5 to 15 MeV and the last bin contains the overflow to 20 MeV

7.3.3 The extracted CC spectrum

Using the unconstrained fit we can extract the number of events in each CC energy bin. This is shown in Fig. 7.4. The error bars on the plots are statistical only. We also show the ratio of number of events in each bin to SSM in Fig. 7.5. This ratio is consistent with flat throughout the energy range.

7.3.4 Fit for the "flavor content"

As mentioned in Sec. 6.3, we can fit the neutrino data with only two signal parameters (ϕ_{ν_e} and $\phi_{\nu_{\mu\tau}}$) and the usual backgrounds. This should in principle allow for smaller statistical uncertainties, since the number of parameters are reduced, therefore the

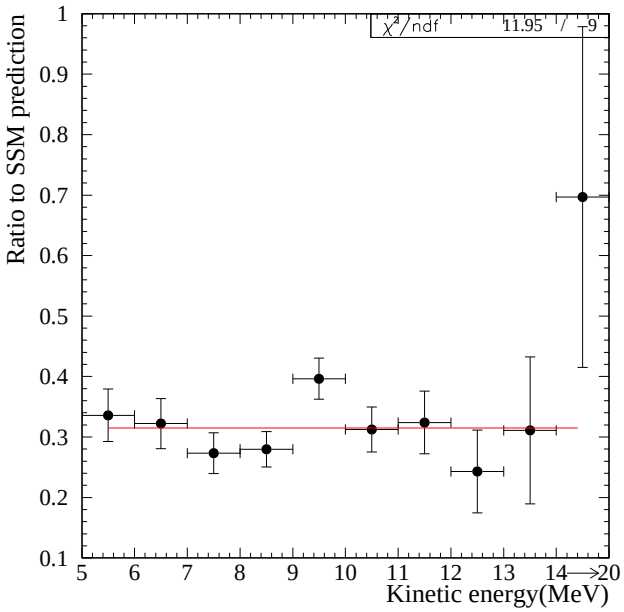

Fig. 7.5: Ratio of number of extracted events in each bins to the SSM prediction

number of individual correlations decreases. Nevertheless, since the ES extracted number of events, which is the extra constrain SNO has besides CC and NC, lacks the statistical precision one would want, there is not a significant improvement in the result. The extracted fluxes of electron and non-electron neutrinos are shown below ($\times 10^6 \mathrm{cm}^{-2}\mathrm{s}^{-1}$).

$$\phi_{\nu_e} = 1.66 \pm 0.10(\mathrm{stat.})^{+0.07}_{-0.07}\ (\mathrm{syst.})$$

$$\phi_{\nu_{\mu\tau}} = 3.32 \pm 0.38(\mathrm{stat.})^{+0.26}_{-0.25}\ (\mathrm{syst.})$$

Combining the statistical and systematic uncertainties in quadrature we obtain for the non-electron solar neutrino flux $3.32^{+0.46}_{-0.45}$. Fig. 7.6 shows the flavor content of the solar neutrino flux as measured during the first 254 days in the D_2O +NaCl

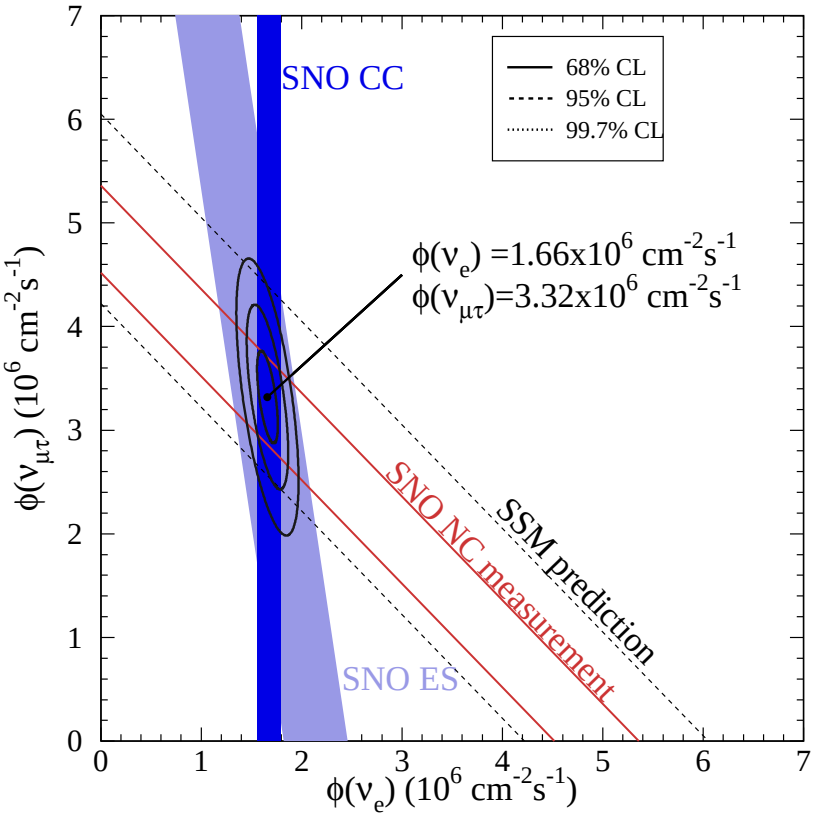

Fig. 7.6: The flavor content of the solar neutrino flux as measured in the D_2O +NaCl phase of SNO

phase of SNO.

Through another change of variables, we can fit for the "survival probability" P_{ee} and the total ^{8}B flux. This is very similar to the fit for the flavor content. The survival probability was found to be $P_{ee} = 0.33 \pm 0.04(\text{stat.})^{+0.02}_{-0.02}$ (syst.) or $P_{ee} = 0.33 \pm 0.05$, where the statistical and systematic uncertainties have been added in quadrature. This is more than 3σ away from the 0.5 value predicted by an MSW model for the maximum mixing in the solar neutrino sector.

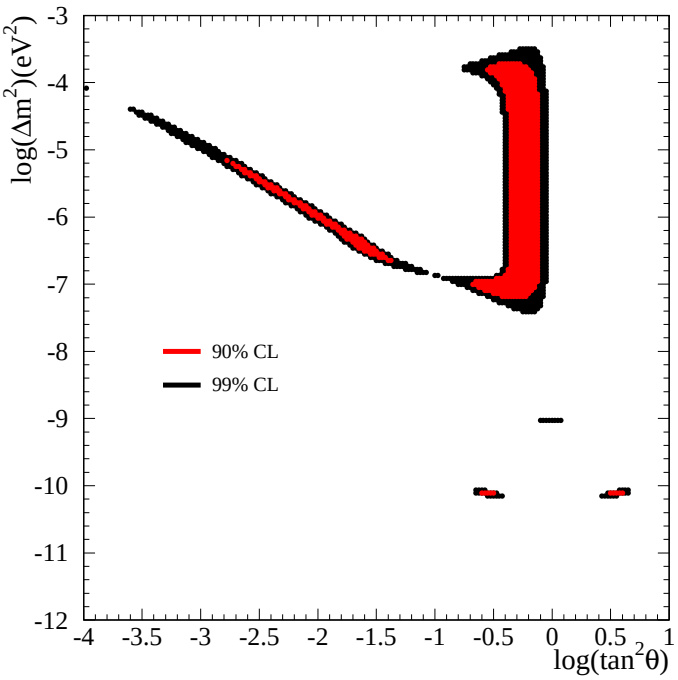

Fig. 7.7: The allowed MSW parameters as derived from the NaCl phase of SNO

7.4 Limits on the MSW parameters

Based on the analysis presented before we can restrict the allowed range for the MSW oscillation parameters (Δm^2 and $\tan^2\theta$). We will scan the MSW plane and minimize the likelihood function for the total ^{8}B flux, the backgrounds and include the most significant systematic uncertainties. We ignore in this analysis the effects of the neutrino propagation through the Earth. The 90% and 95% CL regions allowed by the data analyzed in this thesis is shown in Fig. 7.7.

Ch. 8

Conclusions and the Future

The SNO experiment provided the first measurement of the total solar neutrino flux through the NC reaction on deuterons. This has equal sensitivities to all neutrino flavors and when combined with the CC reaction, which is sensitive to the electron neutrino only, gives us extremely important information about the survival probabilities of neutrinos as they travel from the solar core to Earth.

During the first phase, using only D_2O as the target D_2O , SNO has provided direct evidence for solar neutrino transformation. When the SNO result was combined with other solar neutrino experiments, the LMA region of the MSW plane was strongly favored. This first measurement was obtained assuming a standard ^8B shape and no distortion of the CC energy spectrum through flavor transformations. The total neutrino flux, measured through the NC interaction, was determined with 12.5% uncertainty, when the statistics and systematics where combined.

The constraint on the CC energy spectrum can be relaxed, allowing for an analysis which does not depend on the exact knowledge of the ^8B spectrum and its modifications through flavor changes. For the D_2O phase the total solar neutrino flux from

the NC interaction was measured with a 26% uncertainty.

In June 2001 NaCl was added to the D_2O region of the SNO detector. The salt concentration by weight in heavy water is $0.196 \pm 0.002\%$. This allowed for an increased neutron capture efficiency, higher neutron energy and the possibility of better separating the CC and NC events through the isotropy information. In this theses, we presented the analysis of the first 254 days of SNO data taken during this second phase of the experiment. Since the energy distribution is not as critical as before, we can relax the CC constraint on energy and perform an analysis independent of the shape of the ^{8}B spectrum. The uncertainty on the total solar neutrino flux as measured through the NC interaction was 9% with a central value in agreement with the previous SNO measurements and with the theoretical calculations. This data provided direct evidence for non-electron flavor solar neutrinos. The measured fluxes of electron and non-electron solar neutrinos were found to be ($\times 10^6 \mathrm{cm}^{-2}\mathrm{s}^{-1}$):

$$\phi_{\nu_e} = 1.66 \pm 0.10(\mathrm{stat.})^{+0.07}_{-0.07}\ (\mathrm{syst.})$$
$$\phi_{\nu_{\mu\tau}} = 3.32 \pm 0.38(\mathrm{stat.})^{+0.26}_{-0.25}\ (\mathrm{syst.})$$

The global solar neutrino analysis now provides very stringent bounds on the MSW parameters (Δm^2 and $\tan^2\theta$). A global analysis including all the previous solar and reactor experiments and the SNO data presented here will place tight bounds on the θ_{12} angle relevant for the solar neutrino oscillations . These bounds can be in principle improved by the ^{7}Be experiments (BOREXINO) or future experiments that would measure the *pp* neutrinos. For any significant improvement, these experiments should perform a measurement at less than 1% uncertainty according to [68]. This requires

a significant amount of effort in order to achieve such a low uncertainty.

The atmospheric neutrino data together with the K2K experiment indicate maximal mixing with $0.75 < \tan^2\theta_{23} < 1.3$ at 1σ level [69]. The analysis of data from CHOOZ experiment indicate small mixing for the third mixing angle, with $\sin^2\theta_{13} < 0.02$ ([69]). The solar neutrino analysis together with data from the KamLAND experiment point to a large mixing angle but not maximal.

Assuming the framework of three neutrino species, the three mixing parameters are complemented with 3 CP violation parameters as described in Sec. 1.2; the Dirac CP violating phase and 2 Majorana CP violating phases. The first could be within the experimental reach of the near future if the θ_{13} angle will prove sufficiently large. Future long-baseline neutrino experiments may be able to measure or set strict bounds on the θ_{13} angle and eventually measure the CP violation phase. The Majorana phases, although not affecting the oscillation pattern, are still important parameters that need to be measured. Double-beta decay experiments will attempt to at least probe whether neutrinos are Dirac or Majorana particles.

The field of neutrino physics had a lot of surprises and turns throughout the past 30 years. Our understanding of these particles has greatly improved and new discoveries are within reach in the next decade.

Appendix A

The H_2O PDF from Encapsulated ^{232}Th and ^{238}U Sources

For the NaCl+D_2O analysis we had the opportunity to use a ^{222}Rn spike to build a PDF for the H_2O radioactivity. During the D_2O phase there was no such deployment so we used a series of encapsulated ^{232}Th and ^{238}U source runs to create a volume weighted PDF for the H_2O . The same construction was also used for the D_2O +NaCl data as a cross-check on the spike PDF.

To obtain an H_2O PDF, we take encapsulated source runs at different radii to form a distribution approximating a uniform distribution of radioactivity in the light water, and weight by volume and lifetime accordingly. One option for the volume weighting is to take equal volumes around the source position to obtain a "representative shell" for run i[1] using Eq. (A.1). The inner radius of the innermost shell in the light water is taken to be the AV radius, while the outermost radius of the outermost shell is

[1]Taking equal lengths around the source position instead of equal volumes does not change the PDF shape

taken to be R= 840 cm (the PSUP radius).

$$\Delta V_i = \left(\frac{R_{i+1} - R_i}{2}\right)^3 - \left(\frac{R_i - R_{i-1}}{2}\right)^3 \tag{A.1}$$

This volume weighting does not ensure a "smooth" distribution for the H_2O PDF. This is particularly a problem when the distance between two source positions is larger than the expected reconstruction resolution. In order to obtain a more uniform distribution we use for the salt phase a different algorithm which ensures uniformity. The basic assumption is that the reconstruction characteristics do not change drastically from one position to a neighboring one, therefore one can use the radial distribution at position x and slide it back and forth through the entire "representative region" of the position x. The H_2O region is separated in 50 shells of equal radii. The representative region for position x is defined by those radial shells which are closest to x. For example, assuming a 5 cm division, and an hypothetical first source position at 620 cm with a second source position at 630 cm, the first 5 shells from 600 cm to 625 cm will be represented by the data at 620 cm accordingly shifted in radius to account for the actual position of the current shell. We use 14 source positions deployed throughout the H_2O volume.

The normalization for the shell x is done by linearly interpolating the detector response at the source positions bracketing the shell x. The detector response is obtained using the total number of events per second above the analysis threshold. This is shown in Fig. A.1. Each distribution is then weighted by the volume it represents and divided by the source run time. An example of these 50 obtained distributions is shown in Fig. A.2. The envelope of these 50 histograms is the H_2O PDF.

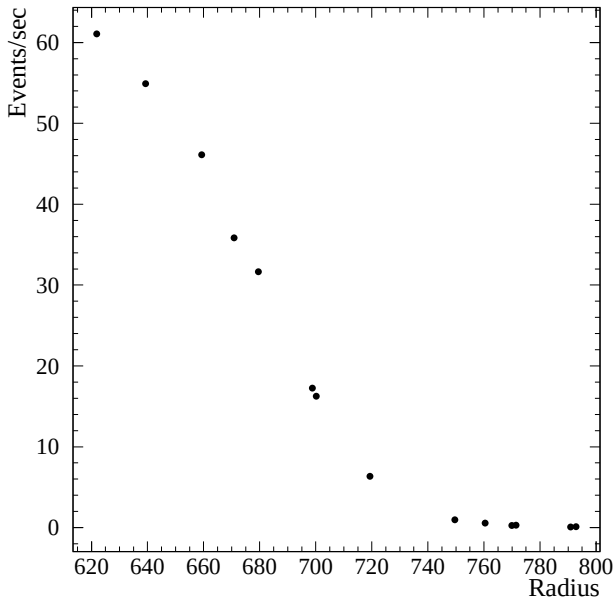

Fig. A.1: Number of events per second above the analysis threshold for encapsulated sources in H_2O . This is used to model the detector response.

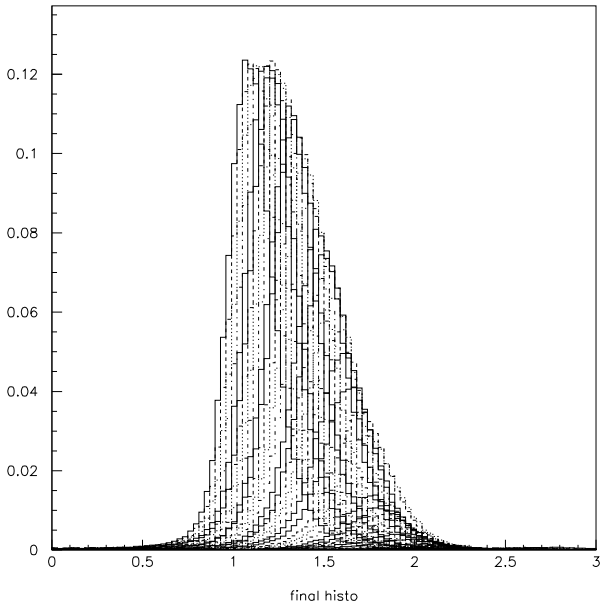

Fig. A.2: PDFs from 50 radial shells in H_2O .

Bibliography

[1] C. Cowan, F. Reines, F. Harrison, H. Kruse, and A. McGuire, Science **124** (1956).

[2] B. T. Cleveland, T. Daily, J. Raymond Davis, J. R. Distel, K. Lande, C. Lee, P. S. Wildenhain, and J. Ullman, Astrophysical Journal **496**, 505 (1998).

[3] M. Gell-Mann and Y. Ne'man, *The Eightfold Way* (Perseus Publishing, 2000).

[4] S. L. Glashow, Nucl. Phys. **22**, 579 (1961).

[5] S. Weinberg, Phys. Rev. Let. **19**, 1264 (1967).

[6] A. Salam, in *Elementary Particle Theory, Relativistic Groups and Analyticity* (1969), pp. 367–377.

[7] S. L. Glashow, J. Iliopoulos, and L. Maiani, Phys. Rev. D **2**, 1285 (1970).

[8] P. Langacker, *Neutrino oscillation workshop 2000: Conference summary* (2000).

[9] M. Apollonio *et al.* (CHOOZ), Phys. Lett. **B466**, 415:430 (1999).

[10] L. Wolfenstein, Phys. Rev. D **17**, 2369 (1978).

[11] S. P. Mikheev and A. Y. Smirnov, Soviet Journal Nuclear Physics **42**(6), 913 (1985).

[12] E. K. Akhmedov, *Neutrino physics*, hep-ph/0001264 (2000).

[13] J. N. Bahcall, M. Pinsonneault, and S. Basu, Astrophys. J. **555**, 990 (2001).

[14] J. Bahcall, *Neutrino Astrophysics* (Cambridge University Press, Cambridge, 1989).

[15] J. Bahcall, available at `http://www.sns.ias.edu/~jnb/`.

[16] H. H. Chen, Phys. Rev. Let. **55**(14), 1534 (1985).

[17] Q. R. Ahmad *et al.* (SNO), Phys. Rev. Let. **87**(7) (2001).

[18] S. Fukuda *et al.* (SuperKamiokande), Phys. Rev. Let. **86**, 5651 (2001).

[19] Q. R. Ahmad *et al.* (SNO), Phys. Rev. Let. **89**(1) (2002).

[20] J. N. Bahcall, P. I. Krastev, and A. Y. Smirnov, JHEP **05**, 015 (2001).

[21] Q. R. Ahmad *et al.* (SNO), Phys. Rev. Let. **89**(1) (2002).

[22] K. Eguchi *et al.* (Kamland), Phys. Rev. Let. **90**, 021802 (2003).

[23] P. C. de Holanda and A. Y. Smirnov, JCAP **0302**, 001 (2003).

[24] G. Ewan *et al.*, *Sudbury Neutrino Observatory Proposal*, SNO technical report SNO-STR-87-12, Queen's University (1987).

[25] J. Boger *et al.*, Nuclear Instruments and Methods **A449**, 172 (2000).

[26] T. Ekenberg, F. M. Newcomer, R. Van Berg, A. Biman, and R. L. Stevenson, in *IEEE Transactions on Nuclear Science* (1995), vol. V0042, pp. 925–932.

[27] F. M. Newcomer and R. Van Berg, in *IEEE Transactions on Nuclear Science* (1994), vol. V0042, pp. 745–749.

[28] R. Stevenson *et al.*, in *Conference Issue of the 1994 Transactions on Nuclear Science* (1994).

[29] J. R. Klein, M. S. Neubauer, R. Van Berg, and F. M. Newcomer, *The SNO trigger system*, SNO technical report SNO-STR-97-036, University of Pennsylvania (1997).

[30] S. Biller *et al.*, *SNO Electronic Calibration Constants*, Tech. Rep., SNO Collaboration (2001).

[31] M. S. Neubauer, *Evidence for Electron Neutrino Flavor Change through Measurement of the* ^{8}B *Solar Neutrino Flux at the Sudbury Neutrino Observatory*, Ph.D. thesis, University of Pennsylvania, Penn (2001).

[32] J. R. Klein, *Design of the SNO timing system*, SNO technical report SNO-STR-95-007, University of Pennsylvania (1995).

[33] The SNO Collaboration, *The SNOMAN User's Manual*, version 4.01 ed.

[34] D. Cowen, G. Jonkmans, R. Komar, C. Okada, and R. Tafirout, *The SNO Database: SNODB v3.06.05*, Penn, Neuchatel, UBC, LBNL, Laurentian (1998).

[35] CERN Program Library Long Writeup Q180, *HEPDB Database Management Reference Manual.*

[36] W. R. Nelson, H. Hirayama, and D. W. Rogers, *The EGS4 code system*, Stanford Linear Accelerator Center (1985).

[37] Radiation Shielding Information Center, Los Alamos National Laboratory, *MCNP4A, A Monte Carlo N-Particle Transport Code System* (1993).

[38] CERN Program Library Long Writeup Q121, *Physics Analysis Workstation - User's guide.*

[39] *ROOT - An Object-Oriented Data Analysis Framework*, see http://root.cern.ch/.

[40] J. Cameron *et al.*, *The Gain and the Pain: A Study of Detector Response and Instrumental Backgrounds After the High Voltage Raise*, SNO technical report SNO-STR-99-039, University of Pennsylvania, Oxford University, TRIUMF, and Queens Universty (1999).

[41] M. G. Boulay, *Direct Evidence for Weak Flavor Mixing with the Sudbury Neutrino Observatory*, Ph.D. thesis, Queen's University (2001).

[42] K. Graham, *Energy Systematics for the Salt Phase*, Tech. Rep., Queen's University (2003).

[43] K. Graham, *Salt Data Reconstruction Analysis*, SNO Internal Report, SNO (2003).

[44] K. Miknaitis and A. Hallin, ^{16}N *Z-scan studies in salt and vertex shift systematics*, SNO Internal Report, SNO (2003).

[45] C. J. Jillings, *The Angular Resolution of SNO*, SNO technical report SNO-STR-98-010, Queen's University (1998).

[46] W. Eadie, *Statistical Methods in Experimental Physics* (North Holland, Amsterdam, 1971).

[47] A. D. Marino, *Muon Induced Spallation Products in the Salt Phase*, SNO Internal Report, LBL (2003).

[48] Y. Koshio, *Study of Solar Neutrinos at Super Kamiokande*, Ph.D. thesis, University of Tokyo, Tokyo (1998).

[49] Y.-F. Wang, V. Balic, G. Gratta, A. Fasso, S. Roesler, and A. Ferrari, Phys. Rev. D **64**(1), 013012 (2001).

[50] M. Kos, K. Graham, and A. Hime, *Neutron Detection Efficiency during the Salt Phase of SNO*, SNO Internal Report, SNO (2003).

[51] N. McCauley *et al.* (Salt Data Cleaning Working Group), *Updates to Data Cleaning for the Salt Phase*, SNO Internal Report, SNO (2003).

[52] P. C. Bergbusch, *Measurement of the Decay* $K^+ \to \pi^+ \nu\overline{\nu}$, Ph.D. thesis, University of British Columbia, Vancouver (2000).

[53] X. Chen, *Monte Carlo Simulations and Analyses of Backgrounds in the Sudbury Neutrino Observatory*, Ph.D. thesis, Balliol College, Oxford University, Oxford (1997).

[54] J. Farine *et al.* (Low Energy Background Working Group), *Low Energy Backgrounds during the Salt Phase of SNO*, SNO Internal Report, SNO (2003).

[55] J. Klein, *A Short, Sharp Shock: Results from the* D_2O *Rn Spike*, Tech. Rep., University of Texas - Austin (2003).

[56] S. Bryce *et al.*, *First generation of encapsulated U/Th sources*, Tech. Rep., Los Alamos National Laboratory (1998).

[57] V. Rusu, *Proposal for a Rn spike in* H_2O , Tech. Rep., University of Pennsylvania (2003).

[58] H. Robertson *et al.*, *"Other" Backgrounds Sources in the Salt Phase of SNO*, SNO Internal Report, SNO (2003).

[59] E. Beier and W. Frati, *Extraction of CC, NC, and ES Signals II - Acrylic Radioactivity Three Parameter Maximum Likelihood Analysis*, Tech. Rep. SNO-STR-91-19, University of Pennsylvania (1991).

[60] G. Cowan, *Statistical Data Analysis* (Oxford University Press, 1998).

[61] CERN Program Library Long Writeup D506, *MINUIT, Function minimization and error analysis.*

[62] K. Miknaitis *et al.*, *Livetime for the salt data set*, SNO Internal Report, SNO (2003).

[63] P. J. Doe *et al.*, *Systematics of the* D_2O *target in SNO*, SNO Technical Report SNO-STR-2002-005, SNO (2002).

[64] M. Butler, J.-W. Chen, and X. Kong, Phys. Rev. **C63**, 035501 (2001).

[65] J. F. Beacom and S. J. Parke, Phys. Rev. **D64**, 091302 (2001).

[66] S. Nakamura, T. Sato, V. Gudkov, and K. Kubodera, Phys. Rev. **C63**, 034617 (2001).

[67] S. Nakamura *et al.*, Nucl. Phys. **A707**, 561 (2002).

[68] J. N. Bahcall and C. Pena-Garay (2003), `hep-ph/0305159`.

[69] M. C. Gonzalez-Garcia and C. Pena-Garay (2003), hep-ph/0306001.